The Dissertation Committee for Xiaolong Wang

certifies that this is the approved version of the following dissertation:

Highly Integrated Polymer Photonic Switching and Interconnects

Committee:

Ray T. Chen, Supervisor

Jack C. Lee

Michael F. Becker

Ananth Dodabalapur

Shaochen Chen

Highly Integrated Polymer Photonic Switching and Interconnects

by

Xiaolong Wang, B.S., M.S.E.

Dissertation

Presented to the Faculty of the Graduate School of

the University of Texas at Austin

in Partial Fulfillment

of the Requirements

for the Degree of

Doctor of Philosophy

The University of Texas at Austin

December 2006

Dedicated to my wife

Acknowledgements

I would like to thank the faculty and staff of the Microelectronics Research Center and the Department of Electrical and Computer Engineering at The University of Texas at Austin for providing me with such an intellectually stimulating environment to conduct my research and pursue my graduate education. I greatly appreciate my advisor, Dr. Ray T. Chen, for his support and guidance in my research work. Many thanks also go to my committee members, Dr. Jack C. Lee, Dr. Michael F. Becker, Dr. Ananth Dodabalapur, and Dr. Shaochen Chen, for their insightful advices on my dissertation.

I would like to acknowledge the productive collaborations with Dr. Brie Howley, a former student in the Optical Interconnect Group and now a research staff at MIT Lincoln Lab. I also want to thank Dr. Maggie Y. Chen, Dr. Wei Jiang, and other group members for their help over the years.

Finally, I would like to express my gratitude to my wife, Jinhong for her love and support during my Ph.D. program. I also thank my father, who passed away last year, my mother, and my parents in-law for their support and encouragement.

Highly Integrated Polymer Photonic Switching and Interconnects

Publication No. _____

Xiaolong Wang, Ph.D.
The University of Texas at Austin, 2006

Supervisor: Ray T. Chen

Benefited from its tremendous gain in bandwidth, optics is taking the leader role instead of electronics in many communication systems for the past three decades, and is expected to continue this trend irresistibly in the predictable future. From the architecture point of view, most optical communication systems provide only the point-to-point topology. The interconnection among the distributed nodes still has to rely on the electronic exchanger, which is becoming an imminent bottleneck throttling the overall system bandwidth. In contrast, all optical exchange networks employing optical switches will skip the heavy-loaded data conversion and achieve a prominent bandwidth enhancement and cost reduction. In the first part of this dissertation, a planar lightwave circuit (PLC) based polymer optical switch utilizing total internal reflection (TIR) effect was proposed and fabricated. The optimized device obtained many desired features, such as low insertion loss, low cross talk, low power consumption and wavelength insensitivity. The application of the TIR optical switch was extended to provide true time delays (TTD) for phased array antennas (PAA). A fully integrated 4-bit TTD device

composed of TIR switches and waveguide delay lines successfully delivered the 16 delay values required by a PAA system.

As we move from long-distance network to short distance reach, optics encounters increasing difficulties in terms of packaging, reliability and system cost. However, with the rapid increasing speed and complexity of VLSI technology, electrical interconnects will fail to provide sufficient bandwidth beyond 10GHz after 2012. There does exist an opportunity for the continuing exploration of optics to complement or even replace the conventional board level electrical interconnects. An innovative approach with a fully embedded structure is anticipated to overcome the technical and cost barriers that prohibit the realization of optical interconnects in board levels. In the second half of this dissertation, technology efforts projected to relieve the concerns of low cost, high performance optical layers, as well as the system integration issues were carried out. The research accomplishments include a 51cm long molded waveguide array with 150GHz optical bandwidth, 85% coupling efficiency surface normal micro-mirror and system integration with laser diodes and photo detectors.

Table of Contents

Chapter 1 Introduction

1.1 Photonic Switch for Backbone Optical Networks

In the beginning to the 21st century, there has been an intense race in optical fiber communication systems. The transmission capacity using dense wavelength division multiplexing (DWDM) was boosted up to terra bits per second. The world's record was set by NEC in March 2001 with an incredible bit rate of 10.9Tb/s (273 channels for 40Gb/s each) over 117km distance[1]. However, this rapid trend slowed down in the past five years due to the information technology (IT) industry recession and the facing technical difficulties, such as information handling capacity. The deployed optical communication system is not constrained by the signal transmitting capacity, but by the exchange rate between the network nodes. It is analog to a high way with only a narrow entrance or exit, causing a traffic jam with a long queue.

Electronics switching is high efficient in routing due to the mature and sophisticated logic circuit and data storage technology that has been studied extensively. However, electronics switching is highly dependent on data rate and protocol, which will result in the addition or replacement of electronics switching when upgrade systems. Additionally, optical signal has to be converted to electronic signal (O/E conversion) before electrically switching, and then after, converted back to optical (E/O conversion) form again. With the network capacity increasing, electronics switching nodes seem unable to keep up with the bit rate, causing electronics bottle neck.

Optical add drop module (OADM) [2] using optical switches, wavelength multiplexer (MUX) shown in Fig 1.1 is designed to solve this stringent limitation. The optical switches can selectively download the signal from the channel, upload the signal to the channel, or simply pass the signal through the OADM, depending on the working status of the optical switches, either in the cross or the bar state. Unlike any electrical exchange processors, optical switching enables routing of optical data signals without O/E and E/O conversion, and therefore, is independent of data rate and data protocol,

namely it is transparent for data transmission. This will greatly improve the system capacity and decrease the overall system cost, because of the reduction of network equipment.

Optical switches have been investigated for over thirty years since the dawning of the optical communication. Generally speaking, there are four categories, mechanically moved fiber switches, micro electro-mechanical system (MEMS) switches [3], planar lightwave circuit (PLC) switches [4] and others, including ink-jet [5] switches, and so forth. In the following subtopic, we will focus on the PLC based optical switches and their applications.

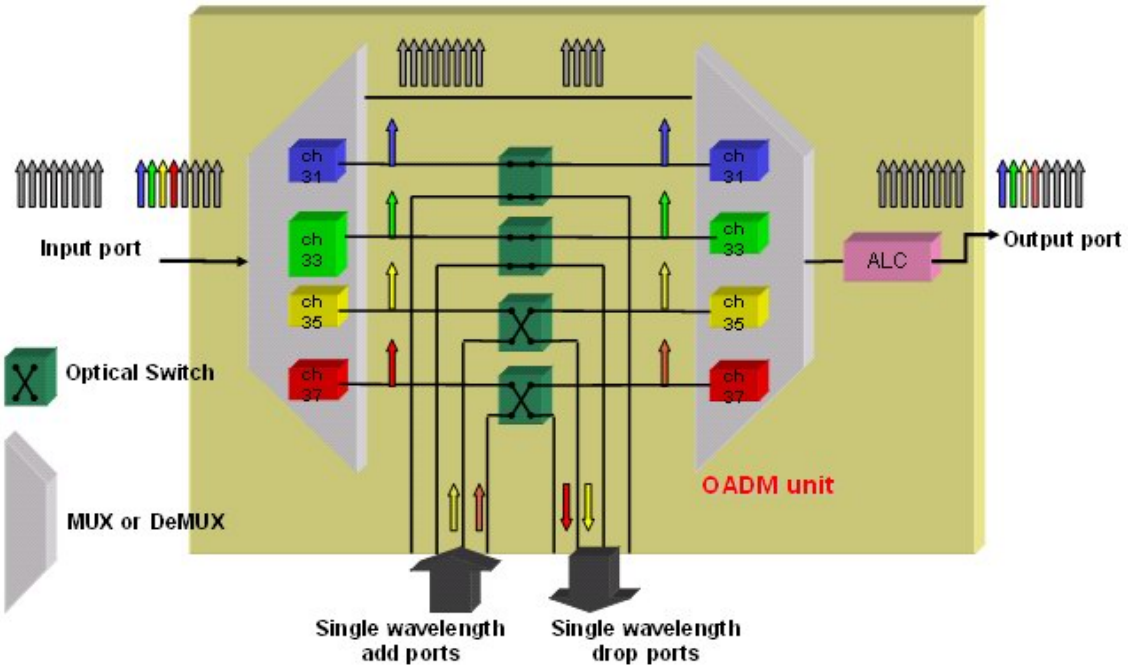

Fig 1.1 OADM unit using optical switches and wavelength multiplexers

1.2 PLC based Optical Switches

PLC technology offers a great benefit for optoelectronics in the aspect of integrating various optical devices, for example, optical switches, modulators, arrayed waveguide gratings (AWG) and variable optical attenuators (VOA) on a single chip,

which can be fabricated at a low cost. The PLC based optical switches, which are also named as waveguide optical switches, basically work on the principle of interference, mode evolution and total internal reflection (TIR). We will give a short introduction to the three types of PLC optical switches.

A well know Mach-Zehnder Interferometer (MZI) optical switch [6] using 3-dB couplers typifies the first category. The output beam can swing between the two output waveguides depending on the phase shift in the modulation arms. Another interesting structure is called directional coupler, which is depicted in Fig.1.2 (a). Here, two phase matched optical waveguides are arranged at such a small separation that light, by evanescent coupling, is periodically coupled back and forth between the waveguides in the direction of light propagation. When the refractive index is changed, the original phase matching between the waveguides is destroyed, and full switching of light between the output ports can be achieved. This kind of directional coupler requires precise coupling length to obtain complete power transfer. It will stay in cross state only if $\Delta\beta=0$ and L/l=2n+1, where L is the coupling length, $\Delta\beta=\beta_1-\beta_2$, β is the propagation constant of the two waveguides, and $l=\pi/2\kappa$ is called the conversion length, κ is the coupling coefficient between the two waveguides. The switch will be in the bar state if

$$(\frac{L}{l})^2 + (\frac{\Delta\beta L}{\pi})^2 = (2n)^2 \qquad (1.1)$$

The conditions for the bar and cross states can be depicted in a switching diagram as Fig 2(b). These cross states are represented by only discrete points as labeled. For example, we can switch the directional coupler by changing the refractive indices from a cross state at $L/l=1$ to a bar state, shown as the horizontal dashed line in Fig 1.2(b). The phase shift for a DC switch is $\sqrt{3}$ times that of a MZI structure [7].

Fig.1.2 (a) Structure of directional coupler optical switch

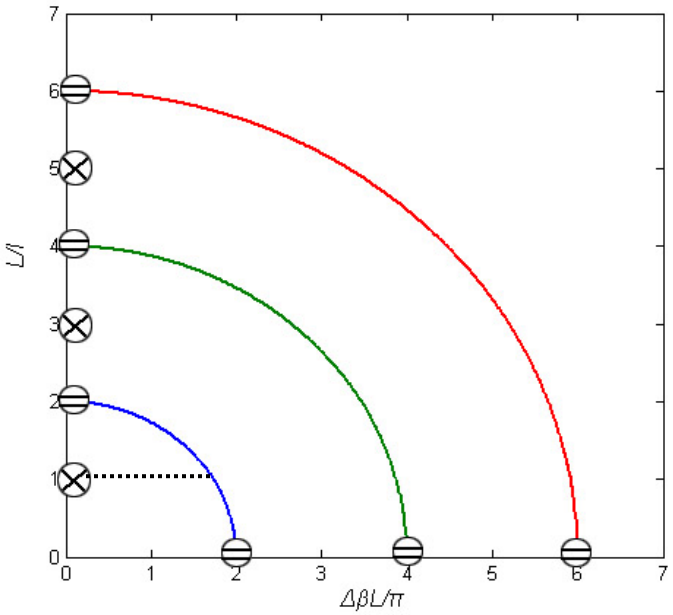

Fig.1.2 (b) Switching diagram of the directional coupler

Interference optical switch has limited performance in the optical bandwidth and periodic or quasi-periodic output versus the control voltage. An alternative to such interference switches is the digital optical switch (DOS) [8], based on mode evolution [9]. The operation principle of the DOS can be explained with reference to Fig 1.3: In an asymmetric structure, the field lunched from the wider input port will only excite even mode (base mode) in the cross area, because the effective index of the input port is more closely to the effective index of the even mode other than the odd mode (first order mode). If the branch angle θ is small enough, namely, satisfying $\theta << \Delta\beta / \gamma$, where $\Delta\beta$ is the average difference between the propagation constant of the two normal modes in the cross section, and γ is the transverse propagation constant, the Y branch will act as a mode separator rather than a power splitter, resulting in guiding all power into the wider output port because the effective indices of the two areas are more close to each other. But if we apply a voltage and decrease the refractive index of the wider output port even lower than the narrow port, all power will be switched to the narrow one. Similarly, if we launch the light from the narrower input port, it will only excite odd mode in the cross

area. Since the refractive index of the narrower out port is more close to the odd mode, all power will come out from narrower port. But if we decrease the refractive index of this port, the light will be switched to the wider port. Unlike the interference optical switch, the output of the DOS is not sensitive to the index modulation as long as it is large enough for the switching.

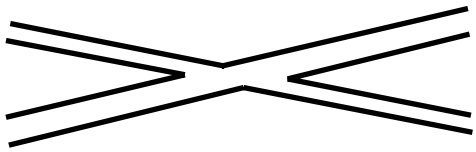

Fig 1.3 Structure of the digital optical switch

The TIR switch will be investigated thoroughly in Chapter 2. Compared with the other two switches aforementioned, TIR switches have a significant advantage in their broad optical bandwidth, or equivalently, their wavelength insensitivity. The pros and cons of the three optical switch structures are compared in Table 1.1.

Table 1.1 Comparison of different optical switch structures

Structure	length	Required index change	Wavelength coverage	Power consumption	Cross talk
Interference	Long (>10mm)	Small ($<10^{-4}$)	Small (<20nm)	Low(<20mW for polymer)	High (-20dB)
DOS	Long (>20mm)	Large (10^{-3}~10^{-4})	Large (<100nm)	Very high (>200mW for polymer)	Low (-40dB)
TIR	Short (<5mm)	Large (10^{-2}~10^{-3})	Very Large (>500nm)	Medium (30~100mW for polymer)	Low (-40dB)

Three possible ways can be adopted to effectively change the waveguide refractive index: thermo-optic effect, electro-optic effect and acousto-optic effect. Their performances are listed in Table 1.2.

Table 1.2 Comparison of different modulation mechanism

Modulation mechanism	efficiency	Power consumption	Optical Loss	Polarization dependence	Speed
Thermo-optic	High (10^{-4}/K for polymer)	High	Small	No	Low (>μs)
Electro-optic (Pockel effect)	Low (γ_{33}~30pm/V)	Very low	Large	Yes	Very fast (<ns)
Electro-optic (Plasma dispersion effect)	Medium	Low	Large	Yes	Fast (~10-100ns)
Acousto-optic	Medium	Medium	Medium	Yes	Low(ms)

To choose a proper material to build up the optical switch is another issue needs to be addressed. Polymer, as a remarkable platform for integrated optics, has drawn intensive investigation in the past decade [10]. The stability and transparancy of the polymer materials is improved greatly with the efforts of chemistry and materials science researchers. The material absorption loss is decreased to 0.05dB/cm [11] or even lower, which is comparable with silica waveguide. The isotropic property of polymers enable the photonic devices to be polarization independent. With a large thermo-optic coefficient, polymers provide an easy and effective mechanism to manipulate photons using little power. A thermo-optic photonic device with several milliwatts power consumption has

been reported [12]. Table 1.3 compares the material characteristics of polymers, $LiNbO_3$, silica, Silicon-on-insulator (SOI) and III-V semiconductor compounds.

Table 1.3 Comparison of different materials

Materials	Modulation efficiency	Optical loss	Speed	Polarization dependence	Integration
TO polymer	$>10^{-4}$/K	<0.1dB/cm	~1ms	No	Yes
EO polymer	Up to 300pm/V	1dB/cm	<1ns	Yes	Yes
$LiNbO_3$	30pm/V	<0.2dB/cm	<1ns	Yes	No
Silica	10^{-5}/K	<0.1dB/cm	200μs	No	Yes
SOI	TO: 1.7X10^{-4}/K EO: plasma dispersion	0.2dB/cm	TO:10μs EO: 10ns	No	Yes
III-V semiconductor	<10pm/V or plasma dispersion	0.5dB/cm	Pockel:<1ns Plasma dispersion: 10ns	Yes	Yes

1.3 Photonic Switch for Phased Array Antennas

Another important application of photonic switch is for optically controlled beam forming, in another word, phased array antenna systems (PAAs). PAA is a promising technology in modern civilian and military communication and targeting systems. PAA has the advantage of high directivity, quick beam steering without physical movement, reduced weight when compared to dish antennas, high bandwidth, low visibility, compact size, low electromagnetic interference, and simultaneous multimode operation (multi-targets) [13-14]. The schematic diagram of a linear phased array antenna is shown in Fig 1.4. Each antenna element is fed with a certain initial phase information, $\varphi+n\cdot\Delta\varphi$, and

transmits electromagnetic waves with different travel distances. These travel distance differences can make additional phases for different elements. All electromagnetic waves with different phases combine together and generate a *wave front* according to the phase relationship among the electromagnetic waves from different array elements. At the wave front, the EM waves transmitted by different array elements have the same phase information. The direction perpendicular to the PAA wave front is called the *scan direction* or radiation direction of the array antenna. The angle between scan direction and array normal direction is called the *steering angle*. For some PAAs, the steering angle changes with RF frequencies, which is usually called the *beam squint* effect.

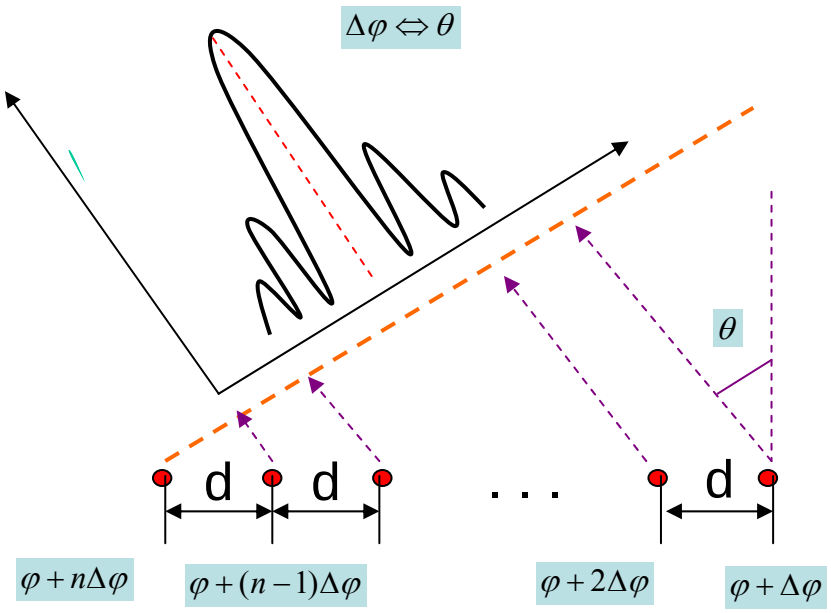

Fig. 1.4 Schematic diagram of phased-array antenna

For linear PAA systems with individual amplitude and phase controlled by radiating elements transmitting in air or free space, the electric field E in the far filed region along θ is [13-14]:

$$E(\theta,t) = \{\sum_{m=0}^{N} A_m \exp[\, i(\psi_m + kmd \sin\theta)]\} \exp(-i\omega t) \tag{1.2}$$

where t is time, N is the total array element number, A_m is the amplitude of m^{th} element, k is the wave vector with $k = 2\pi/\lambda$, λ is the RF wavelength, d is the array pitch, ω is the RF frequency, ψ_m is phase. For scanning angle θ,

$$\psi_m = -kmd \sin\theta \tag{1.3}$$

Conventional PAAs use phase shifters or phase trimmers to scan the radiation direction, which is usually of narrow bandwidth accompanied with beam squint effect, low EMI noise immunity, and bulky volume. Here beam squint means radiation direction shifts when the RF frequency changes with the relationship of

$$\Delta\theta = -\tan\theta_0\left(\frac{\Delta\omega_m}{\omega_m}\right) \tag{1.4}$$

where θ_0 is the initial radiation angle, and ω is RF angular frequency. Here it can be clearly seen that beam squint is proportional to the frequency change when using phase shifters, which results in narrow RF bandwidth. One solution to this problem is to use optical true time delay (TTD) techniques.

Optical true time delay for PAAs offers many advantages over electrical phase delays such as wide bandwidth, immunity to electro-magnetic interference (EMI) and compact size [15]. Compared with wavelength tuning configuration [16], an optically switched waveguide delay line device structure [17] needs no tunable wavelength sources, resulting in reduced system costs and enhanced resistance to harsh environments. Another delay device structure composed of optical MEMS switches and fiber delay lines [18] shows desirable features such as low insertion loss. A novel design based on MEMS and free space white cell also shows potential in terms of speed and scalability. However, either the fiber length has to be precisely cut or the mirrors have to be exactly assembled to achieve accurate delays.

A more attractive approach is to integrate waveguide switches and delay lines on a single chip by the PLC technique. A previously reported 2-bit true time delay configuration using polymer optical switches and waveguide delay lines [19], which are defined by photolithography, can precisely deliver four true time delays. The fully

integrated photonic circuit eliminates the discrete couplings between optical switches and fibers, therefore, it provides a more stable throughput and occupies less space. Additionally, the fabrication cost is significantly reduced.

A proposed 1×N PAA sub-array system structure is shown in Fig 1.5. A high speed optical modulator transfers the RF signal onto the optical carrier wave from a constant wave (CW) laser. The modulated signal is split and fed into the photonic switch based TTD devices, providing the time delays for the beam steering, which are specified by the controlling electronics. After the appropriated time delay within the delay modules, the optical signals are converted into the corresponding electrical signals by a photodiode bank. The electrical signals are then connected to an array of antenna head. By changing the working status of the photonic switches, a 1-D digitized TTD can be obtained.

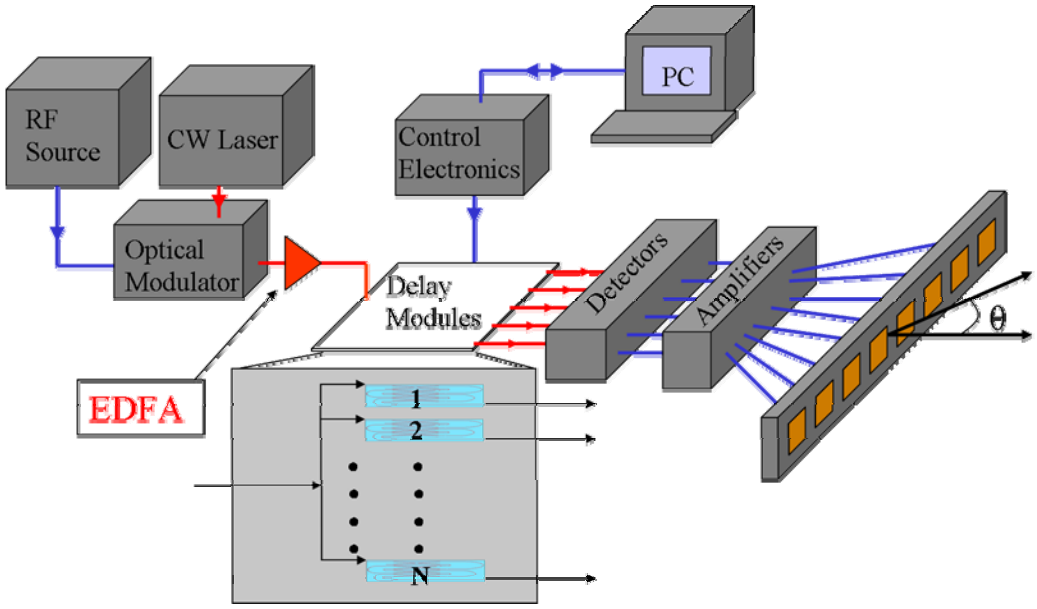

Fig 1.5 Schematic diagram of the 1×N phased array antenna sub-array system. (RF: radio frequency; EDFA: erbium doped fiber amplifier)

1.4 Overview of Board Level Optical Interconnects

Optics dominates electronics in backbone, metro and even local communication networks, which is an inarguable reality. However, electrical interconnects still takes the leading role in short distance reach, such as computer to computer, board to board, chip to chip and transistor to transistor inside a chip. Electrical interconnects has the unique features such as ease of deployment, low cost, free of interface problem.

However, the speed and complexity of integrated circuits are increasing rapidly as integrated circuit technology advances from very-large-scale integrated (VLSI) circuits to ultra-large-scale integrated (ULSI) circuits. The number of devices per chip, the number of chips per board, the modulation speed, and the degree of integration continues to increase. The International Technology Roadmap for Semiconductors (ITRS) expects that on-chip local clock speed will constantly increase to 10 GHz by the year 2011[20]. Fig 1.6 shows the increasing bit rates of different chips by the year of 2020.

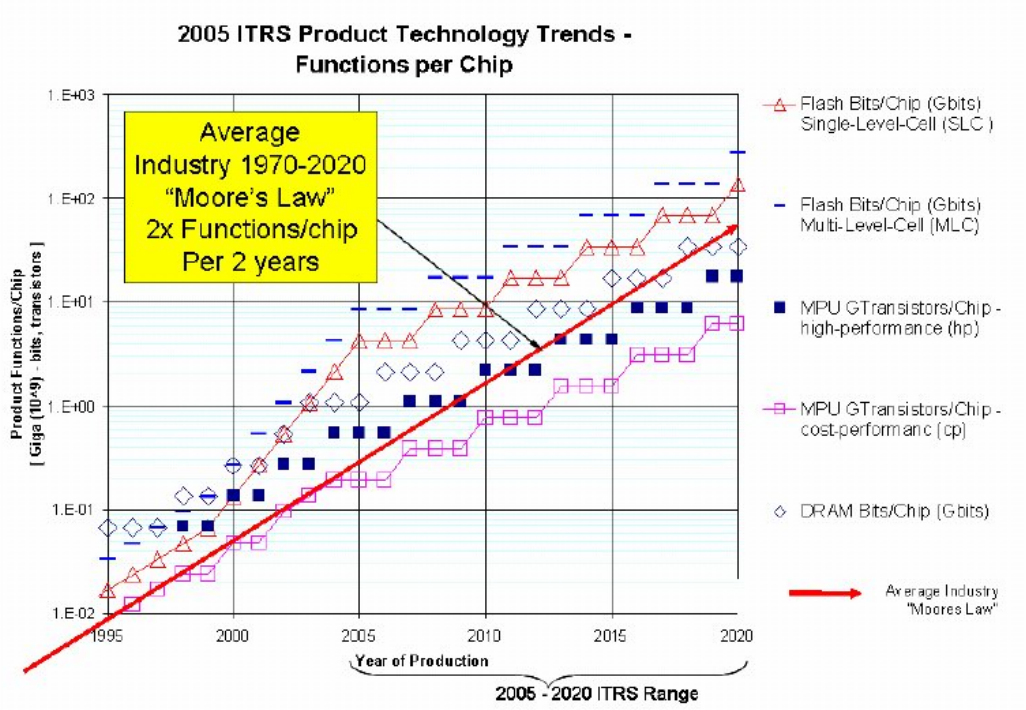

Fig.1.6 On-chip bit rates predicted by ITRS

Accordingly, the backplane frequency will boost proportionally. The third-generation I/O protocol called PCI Express, developed by the Signal Interest Group (SIG)

consortium, is becoming an industry standard [21]. PCI Express is expected to increase transfer rates up to 10GHz in the next 7-10 years. Beyond 10GHz, copper interconnects on PCB made of FR4 material, become bandwidth limited due to losses such as the skin effect in the conductors and the dielectric loss from the substrate material. Figure 1.7 shows simulated data of frequency-dependent loss for a 20-inch long electrical interconnect link for a situation found in a blade-based server configuration. The result includes the effect of packages, pad capacitance, via inductance, and connectors, in addition to the loss associated with the traces in FR4 material [22]. At 10 GHz the simulation for this link predicts an insertion loss of ~50 dB in a standard FR4 material.

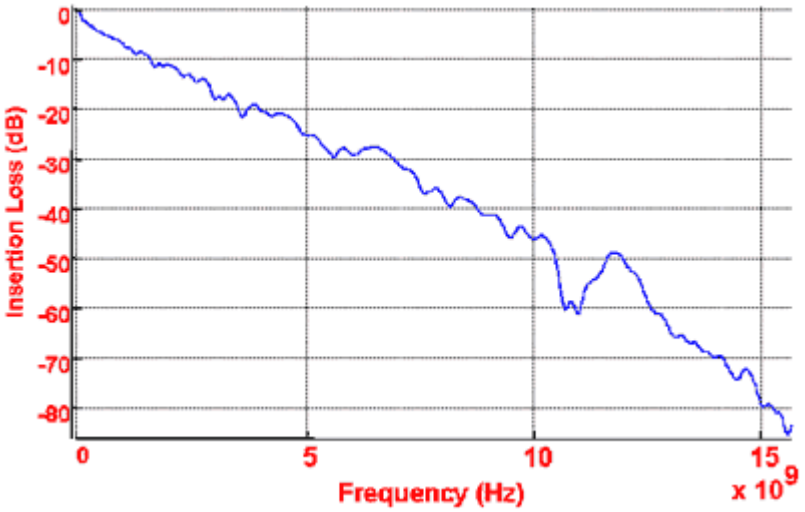

Fig 1.7 Projected channel loss for electrical link

It has been reported that replacing the FR4 material with newer laminates such as Rogers 4000 can extend the bandwidth of electrical interconnects to 7.7Gbps, but increase the cost by five times [23]. Besides the cost issue, a much worse situation for electrical interconnects was brought in by the unsolvable frequency dependent loss. To compensate the frequency dependent loss, very complex equalization technologies using equalization, pre-emphasis, and multi-level encoding techniques [24] are employed. The effects of reflections and crosstalk on the performance of electrical interconnect can pose other challenges for interconnect designers as the data rate increases beyond 10 GHz.

Optical solutions, which are widely agreed as a better alternative to upgrade the system performance, have been proposed for the upcoming electrical interconnect bottleneck for over 20 years [25]. Optical interconnects preponderate over the copper links in immunity to electromagnetic interference, independency to impedance mismatch, less power consumption, and high speed operation. Many optical interconnects schemes have been proposed and investigated. We will survey several typical implementations.

Figure 1.8 depicts an example of free space interconnects [26]. A space between two circuit boards or a circuit board and optical interface board is purely empty; so, it is called free space. Light signals coming out from the sources propagate to designated location on the other substrate. The architecture is simple; however, realization is very difficult. All optical components should be mounted at precise location. Moreover, two substrates should be mounted on the designated place, exactly. If reflective optical components are used, mounting accuracy should be doubled by nature. Another disadvantage of the free space interconnects is that the system is vulnerability to external environment such as vibration, and dust. Maintenance of the system is extremely difficult, also.

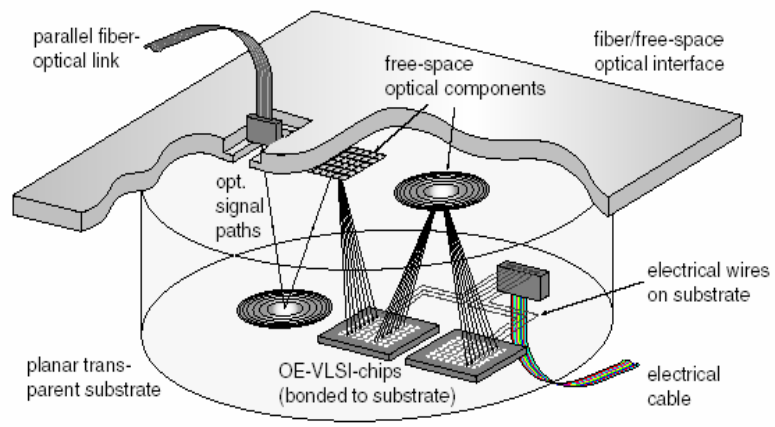

Figure 1.8 Illustration of free space optical interconnect [from M. Gruber [26]].

A high-coupling-efficiency optical interconnection has been demonstrated using a 90º bent fiber array connector to deflect beams between surface-emitting lasers or

surface-receiving photodiodes and optical layers embedded in a board [27], as depicted in Fig.1.9 (a). A 90º bent fiber array is mounted in a tetragonal body with a millimeter scale size to make it suitable for passive packaging in the board. The bending radius of silica fibers in the connector was controlled to have 1.5 mm resulting in bending loss of about 0.5 dB. An optical link of 2.5Gb/s signals with a total interconnection loss of 1.3 dB was demonstrated using the connectors and a fiber-embedded board. Fig.1.9(b) is the laminated fiber array inside PCB layers. The embedded fiber array will provide a stable and low loss link between the transceivers, however, as Fig1.9(a) shows, the vertical cavity surface emitting laser (VCSEL) and photodiode arrays are still located above the PCB, and wire bonded to the electrical drivers. The reliability and interface concerns are not completely removed.

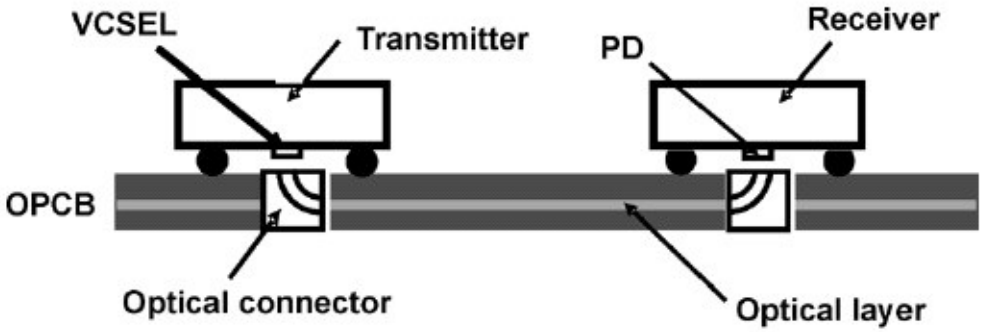

Fig 1.9(a) Schematic of the embedded fiber optical interconnects

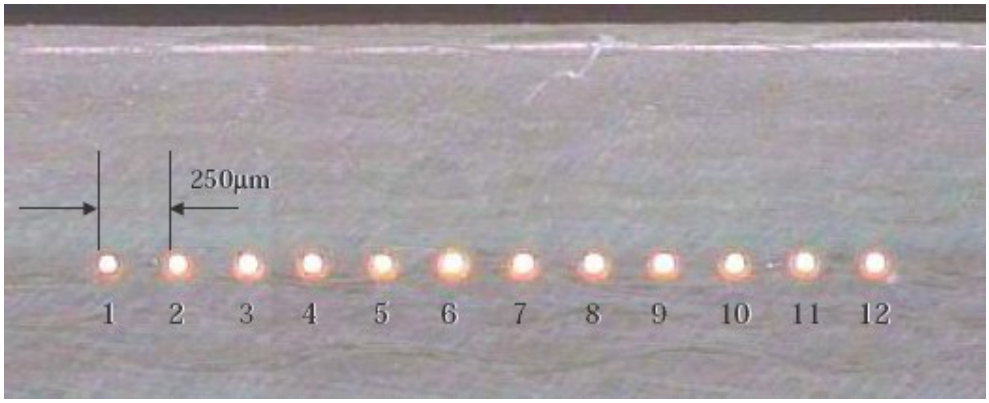

Fig 1.9(b) Cross section view of the PCB with embedded fiber array

There are many other implementations using polymer waveguides [28-30] instead of the embedded fiber array to achieve lower fabrication cost. Using polymer waveguide offers another advantage to integrate 45º micro-mirrors, which will improve the coupling efficiency between the waveguide and the active optical components. The waveguide layer and electrical layers are fabricated separately and then laminated together. Optoelectronic devices like VCSELs and PIN-PD are mounted on the top of the hybrid PCB. Fig 1.10 shows the concept of Optical PCB (OPCB) proposed by Yuzo Ishii and *et.al* [31]. The optical devices are directly coupled to the waveguide via 45º turning mirror. By doing so, vulnerability can be reduced. However, there is still an alignment problem. After laminating the boards, optoelectronic components should be aligned precisely at designated locations. This procedure is the most difficult part. The end of the waveguide was blocked from the line of sight by device itself. This alignment difficulty can be eased a little by increasing the size of the waveguide. Another shortcoming of these approaches is that optoelectronic devices occupy real estate of board.

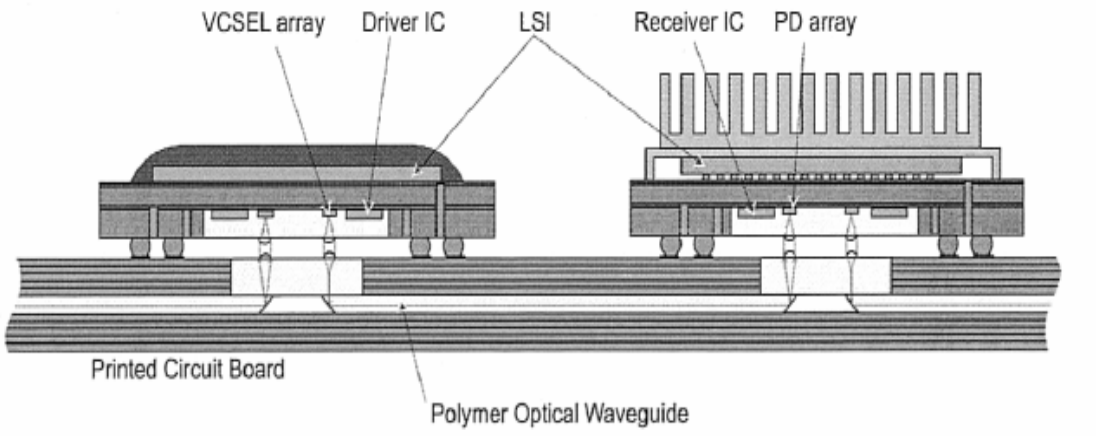

Fig 1.10 Illustration of optical-I/O chip packaging concept [from Yuzo Ishii and *et.al.* [31]].

However, none of them can provide a seamless interface with electrical components. For example, the board level optical interconnections reported in [32] piled up lasers, detectors and microlens on the surface of the board. The difficulties regarding packaging, multilayer technology, and reliability still remain to be solved.

1.5 Fully Embedded Board Level Optical Interconnects

We proposed a large field size (up to 2 feet x3 feet) molded polymer waveguide layer containing waveguides, waveguide couplers, thin film lasers, and thin film detectors with a cost-effective connectorization approach to peripherals on a flexible substrate [33-35]. The proposed approach with a fully embedded structure is anticipated to overcome the technical and cost barriers that prohibit the realization of optical interconnects in both inter- and intra-board levels. The fully embedded architecture totally separates the optical layer on a polymer film with the ectronic layer, and electrical-to-optical and optical-to-electrical signal conversions are realized using electrical vias. Therefore, packaging compatibility can be realized. The end users observe the pronounced performance upgrade due to the insertion of fully embedded optical interconnection proposed herein, but do not share the headache of optoelectronic packaging, a serious stumbling block for the realization of optical interconnect systems.

The architecture of the fully embedded optical layer includes a VCSELs array, a p-i-n photodiode array, surface-normal micro-mirrors, and a polymeric channel waveguide functioning as the physical layer of optical interconnection, as depicted in Fig 1.11. The driving electrical signals to modulate the VCSELs and the demodulated signals received at the photodiode flow through electrical vias connecting to the surface of the PC board. Within the optical interconnect layer, the light from the VCSELs is coupled into/out of the waveguide through 45° micro-mirror couplers and travels in the polymer waveguide. The fully embedded structure makes the insertion of optoelectronic components into microelectronic systems much more realistic when considering the fact that the major stumbling block for implementing optical interconnection onto high-performance microelectronics is the packaging incompatibility.

To fulfill the embedded structure, two major stumbling blocks need to be solved. A low cost, high performance optical layer on a polymer thin film remains the first; Packaging the optical layer through via holes and laminating it inside PCB layers counts the second. The research work presented in this disertation will relieve the concerns for

the first major block, and is believed to accelerate the deployment of fully embedded optical interconnects architecture based on the proposed structure with later effort.

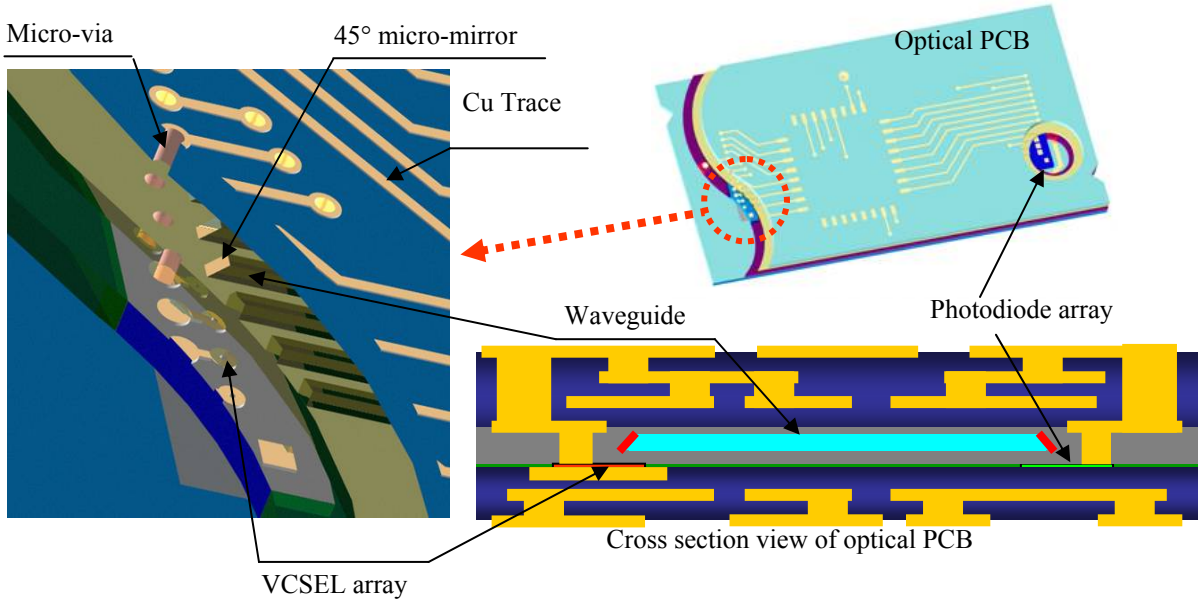

Fig 1.11Illustration of fully embedded optical interconnect architecture

1.6 Research Contributions

The major contributions of this dissertation are summarized below:

- Optimized the design and fabrication of 2X2 polymer based thermo-optic switches based on TIR effect in the aspect of thermal management and optical transmission. The measured results are comparable to the performance to commercialized polymer optical switches in terms of insertion loss, cross talk and polarization dependent loss, but outperform in device length, power consumption, and switching speed. The wavelength coverage from 630nm to 1600nm, as we called all-wave coverage is the most unique feature of the optical switch.
- Designed and fabricated a 4X4 optical switch matrix based on the cross-bar structure. The device obtained an ultra compact size, when compared with other structures.

- Integrate the TIR optical switches and polymer waveguide delay lines on a single chip with PLC technique. The fabricated 4-bit TTD module can dynamically deliver 16 delays from 0~177ps. The RF signal phase error attributed by the optical switch cross talk is investigated, and proved to be negligible.
- Fabrication process for large cross section multimode waveguide array by silicon hard molding process was investigated. A 51-cm long waveguide array by hot embossing method, which is the longest molding waveguide that has ever been reported, was successfully demonstrated with -15.1dB insertion and 150GHz optical bandwidth.
- The coupling efficiency of the 45º micro-mirror was theoretically studied using M^2 factor revised Gaussian beam method. The mirror was also experimentally achieved through a one-step pattern transfer molding process, and obtained a coupling efficiency as high as 85%.
- The integration of the optoelectronics device with the optical waveguide array is explored. With a simplified integration scheme, the VCSELs and photodiode array are integrated to the thin film waveguide, and successfully demonstrated 12X2.5Gbps signal transmission.

1.7 Dissertation Layout

In Chapter 1, basic concepts of photonic switching, true time delay, and board level optical interconnects are introduced.

In Chapter 2, the design for a 2X2 TIR optical switch, from both optics and thermal management, is presented. The material relaxation induced cross talk is investigated and compensated by increasing the half branch angle. The fabricated devices are fully tested and detailed performance is also presented. The 2X2 TIR switches are expanded to build up a 4X4 switch matrix with an ultra-compact size.

In Chapter 3, a 4-bit optical TTD module using integrated optical switches and waveguide delay lines are presented. The process integrations are discussed, followed by

the testing result of the device. The RF phase noise induced by the optical switch cross talk is theoretically studied, and confirmed by experimental results to be negligible.

Chapter 4 describes the fabrication procedure of large cross section waveguide array with silicon hard molding process. The surface smoothing techniques using oxidation and spin coating method are described. The measured optical properties of the molded waveguide array are also presented.

In the last chapter, the design and fabrication of the 45º micro-mirror is given in details. The system integration of waveguides, micro-mirrors, VCSELs and photodiodes are investigated. The signal transmission over the prototype system is successfully demonstrated.

1.8 References

[1] http://www.labs.nec.co.jp/Eng/Topics/data/r010322/

[2] M. Okuno, "Highly integrated PLC-type optical switches for OADM and OXC systems," in Proc. Optical Fiber Communications Conf., Atlanta, GA, Mar. 2003, vol. 1, pp. 169–170.

[3] Giles, C.R. Aksyuk, V. Barber, B. Ruel, R. Stulz, L. Bishop, D. "A silicon MEMS optical switch attenuator and its use in lightwavesubsystems," IEEE Journal of Selected Topics in Quantum Electronics, Vol.5, No.1, pp.18-25, 1999.

[4] Hattori, K. Fukui, M. Jinno, M. Oguma, M. Oguchi, K. "PLC-based optical add/drop switch with automatic level control," IEEE Journal of Lightwave Technology, Vol.17, No.12, pp.2563-2571, 1999

[5] http://physics.pdx.edu/~larosaa/Agilent_All_Optical_Network.htm

[6] Q. Lai, W. Hunziker, and H. Melchior, "Low-power compact 2 × 2 thermooptic silica-on-silicon waveguide switch with fast response," IEEE Photon. Technol. Lett., vol. 10, no. 5, pp. 681–683, May 1998.

[7] R.V.Schmidt, R.C.Alferness, "Directional Coupler Switches, Modulators and Filters using Alternating ΔβTechniques", IEEE Transactions on Circuit and Systems, Vol.26, No.12, 1979: pp.1099-1108

[8] Y.Silberberg, P.Perimutter and J.E.Baran, "Digital Optical Switch", Applied Physics Letters, Vol.51, No.16, 1987: pp1230-1232

[9] W.K.Burns, and A.F.Milton, "An Analytic Solution for Mode Coupling in Optical Waveguide Branches", IEEE Journal of Quantum Electronics, Vol.16, No.4, 1980: pp446-454

[10] Li, Bing; Tang, Suning; Taboada, John M.; An, Dechang; Shi, Zan; Li, Bulang; Chen, Ray T.,"
Proc. SPIE Vol. 4225, p. 0-9, Optical Interconnects for Telecommunication and Data Communications

[11] A.Yeniay, R.Gao, K.Takayama, and A.F.Garito, IEEE J.Lightwave Technol., Vol.22, No.1, pp.154-158, 2004

[12] Y. Hida, H.Onose, S.Imamura, IEEE Photonics Technology Letters, Vol.5, No.7, pp.782-784, 1993

[13] C.A. Balanis, *Antenna theory: Analysis and design*, 3rd Edition, John Wiley & Sons, 2005

[14] R. C. Hansen, *Phased array antennas*, Wiley-Interscience, 1998

[15] W.Ng, A.Walston, L. Tangonan, J. J. Lee, I. Newberg, and N. Bernstein, "The first demonstration of an optically steered microwave phased array antenna using true-time-delay," *J. Lightwave. Technol.*, vol. 9, no. 9, pp.1124–1131, Sep. 1991.

[16] Z. Shi, Y. Jiang, B. Howley, Y.Chen, F. Zhao, and R.T. Chen, "Continuously Delay-Time Tunable-Waveguide Hologram Module for X-Band Phased-Array Antenna", *IEEE Photon. Technol. Lett.*, vol.15, pp.972-974, July, 2003

[17] K.Horikawa, I.Ogawa, H.Ogawa, and T.Kitoh, "Photonic switched true time delay beam forming network integrated on silica waveguide circuits,," in *IEEE MTT-S Int.*, vol. 1, May 16–20, 1995, pp. 65–68.

[18] J.D.Shin, B.S.Lee, and B.G.Kim, "Optical true time-delay feeder for X-band phased array antennas composed of 2×2 optical MEMS switches and fiber delay lines", *IEEE Photon. Technol. Lett.*, vol.16, pp.1364-1365, May, 2004

[19] B.Howley, Y.Chen, X.Wang, and Ray T.Chen, "2-bit Reconfigurable true time delay lines using 2×2 polymer waveguide switches," *IEEE Photon. Technol. Lett.*, vol.17, pp.1944-1946, Sep. 2005

[20] International SEMATECH, "The National Technology Roadmap for Semiconductors (ITRS)—Technology Needs," Semiconductor Industry Association, 2005.

[21] S. Berry, "Advanced Bus and Interface Market and Trends," *Electronic Trend Publication Inc.*, September 2003.

[22] http://www.intel.com/technology/itj/2004/volume08issue02/art04_interconnect/p02_intro.htm

[23] D. Huang, T. Sze, A. Landin, R. Lytel, and H.L. Davidson, "Optical interconnects: Out of the box forever?" *IEEE J. Sel. Top. Quan. Elec*., vol. 9, no. 2, pp. 614-623, 2003.

[24] R. Mooney. Intel internal document on equalization.

[25] J.W.Goodman, F.I.Leonberger, S.Y.Kung, and R.A.Athale, "Optical Interconnections for VLSI Systems," *Proc. IEEE*, vol. 72, no. 7, pp. 850-866, July 1984

[26] M. Gruber, S. Sinzinger, and J. Jahns, "Optoelectronic multichip module based on planar-integrated free-space optics," Proc. SPIE, Optics in Computing2000, **4089**, (2000)

[27] Mu Hee Cho, Sung Hwan Hwang, Han Seo Cho, and Hyo-Hoon Park, "High-Coupling-Efficiency Optical Interconnection Using a 90 -Bent Fiber Array Connector in Optical Printed Circuit Boards," IEEE Photonics Technology Letters, Vol.17, No.3, pp.690-692, 2005

[28] I.K.Cho, K.B.Yoon, S.H.Ahn, and H.K.Sung, “Experimental demonstration of 10Gbit/s transmission with an optical backplane system using optical slots”, Optics Letters, 30,pp.1635-1637, 2005

[29] Elmar Griese, “A High-Performance Hybrid Electrical–Optical Interconnection Technology for High-Speed Electronic Systems,” IEEE TRANSACTIONS ON ADVANCED PACKAGING, VOL. 24, NO. 3, pp. 375-383, 2001

[30] Takashi Sakamoto, Hiroyuki Tsuda, Member, Makoto Hikita, Member, Toshiaki Kagawa, Kouta Tateno, and Chikara Amano, “Optical Interconnection Using VCSELs and Polymeric Waveguide Circuits,” JOURNAL OF LIGHTWAVE TECHNOLOGY, VOL. 18, NO. 11, pp.1487-1492, 2000

[31] Yuzo Ishii, Shinji Koike, Yoshimitsu aria, and Yasuhiro Ando, “SMT-Compatible Optical I/O Chip Packaging for Chip-Level Optical Interconnects,” Elec. Components and Technology Conf. 2001

[32] Eva M. Strzelecka, Duane A. Louderback, Brian J. Thibeault, Geoff B. Thompson, Kent Bertilsson, and Larry A. Coldren, “Parallel free-space optical interconnect based on arrays of vertical-cavity lasers and detectors with monolithic microlenses”, Applied Optics, 37, pp.2811-2821, 1998

[33] Choi, C.; Lin, L.; Yujie Liu; Jinho Choi; Li Wang; Haas, D.; Magera, J.; Chen, R.T., “Flexible optical waveguide film fabrications and optoelectronic devices integration for fully embedded board-level optical interconnects,” Lightwave Technology, Journal of ,Volume: 22 , Issue: 9 , pp.2168 - 2176, 2004

[34] Choi C, Lin L, Liu YJ, Chen RT, “Performance analysis of 10-mu m-thick VCSEL array in fully embedded board level guided-wave optoelectronic interconnects,” ,J LIGHTWAVE TECHNOL 21 (6): pp.1531-1535, 2003

[35] R.T.Chen, L.Lin, C.Choi, Y.Liu, B.Bihari, L.Wu, S.Tang, R.Wickman, B.Picor, M.K.Hibbs-brenner, J.Bristow, and Y.S.Liu, “Fully Embedded Board-Level Guided Wave Optoelectronic Interconnects”, Proc. Of the IEEE, 88,6, pp.780-794, 2000

Chapter 2 Polymer based Thermo-optic Switch using Total Internal Reflection Effect

In this chapter, the optimized design of the 2X2 TIR switch, including the geometric parameter optimization and thermal management are presented. The device performance, especially the cross talk, which is seriously affected by the relaxation phenomena of the polymer materials, is significantly improved with the effort of optical design compensation. 4X4 switch matrix based on cross-bar topology is also presented.

2.1 Working Principle of the 2X2 TIR Optical Switch

Polymers are an ideal choice for a platform to integrate various passive optical devices, such as optical switches, AWGs, VOAs or power couplers. This low-cost material can be easily manipulated by methods such as molding, sawing and dry etching [1]. Additionally, polymers have a large polarization independent thermo-optic (TO) effect, which is one order greater than that of silica. In spite of a relatively slower response compared to electro-optic devices, the simpler fabrication procedure and more reliable performance of TO devices have kept them popular and commercially available in recent years.

The TO effect of polymeric materials is negative, i.e., the refractive index of the polymer decreases as the temperature rises. Thus, a total internal reflection (TIR) optical switch can be formed if a heater is set at the crossing point of a symmetric X junction [2][3][4]. As Fig 2.1 shows, the incident light is launched from one of the input waveguides. If no action is taken, the light will pass the junction in a straight line to corresponding output waveguide, which is called the cross state. However, if the heater raised the local temperature by joule heat, the refractive index of the polymer in the junction will decrease and the incident light will be reflected to the opposite waveguide, called the bar state. Compared with various TO switch configurations, such as a digital optical switch (DOS) [5], a Mach-Zehnder interferometer (MZI) switch[6], or a

directional coupler switch[7], TIR switches have a significant advantage in their broad optical bandwidth, or equivalently, their wavelength insensitivity.

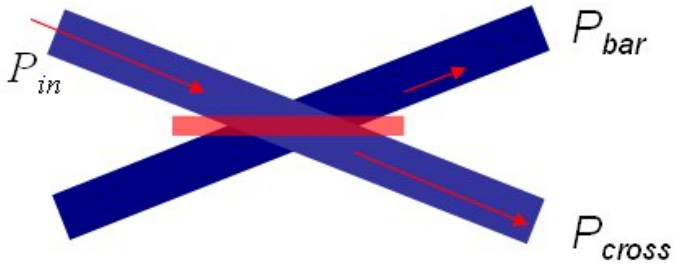

Fig 2.1 Schematic of the 2X2 TIR optical switch

2.2 Optimized Design of the TIR switch

2.2.1 Optical design

The design of a TIR TO switch deals with two major issues: optical and thermal characteristics. Some general concepts are discussed in ref [4]. Fig 2.2 shows the schematic diagram of the TO TIR switch. The refractive indices of the cladding and core used in the simulation are 1.45 and 1.46 respectively, corresponding to the actual materials used. The waveguide dimension is 6.5 × 6.5μm2. The separation of the input/output waveguide is 250μm, which is compatible with a standard fiber array. The radii (R) of the bend waveguides are fixed at 10mm, which is large enough such that negligible bending loss and guided mode perturbation result. The bend waveguides are then connected by two straight waveguides to form an X junction. Horn structures are introduced near the junction area for two purposes: to reduce the cross talk and to make it compatible with the temperature gradient. The electrode heater, formed by a thin layer of gold film, is shortened and narrowed to reduce the power consumption compared with ref [3]. The electrode heater is connected to two enlarged pads by tapered lead lines. With this structure, the lead resistance can be reduced and the heating efficiency can be improved.

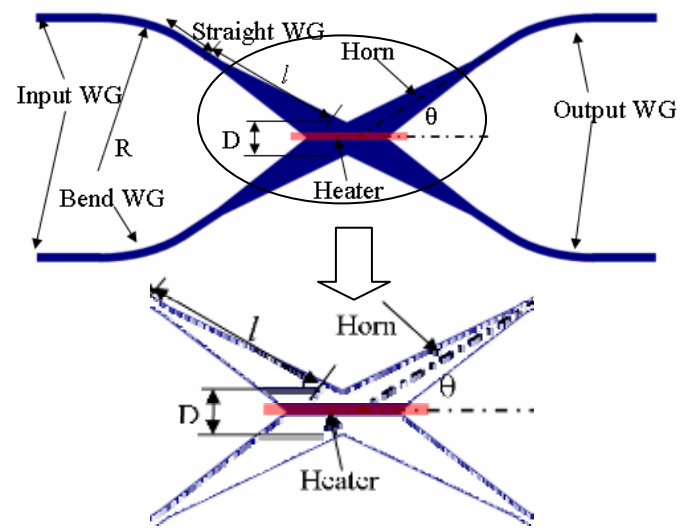

Fig 2.2 Schematic diagram of the TO TIR switch

To improve the performance of the switches, the paramount concern is the geometric parameters of the X junction. 3-dimentional semi-vector beam propagation method (3-D SV BPM) [8] is employed in this investigation. If the half branch angle of the junction is θ, the effective length of the switch, namely, the total device length excluding the input/output waveguides, is determined by

$$L = 2\left\{\frac{\left[\frac{P}{2} - R(1-\cos\theta)\right]}{\tan\theta} + R\sin\theta\right\} \tag{2. 1}$$

The length of the horn structure l can vary from 0 to $l_{\max}$, where

$$l_{\max} = \frac{\left[\frac{P}{2} - R(1-\cos\theta)\right]}{\sin\theta} \tag{2.2}$$

The most critical parameters are the taper length l, the junction width D, and the half branch angle θ. In order to optimize these three parameters, two of them are fixed and the third is determined. All simulations in this paper are based on the TE mode. Since both the switch structure and the TO effect are polarization independent, the TM mode shows the same behavior as the TE mode.

First, D and θ are set at 50μm and 4° based on our previous experimental result to determine l. Fig 2.3 (a) shows the excess loss and cross talk as functions of l. Excess loss represents the loss caused by the switch structure excluding the coupling loss, material absorption and Fresnel reflections. The simulation result in Fig 2.3 (a) shows that longer l leads to lower excess loss and lower cross talk. For example, at the maximum length, where $l_{\max} = 1442\mu m$, the excess loss is 0.96dB and the cross talk is below -44dB. In later simulations, l= l_{max} will be adopted. A direct explanation for this result is that longer taper length causes smoother adiabatic mode transformation from the straight waveguide to the horn structure [12]. Fig 2.3(b) shows the excess loss and cross talk as functions of D, when $l = 1442\mu m$ and θ=4°. A compromise has to be made to obtain a low excess loss as well as low cross talk. We conclude based on the simulation that 40-50μm is a good range because it also fits the requirement of the temperature gradient, which will be discussed in the next part. Fig 2.3(c) shows the variation of the excess loss and cross talk with θ. With the increase of θ, both the excess loss and cross talk will decrease. However, with the increase of θ, more driving power has to be applied to switch the light, which will eventually burn the device. Thermal simulations show that if θ>6°, the electrode heater temperature has to be greater than 251℃.

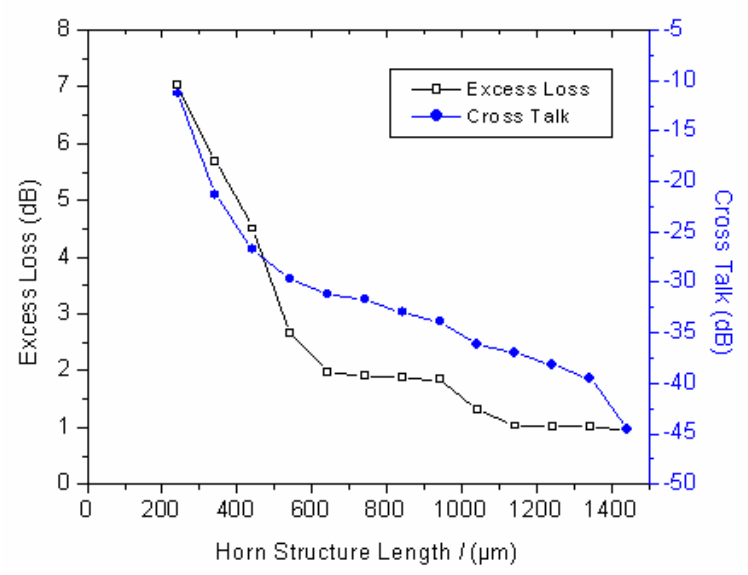

Fig.2.3 (a)

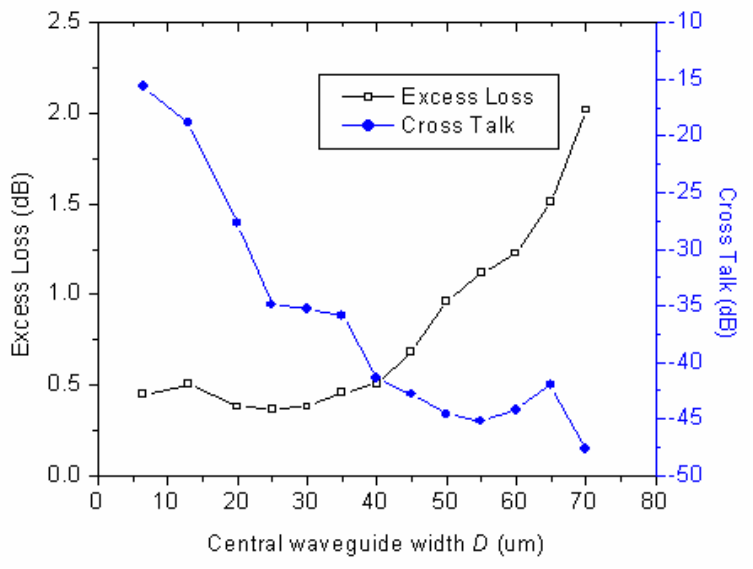

Fig.2.3(b)

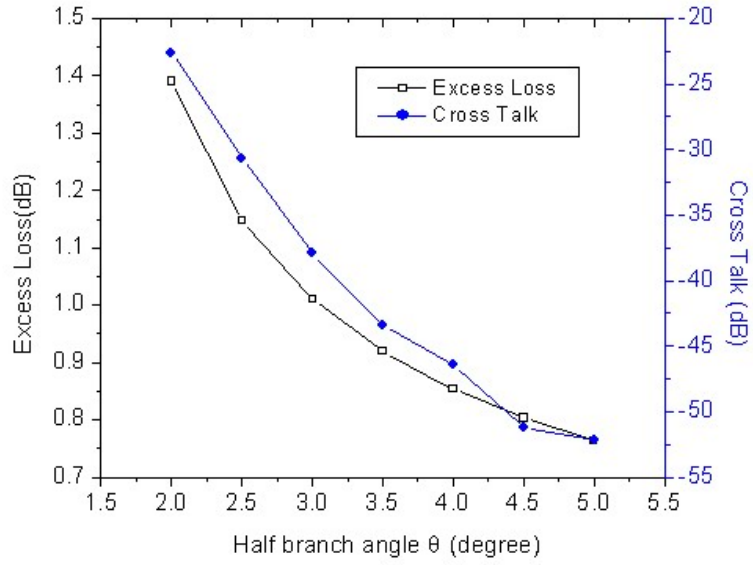

Fig.2.3(c)

Fig 2.3 The simulated excess loss and cross talk as functions of the (a)horn structure length (b)junction width (c)half branch angle

2.2.2 Thermal Management

The heating structure shown in Fig 2.2 is quite similar to the model in ref [10]. The temperature of the electrode heater, which can be considered to be infinitely long compared with the electrode width, was given in ref [10]

$$T = T_a + \frac{J^2 \rho_0}{\frac{K_i}{tt_i}[1 + 0.88t_i / w] - J^2 \rho_0 \beta} \tag{2.3}$$

where Ta is the ambient temperature, J is the current density, ρ0 is the resistivity of the metal, β is the temperature coefficient of the resistivity (ignored here), t is the metal thickness, w is the metal line width, and Ki is the thermal conductivity of the polymer. The density of the polymer used in this paper is ρ=1.0 g/cm3, the specific heat is c=0.84J/g·K and the thermal conductivity is $K=2\times10^{-3}$W/cm·K. Eqn. (2.3) can then be written in a simpler form:

$$T = T_a + \frac{P_0 / l_{ele}}{K_i (w / t_i + 0.88)} \tag{2.4}$$

where P0 is the heating power, and lele is the length of the electrode heater. Eqn. (2.3) and (2.4) are only valid if lele>>w, which allows the two-dimensional model approximation. The case under here consideration is P_0=44mW, l_{ele}=1500μm, w=8μm, t_i=18μm, T_a=25℃, resulting in a T=125.6℃. This case corresponds to the fabricated device discussed in Part IV.

However, what we are most concerned with is the temperature of the polymer rather than the electrode heater. Thus, numerical simulations using the finite element analysis (FEA) method have to be carried out to solve the 2-D thermal conduction equation. Fig 2.4 shows the three-layer active region that will be analyzed. The geometry is simplified by approximating the central convex waveguide as a planar layer, since we use a thick top cladding (>8μm) to reduce metal absorption and since the junction width is significantly greater than the temperature extension width. The parameters used to calculate the steady-state temperature distribution are the same condition as given above. The temperature at the electrode heater is 131℃, which is close to the temperature

derived by Eqn.(2.4). The simulation also indicates that along the mid-height of the core, the temperature resembles a Gaussian distribution.

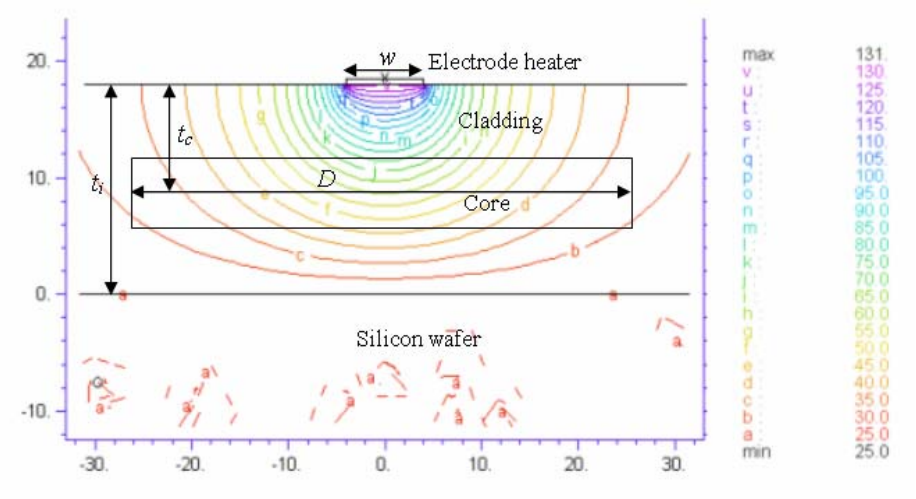

Fig 2.4 Thermal steady state simulation for the active region of temperature contour map

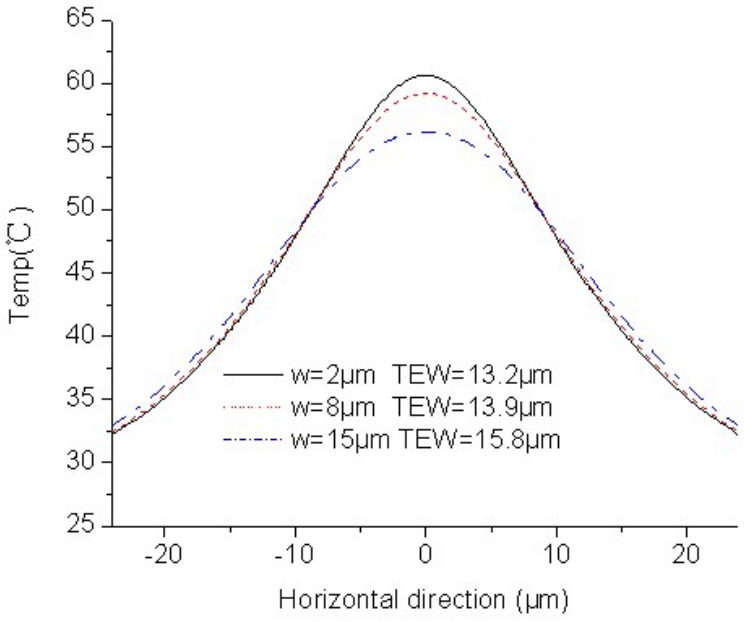

Fig 2.5 temperature distribution for different electrode width

Fig 2.5 shows the temperature distribution for various w, demonstrating that narrower electrode heater widths will lead to higher central waveguide temperatures and steeper temperature gradients, especially in the region right below the electrode heater.

We define the temperature extension width (TEW) as the distance to the waveguide center where ΔT is half of the maximum ΔT. A smaller temperature extension width represents a better heat confinement and higher heating efficiency. So, for a given change of the refractive index, a smaller width will require less driving power. However, some fabrication issues limit the narrowness of the electrodes. Since w=8μm does not yield a significant improvement over 2μm, w=8μm is adopted in the real fabrication.

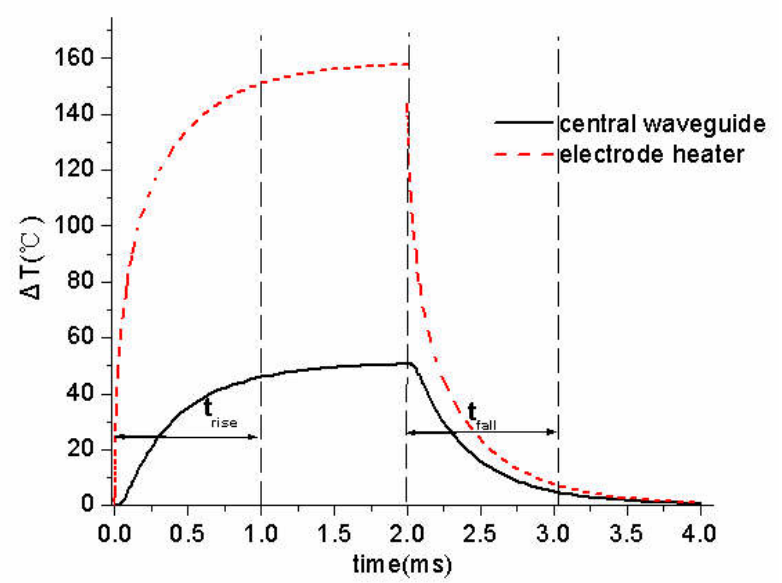

Fig 2.6 Transient thermal state for the active region of time domain temperature cycle

Fig 2.6 shows the transient temperature response of the electrode heater and central waveguide. We define t_{rise} as the time from 0 to 90% ΔT_{max} and t_{fall} as from ΔT_{max} to 10% ΔT_{max}. The simulated t_{rise} and t_{fall} are 1.0ms and 1.1ms, respectively, which are also the switching times for the TIR switch. The polymer thickness t_i has significant impact on the switching time. If the polymer thickness is decreased, the heat can easily go through the polymer film to the silicon wafer, which is a good thermal conductor, thus achieving a higher speed. However, the switch will also consume more driving power with a decrease in t_i.

Fig 2.7 shows how the switching time and the power consumption vary with ti. From this chart, we conclude that for a TIR switch with a half branch angle of 4°, the power consumption cannot be less than 38mW, which is determined by the heat sinking

rate of the polymer. The switching time cannot go below 5μs, being limited by the thermal response of the silicon wafer. Although we can make a TO switch with a switching time less than 10μs if ti<1μm, the optical loss will become intolerable due to the low coupling efficiency and the large metal and substrate absorption.

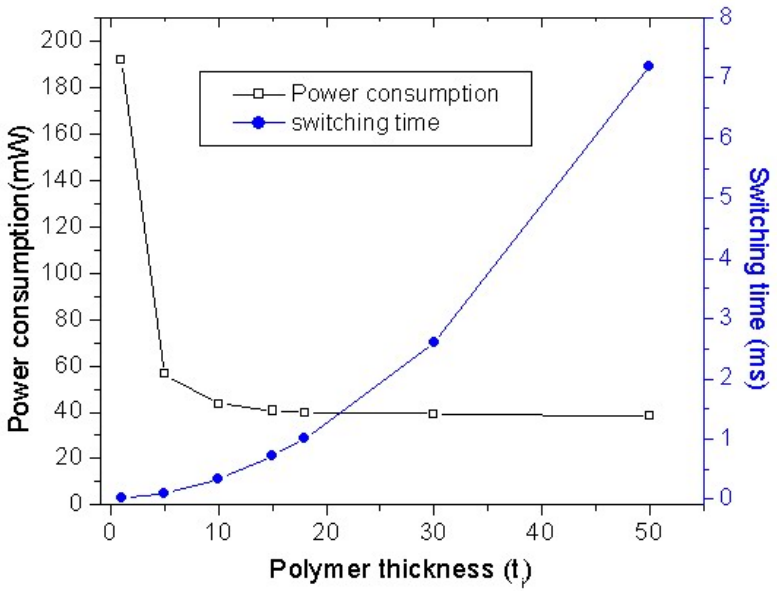

Fig 2.7 Switching time and power consumption as functions of polymer thickness

2.2.3 Reflection at the X Junction

One possible approach to evaluate the reflection phenomenon at the junction is to use the classical Goos-Hanchen theory for the collimated light reflection at interfaces, as in ref [11]. However, the refractive indices in the cross section resemble a graded distribution due to the thermal expansion. It is difficult to find a precise analytical solution for the mode profile. As an approximation, we assume a parabolic indices distribution as

$$n(x) = 1 - \frac{1}{2} a^2 (x - x_0)^2 \tag{2.5}$$

x is the direction vertical to the input waveguides in the waveguide plane, x0 is the mode center and a is the fitting coefficient. Using the Gauss-Hermite polynomials, the fundamental mode profile is [15]

$$\psi(x) = (\frac{ka}{\pi})^{1/4} \exp[-\frac{ka(x-x_0)^2}{2}] \qquad (2.6)$$

where $k = \frac{2\pi n}{\lambda}$ is the wave number in the optical media. Fig 2.8(a) shows the fundamental mode profiles for different wavelengths, suggesting that longer wavelengths will result in larger mode diameters. Hence the optical power leakage into the cross port will aggravate the excess loss and cross talk, resulting in the bandwidth limitation of the TIR structure. If the wavelength is very short, higher order modes will dominate the behavior, which will increase the radiation losses at the taper regions. Fig 2.8(b) shows how the performances vary with λ by 2D SV BPM simulations. If we require the excess loss to be less than 3dB and cross talk less than -25dB, the expected bandwidth is 4200nm (0.6μm-4.8μm), which is much broader than any conventional optical switch structures based on beam interference.

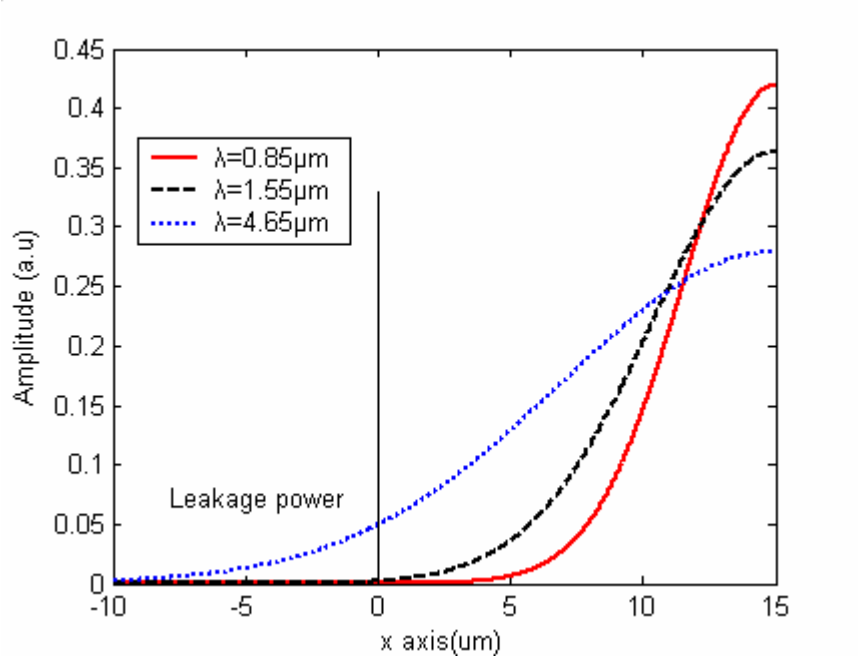

Fig 2.8(a)

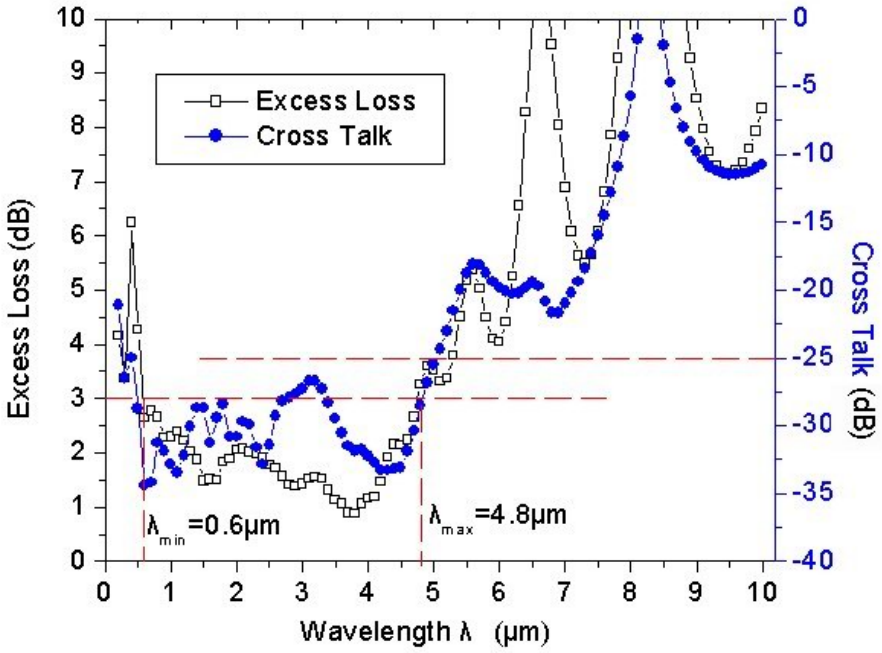

Fig 2.8(b)

Fig 2.8 (a) fundamental mode profiles of different wavelengths (b)simulated bandwidth of the TIR structure

2.3 Device Fabrication

ZPU12-RI series polymer materials with the TO coefficient of -1.7×10^{-4}/℃ from Chemoptics are employed to make optical waveguides on silicon wafers. First, a layer of ZPU12-450 (n=1.45) as the bottom cladding is spin coated onto the wafer. After UV and thermal curing, a second layer of ZPU12-460 (n=1.46) is spun which servers as the core layer. A suitable thickness of a hard masking material is then deposited and patterned by either a wet or dry etching method. Silicon dioxide (SiO2) is employed as the hard mask material because it has the ability to be dry etched with RIE plasma. The dry etch process yields smoother hard mask edges compared with wet etching, thereby reducing the roughness of the polymer waveguide sidewalls. But the conventional plasma enhanced chemical vapor deposition (PECVD) process to grow SiO2 requires a high temperature (285℃), which is quite close to the polymer degradation point (300℃). We developed a low temperature PECVD recipe running under 200℃, which is quite close to the thermal

baking temperature and will not cause undue material degradation loss. The measured propagation loss of the fabricated channel waveguide is 0.38dB/cm at a 1.55μm wavelength. This is close to the limit set by the material absorption, measured from the planar waveguide propagation loss, which is 0.35dB/cm. Once the hard mask is properly defined, RIE is used to form the channel waveguides in the core material. The remaining hard mask is then removed by wet etching and a polymer top cladding layer is spin coated and cured. Fig 2.9 shows a part of the core layer in the junction with smooth sidewalls produced by the RIE process. After words, a 300nm gold film is deposited on the top cladding and patterned by photolithography. Wet etching is used to form the electrode heater.

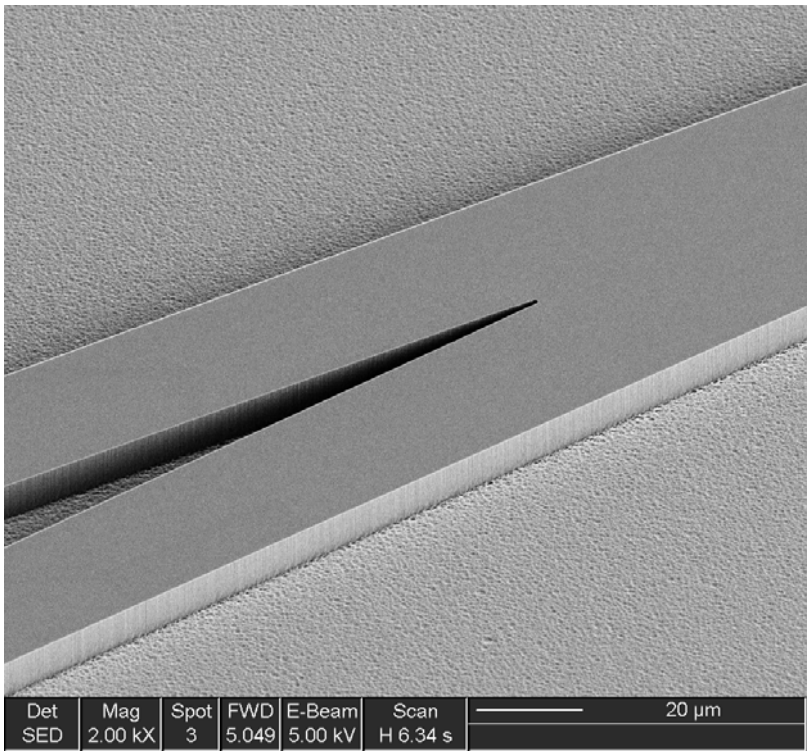

Fig 2.9 SEM of the core at the junction

Fig 2.10 shows the patterned electrode on top of the X junction. In the last step, the device is cleaved and the facets are polished to form a good coupling interface with a single mode fiber.

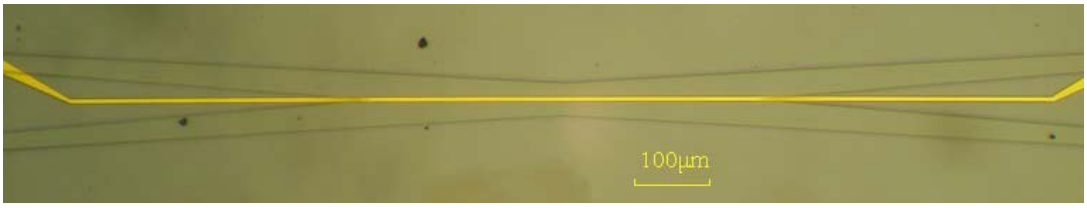

Fig 2.10 X junction with electrode heater

2.4 Testing Results of the 2X2 TIR Switch

2.4.1 Switching Characteristics

A Thorlabs ASE-FL 7001P broad band light source (1.53-1.61μm) is used to launch the light through a single mode fiber into the optical switches. Fig 2.11 shows the near field pattern of the TO switch in the cross and bar state, respectively. The mode profiles are composed of the fundamental modes with a separation of 250μm.

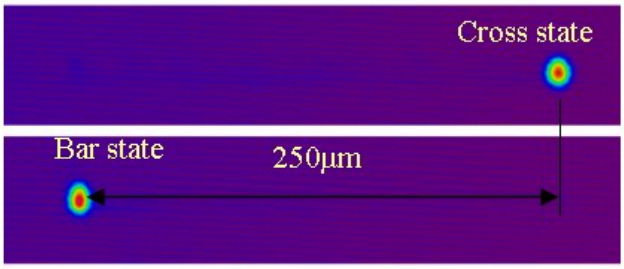

Fig 2.11 Near field patterns in cross and bar state

Fig 2.12 shows the optical power of the TE and TM modes in the cross port and the bar port responding to the driving power. The tested switch, with a half branch angle of 4°, has a cross talk of -32dB in the cross state, and a power consumption of 0mW. The zero static power consumption is a profitable feature since it can reduce the average driving power in real applications. With a driving power increase, the optical power in the cross port will decrease but in the bar port will increase simultaneously. Eventually, the switch will reach the bar state. Here, we define the driving power resulting in maximum optical power in the bar port as the bar state power consumption, which is 44mW in Fig 2.12, achieving a cross talk of -31dB. The TE and TM modes show almost the same response to the driving power. The polarization dependent loss (PDL) is 0.1dB in the

cross state and 0.2dB in the bar state. The measured total resistance including the pads and lead lines is 48.0Ω and the resistance of the heater is 39.1Ω, so that the thermal efficiency is estimated to be 81.5%.

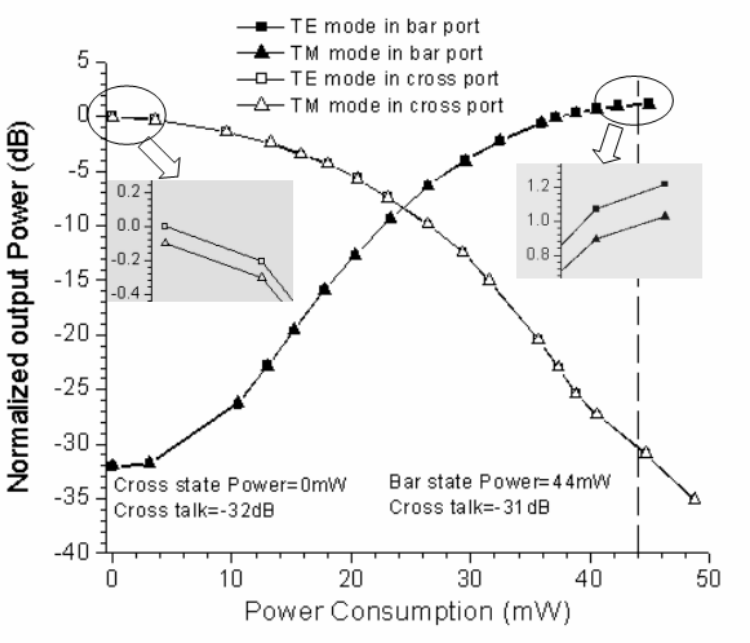

Fig 2.12 Switching characteristics of the TIR switch

The performance of the TIR switches for different values of θ is listed in Table 2.1.

Table 2.1 Performance of the TIR switches with different θ

θ (degree)	3	4	5
Effective Length(μm)	5294	4274	3731
Cross talk in cross state(dB)	-20	-31	-40
Cross talk in bar state(dB)	-23	-32	-41
Excess loss(dB)	1.3	0.9	1.4
Switching Power (mW)	25	44	66

For practical applications, the fiber to fiber insertion loss is more important than the excess loss. We shortened the input/output waveguide to reduce the propagation loss. With a total device length of 19mm, the lowest insertion loss we have achieved is 2.8dB.

2.4.2. Switching Time

The switching time of the TIR switch is determined by the thermal conductivity and thickness of the polymer. But for the loss issue (thinner polymer layer results in larger metal and substrate absorption), the total thickness is still around 18μm. Both our simulation and experimental results show that the switching time of the TIR TO switch is independent of the geometric parameters of the X junction. We used a 200Hz square waveform with an amplitude of 1.3V and an offset at 0.65V to drive the heater of the switch with a half branch angle of 4°. The dynamic power consumption is calculated to be 43.2mW, which is very close to the value in Table1. The optical response in the two output channels, as shown in Fig 2.13, demonstrates a delay of 1.5ms for t_{rise} and 2ms for t_{fall}. The measured speed is a little bit slower than the simulation results (1ms for t_{rise} and 1.1ms for t_{fall}), which is possibly caused by the approximation of the 2-D FEA model.

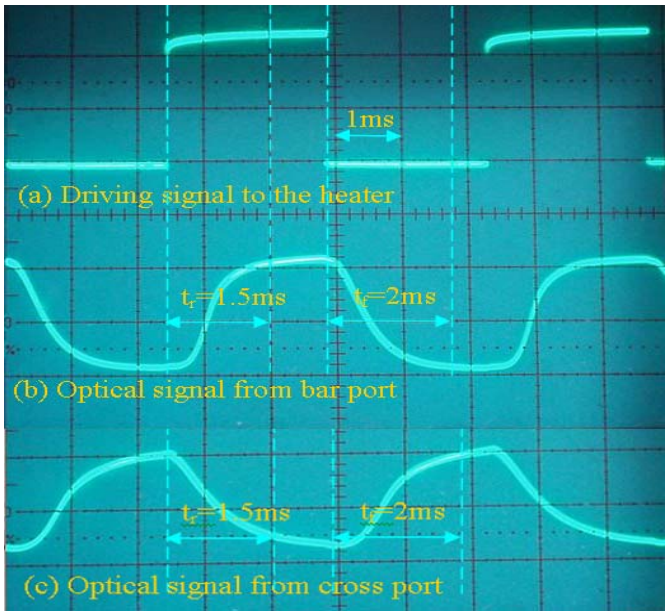

Fig 2.13 Dynamic response of the optical signal to the driving signal

2.4.3. Optical Bandwidth

The fabricated devices have good performance over the wavelengths from 1.53-1.61μm as described in Part IV A and B. To find the bandwidth limit, a white light source (AQ 4303-B) is used as the broadband supply. The bandwidth of the white light source

covers from 400-1800nm. In the cross state, the optical power from the cross port is monitored by the optical spectrum analyzer, as shown in Fig 2.14 by the dashed line. The optical power from the bar port is under the sensitivity of the spectrum analyzer, which is at least 20dB lower than that of the cross port. When a driving power is applied to switch the device to the bar state, the optical power from the bar port is represented by the solid line in Fig 2.14. Based upon these two curves, a conclusion can be made: all waves can be switched simultaneously for a given driving power. The output of the TIR switch shows rapid oscillation from 400-630nm and 1600-1800nm. This is because of the high material absorption at these wavelengths which cannot be avoided through structure design, and the output light intensity is below the sensitivity of the optical spectrum analyzer. From 630-700nm, the optical loss is 5-10dB higher than that of 1550nm, but the uniformity between the cross state and the bar state is within 2dB. From 700-1600nm, the optical loss is within 5dB and the uniformity is within 2dB compared with those at 1550nm. As a conclusion, the working bandwidth of the TIR TO switch is 700-1600nm if we consider both the optical loss and channel uniformity; but it will extend to 630-1600nm if we only concern the uniformity.

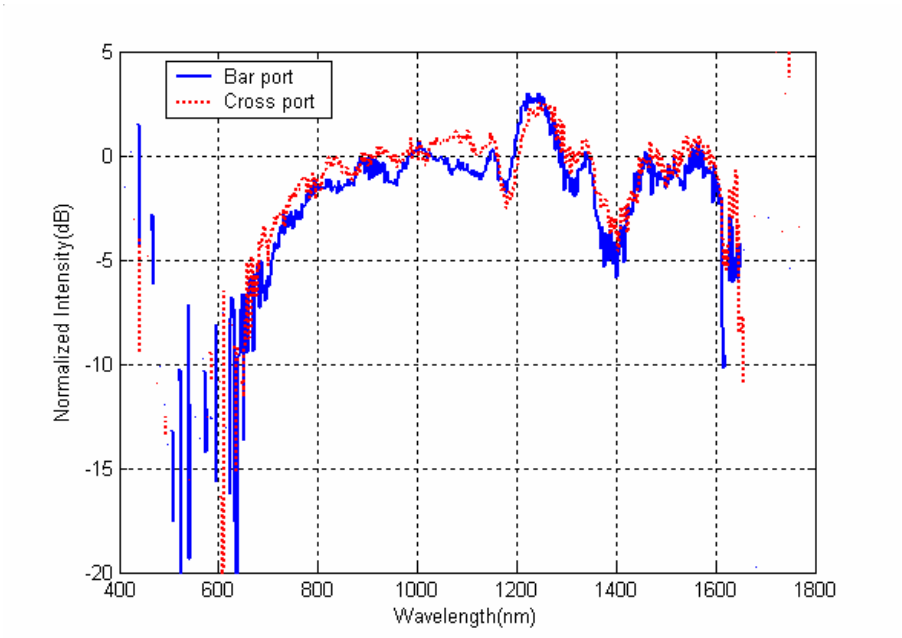

Fig 2.14 Optical response as a function of the wavelength

2.5 Cross Talk Minimization

2.5.1 Volume Relaxation phenomena of polymer materials

Polymer materials have a drawback because of the stability problem. When the operating temperature (T) is below the glass transition temperature (Tg), a limited amount of molecular motion prevents polymers from reaching equilibrium if there is a temperature shift. However, the entropy still drives polymers toward equilibrium, resulting in a gradually change of bulk volume after the temperature stabilization [13]. This so called volume relaxation phenomenon is an intrinsic characteristic of polymers. Since the bulk densities determine the refractive indices of polymers, the volume relaxation phenomenon causes the refractive indices a gradually change in the time domain [14]. Fig 2.15 shows the volume density change within a temperature cycle.

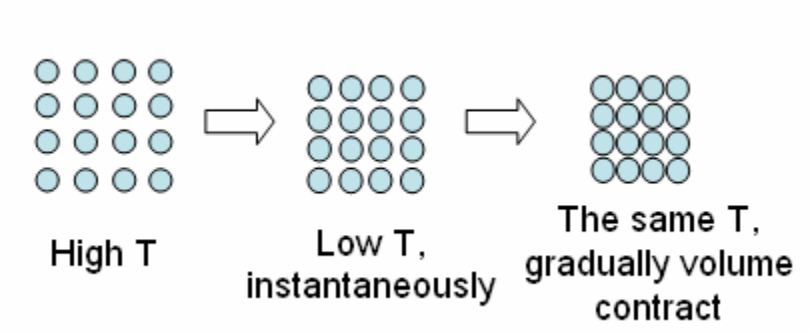

Fig 2.15 Volume density variation as the temperature change

As an approximation, the volume relaxation rate is inversely proportional to T_g－T [15], thus the refractive index will be more unstable at higher temperatures. TIR switches require a larger refractive index decrease ($\Delta n \sim 0.01$) in the central waveguide than other PLC structures. For instance, the top cladding beneath the electrode needs to be heated to 97℃ in the bar state with a 3° half branch angle[16]. At this temperature, the glassy polymers will face a serious volume relaxation problem even high Tg polymers are used. The result is that the refractive indices will not return to the initial values as the temperature does. The slightly smaller refractive index in the central waveguide partially reflects the incident light and deteriorates the cross talk of the device. Experimentally, we observed that the device may require up to 100 hours for the performance to stabilize.

2.5.2 Design compensation

In order to overcome this material problem, the half branch angle of the TIR switch is increased. This design is based on the fact that the interface of two dielectric media causes less reflection to light with a larger glancing angle, which equals the half branch angle in our design. Due to the amorphous nature of the polymer thin film, the waveguide switch is experimentally confirmed to be polarization independent within ±1%. In this letter, 2×2 switches with increased half branch angles are proposed and fabricated.

A 3-dimensional semi-vectorial beam propagation method (3-D SV BPM) is employed to investigate the characteristics of the TIR switch. The half branch angle θ is a paramount parameter determining the performance of the device. An increased θ will decrease the cross talk, however, the device will consume more power as well.

When the switch is heated, the refractive index of the polymer under the electrode heater is slightly smaller than the other area of the X-junction, thus forming an abrupt index interface with an index modulation of Δn. The index modulations by the volume relaxation phenomenon for the 3°, 4° and 5° half branch angle switches are approximately 5×10^{-4}, 6.5×10^{-4} and 8×10^{-4} measured by a Metricon prism coupler, which are marked by "volume relaxation affecting regions" in Fig 2.16. Fig 2.16 shows the cross talk as a function of Δn when the half branch angle (θ) is 3°, 4° and 5°. When Δn is within the "volume relaxation affecting regions", the slope decreases as θ increases. This indicates that with a larger half branch angle, the cross talk not only decreases, but also becomes less sensitive to the refractive index variation. Although a larger half branch angle requires a higher operating temperature, the device still successfully decreases the cross talk below -40dB in both the cross and bar states due to the insensitivity of the cross talk to the refractive index modulation.

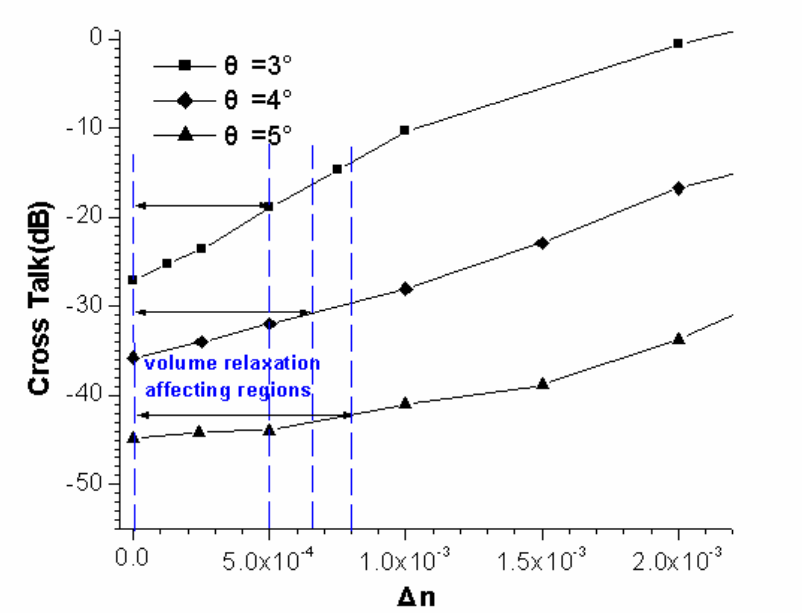

Fig 2.16 Cross talk as a function of the index modulation in the central waveguide for various half branch angles

2.5.3 Experimental Result

A Thorlabs ASE-FL 7001P broadband light source (1.53-1.61μm) is launched through an optical fiber of 8μm diameter core into one of the input waveguides of the fabricated device. Fig 2.17 shows the time dependent cross talk of the switches with 3°, 4° and 5° half branch angles in the cross state right after suspending the power supply. By increasing the half branch angle, the cross talk is significantly decreased and becomes more stable: the 20-hour variation is 10.1dB of 3°, 5.3dB of 4°, while only 2.7dB of 5°.

Fig 2.18 shows the optical power in the cross port and the bar port as a response to the electrical driving power. In the working state, the TIR switch with a 5° half branch angle shows a cross talk of -40.4dB in the cross state and -41.5dB in the bar state. The measured switching curve shows that if the applied driving power is less than 20mW, the power increase rate in the bar port is much lower than that with higher driving power, which is marked as an "Insensitive Region" in Fig 2.18. The experimental results also verify that the cross talk is not sensitive to small index variations. The switching power, which is defined as the point at which maximum optical power in the bar port is obtained,

is 66mW in Fig 2.18.

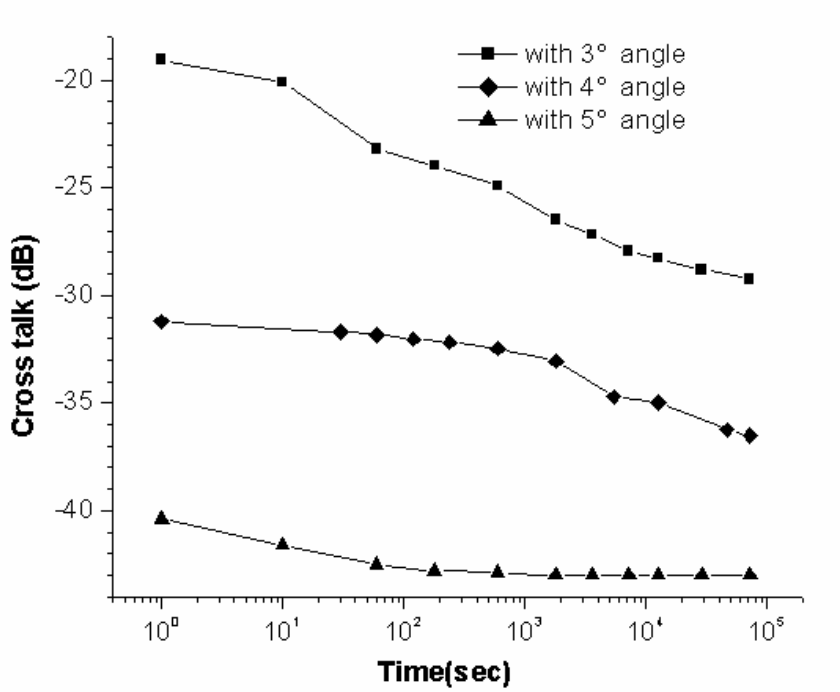

Fig 2.17 time dependent cross talk of devices with 3°, 4° and 5° half branch angle

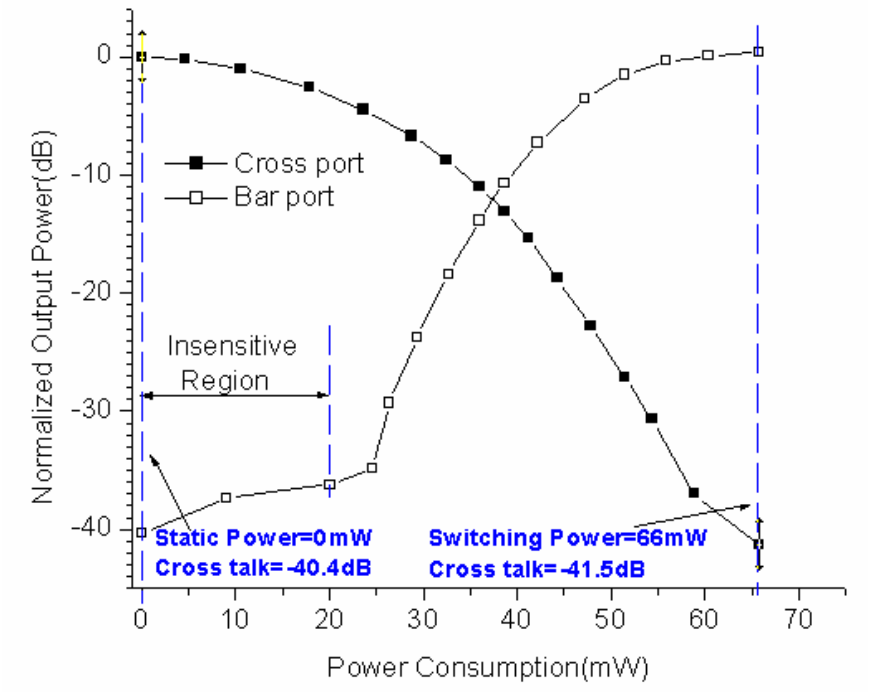

Fig 2.18 optical power in the output ports as a response to the electrical driving power

The input/output waveguides with 250μm separations are shortened to reduce the propagation loss. With a total device length of 19mm, the lowest fiber to fiber insertion loss obtained is 2.8dB and the polarization dependent loss (PDL) is 0.1dB.

2.6 4X4 TIR Optical Switch Matrix

TIR switches can be easily expanded to form a crossbar switch matrix that has great potential in optical cross connects (OXC) for the evolving optical communication networks. There have been several reports of very compact 4×4 crossbar optical switch matrices using the electro-optic TIR effect on LiNbO3[17] and InGaAsP/InP[18] substrates. But these types of switch matrices are suffering from polarization dependence and high insertion loss. Polymer or silica based switch matrices using the high and inherently isotropic thermo-optic effect can achieve low insertion loss, polarization insensitivity, and low cross talk. However, the reported N×N (N=16 is the input/output waveguide number) switch matrices are composed of either digital optical switches (DOS) or directional coupler Mach-Zehnder interferometer (DC MZI) switch units[19,20]. The cascaded 16×16 switches have lengths of 10.4cm and 66cm respectively, therefore the yield will be low and it becomes more difficult to integrate the switch matrices with other photonic devices. Additionally, each switch unit needs a constant heating power applied in both the cross and bar states, so the total power consumption will increase proportionally to N2, reaching 6.4W and 17W respectively according to [19] and [20]. High power consumption will cause many problems such as temperature drift, device lifetime deduction, and heavy system load. These drawbacks limit the scale of the switch matrix.

2.6.1 Design

A polymeric switch matrix using the thermo-optic TIR effect outperforms all other thermo-optic devices in size and power consumption requirement mentioned above. In this letter, we propose a compact 4×4 non-blocking thermo-optic switch matrix using the

TIR effect. The crossbar schematic diagram is shown in Fig 2.19, where switch unit uses the proposed structure reported.

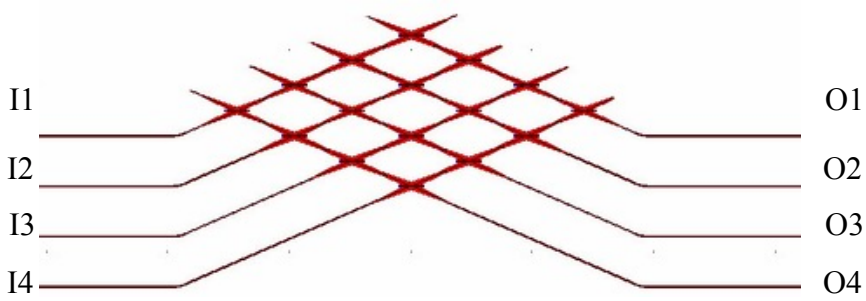

Fig 2.19 schematic diagram of the 4×4 crossbar switch matrix

For an arbitrary N×N switch matrix, the channel distance between each input waveguide is P, the half branch angle of each switch unit is θ, the curve waveguide radius is R, and the input/output waveguide length is L0. The total device length is derived as

$$L = \frac{W}{2\tan\theta} + 2L_0 + 2R[\sin\theta - (1-\cos\theta)\frac{1}{\tan\theta}] \qquad (2.7)$$

where W=2NP is the device width. The actual device width must be larger due to the presence of electrical pads and lead lines. Eqn.(2.7) predicts that crossbar optical switch matrices using the TIR effect can be much more compact than with MZI or DOS structures. Using the geometric parameters from [19], [20] and [17], the total lengths of N ×N optical switch matrices are plotted in Figv2.20. For N≥4, the total length of a TIR switch matrix is much shorter than those of MZI or DOS structures.

TIR switches consume no driving power in the cross state, which is a desirable feature for crossbar switch matrices because most of the switch units will work in the cross state. The total power consumption will be proportional to N, while other configurations need N2 activated switch units. Based on recent experimental result, each switch unit consumes 24mW of driving power. Therefore the total power consumption for the 4×4 switch matrix is up to 96mW.

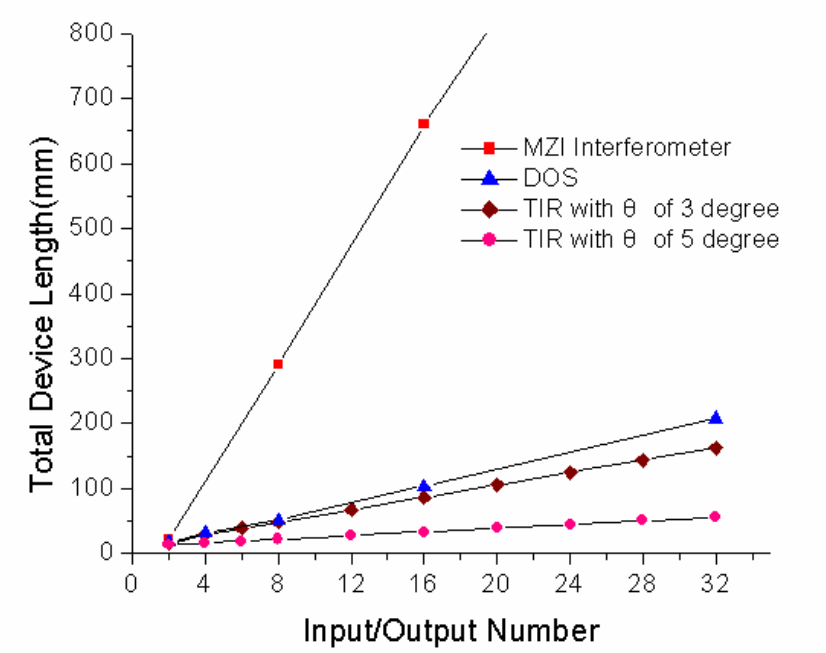

Fig 2.20 Total device lengths as a function of the input/output number

2.6.2. Experimental Results

A Thorlabs ASE-FL 7001P broadband light source (1.53-1.61μm) is launched through a single mode optical fiber with an 8μm diameter core into one of the input waveguides of the fabricated device. All 4×4 switching configuration is experimentally confirmed. When the input light is coupled into I2, and the switch units (I2, O1), (I2, O2), (I2, O3) and (I2, O4) shown in Fig.13 are activated sequentially to route the optical signal to different output waveguides. (I2, O1) here refers to the switch unit at the cross point of waveguide I2 and O1, and so on for the other switch units. Fig 2.21 shows the near field patterns of the output from O1 to O4 measured by a CCD camera.

A typical switching characteristics of the single switch unit has a cross state power consumption of 0mW and a bar state power consumption of 24mW. Table 2.2 shows the output powers at all working configuration. The values are recorded sequentially from O1 to O4 and the values with parenthesis are for the desired output waveguides. The input light intensity is measured to be 12dBm. From this table, we can

conclude that the fiber to fiber insertion loss of the switch matrix is from -8.7dB to -4.5dB, and the cross talk is below -23.3dB.

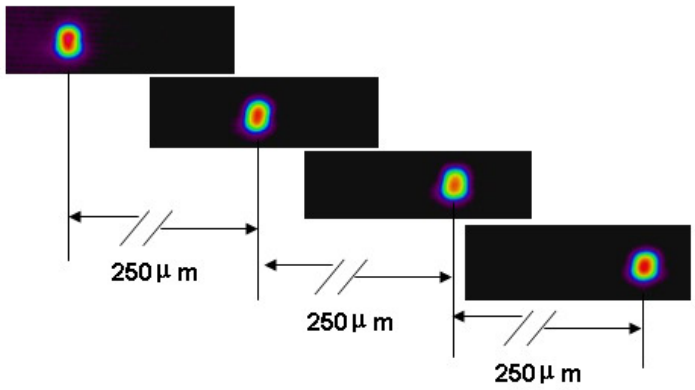

Fig 2.21 Near field patterns from the output waveguides

Table 2.2 output powers of the 4×4 switch matrix (unit dBm)

Output / Input	1	2	3	4
1	(3.31), -24.29 -21.99, -20.01	-24.55, (3.98) -21.62, -20.12	-23.86, -23.23 (4.65), -20.34	-25.92, -24.18 -22.33, (5.32)
2	(4.01), -22.78 -21.34, -19.37	-44.49, (4.59) -21.02, -19.32	-44.11, -42.55 (5.38), -19.03	-44.22, -42.45 -41.5, (6.01)
3	(4.51), -23.34 -22.12, -18.33	-43.1, (5.40) -22.34, -18.44	-45.61, -42.18 (6.12), -18.23	-49.06, -48.14 -45.91, (6.85)
4	(5.45), -20.22 -20.12, -20.88	-46.97, (6.18) -20.3, -20.81	-48.76, -47.8 (6.98), -20.55	-46.33, -43.46 -41.4, (7.50)

The switching speed of the polymeric thermo-optic switch is determined by the thermal conductivity and layer thickness of the polymer material. A higher thermal conductivity and smaller polymer thickness will lead to a faster speed. The optical response with respect to the electrical driving power is shown in Fig 2.22 when the light is launched into I1 and monitored from O1 with the activated switch unit of (I1, O1). C1

represents the electrical driving signal and C2 represents the responding optical signal. The 10% to 90% rising time and 90% to 10% falling time are measured to be 1.3ms and 2.1ms respectively.

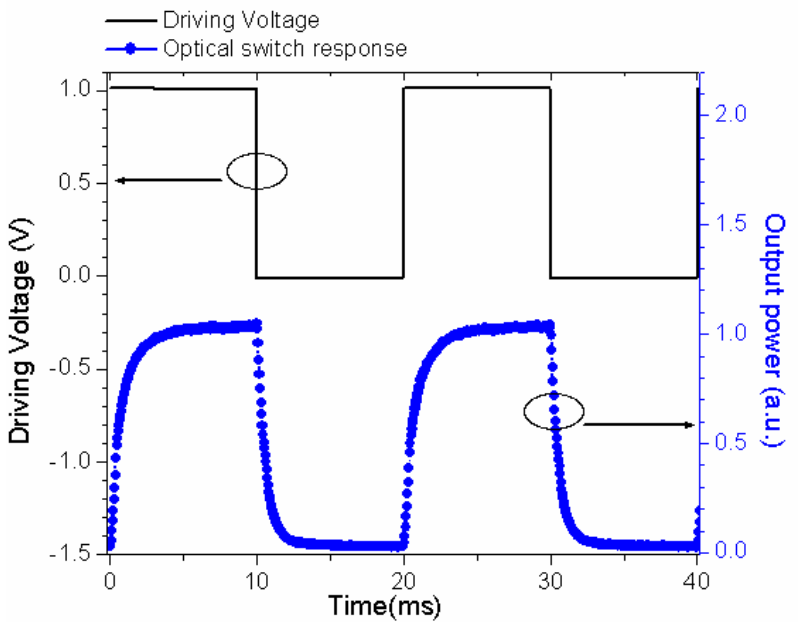

Fig 2.22 the driving electrical signal and the responding optical signal with a 2.1ms delay

2.7 References

[1] L.Eldada, "The promise of polymers", SPIE's OEmagazine, pp.26-29, May 2002

[2] C.S Tsai, B.Kim and F.R. Akkari, "Optical channel waveguide switch and coupler using total internal reflection", IEEE Journal of Quantum Electronics, Vol.14, pp. 513-517, 1978

[3] J.Yang, Q.Zhou and R.T.Chen, "Polyimide -waveguide-based optical switch using total-internal –reflection effect", Applied Physics Letters, Vol.81, pp. 2947-2949, 2002

[4] X Wang, B. Howley, M. Chen, et al, "Polymer Based Thermo-optic Switch for Optical True Time Delay", SPIE Photonics West 2005 San Jose

[5] Y.Silberberg, P.Perimutter and J.E.Baran, "Digital Optical Switch", Applied Physics Letters, Vol.51, pp.1230-1232, 1987

[6] Q. Lai, , W. Hunziker, H. Melchior, “Low-power compact 2×2 thermooptic silica-on-silicon waveguide switch with fast response”, IEEE Photonics Technology Letters, Vol.10, pp.681 – 683 ,1998

[7] H.Kogelnik and R.V.Schmidt, “Switched directional couplers with alternating Δβ”, IEEE J. Quantum Electronics, Vol.12, pp.396-401, 1976

[8] P.C Lee, E.Voges, “Three-dimensional semi-vectorial wide-angle beam propagation method”, Journal of Lightwave Technology, Vol.12, pp.215-225, 1994

[9] C. Lee, M. Wu, L. Sheu, P. Fan, J. Hsu, “Design and analysis of completely adiabatic tapered waveguides by conformal mapping”, Journal of Lightwave Technology, Vol.15, pp. 403 – 410, 1997

[10] A.S.Harry, “Thermal Analysis of electro- migration test structures”, IEEE Transactions on Electron Devices, Vol.34, pp.664-672, 1987

[11] I. Cayrefourcq, M. Schaller, C. Fourdin, et al, “Optical switch design for true time delay array antenna”, IEE Proceedings Optoelectronics, , Vol. 145 , pp.77 – 82, 1998

[12] C.C. Constantinou and R.C.Jones, “Path integral analysis of the linearly tapered graded-index waveguide”, J.Phy.D: Appl.Phys., Vol.24, pp.839-848, 1991

[13] S.Matsuoka, Relaxation Phenomena in Polymers. Hanser Gardner, NY: New York, 1992

[14] C.Robertson and G.Wilkes, “Refractive index: a probe for monitoring volume relaxation during physical aging of glassy polymers,” Polymer, vol.39, pp.2129-2133, Nov. 1998

[15] Z.Zhang, G.Xiao and C.Grover,”Volume relaxation in polymers and its effect on waveguide application,” Appl. Opt., vol.43, pp.2325-2331, Apr. 2004

[16] X Wang, B.Howley, M.Chen, et al, “Polymer Based Thermo-optic Switch for Optical True Time Delay,” in SPIE Photon. West’05, San Jose, CA, Jan., 2005, vol. 5728, pp.60-67

[17] L.McCaughan and G.Bogert, “4×4 Ti:LiNbO3 integrated-optical crossbar switch array,” Appl. Phys. Lett., vol.47, pp.348-350, Aug 1985

[18] H.Inoue, H.Nakamura, K.Morosawa, et al, “An 8mm length nonblocking 4×4 optical switch array,” IEEE J. Selected Areas in Commun., vol.6, pp.1262-1266, Aug 1988

[19] F.Rabbering, J.Numen and L.Eldada, “Polymeric 16×16 digital optical switch matrix,” in Proc. European Conference on Optical Communication 2001, Post-deadline, Amsterdam, Holland, Sep-Oct, 2001

[20] G.Takashi, Y.Missuho, H.Kuninori, et al, “Low-loss and high-extinction-ratio silica-based strictly nonblocking 16×16 thermo-optic matrix switch,” IEEE Photon. Technol. Lett., vol.10, pp.810-812, Jun 1998

Chapter 3 Integrated 4-bit True Time Delay Module using Cascaded Optical Switch Array

This chapter will describe the design and fabrication issues of the 4-bit true time delay module using cascaded optical switch array.

3.1 Design of the 4-bit True Time Delay Module

Optical true time delay (TTD) for phased array antennas (PAAs) offers many advantages over electrical phase delays such as wide bandwidth, immunity to electro-magnetic interference (EMI) and compact size [1]. Compared with wavelength tuning configuration [2], an optically switched waveguide delay line device structure [3] needs no tunable wavelength sources, resulting in reduced system costs and enhanced resistance to harsh environments. Another delay device structure composed of optical microelectromechanical system (MEMS) switches and fiber delay lines [4] shows desirable features such as low insertion loss. A novel design based on MEMS and free space white cell [5] also shows potential in terms of speed and scalability. However, either the fiber length has to be precisely cut or the mirrors have to be exactly assembled to achieve accurate delays.

A more attractive approach is to integrate waveguide switches and delay lines on a single chip by the planar lightwave circuit (PLC) technique. A previously reported 2-bit true time delay configuration using polymer optical switches and waveguide delay lines [5], which are defined by photolithography, can precisely deliver four true time delays. The fully integrated photonic circuit eliminates the discrete couplings between optical switches and fibers, therefore, it provides a more stable throughput and occupies less space. Additionally, the fabrication cost is significantly reduced. In this chapter, we present an implementation of a 4-bit polymer TTD device containing five fully integrated 2×2 thermo-optic switches based on the total internal reflection (TIR) effect.

The configuration of the proposed TTD device is shown in Fig 3.1(a). The device is composed of input/output waveguides, five 2×2 TIR thermo-optic switches, four reference lines and four delay lines, which give 16(2^4) delay combinations. Both optical switches and waveguide delay lines have a core index of 1.46 and a cladding index of 1.45. The 6.5μm×6.5μm channel waveguide cross section constrains the waveguide to the single mode condition and provides a measured coupling efficiency of 85% with a single mode fiber. The TIR switches have a 250μm waveguide separation and 4° half branch angle, as seen in Fig 3.1(b). For each crossing region, the waveguides are tapered from 6.5μm to 48μm to reduce the cross talk [6]. The switches are 4924μm in length including 500μm straight waveguide segments on each side to stabilize the optical mode into/out of the delay lines. Micro-heaters are placed on the top cladding layer and connected to bonding pads through lead lines. The bend radii of the reference lines are 1.5mm, and those of the delay lines are 1.75mm. The proposed 4-bit TTD device can dynamically deliver 16 delays from 0 to 177ps with 11.8ps increment, which are determined by the lengths of the waveguide delay lines.

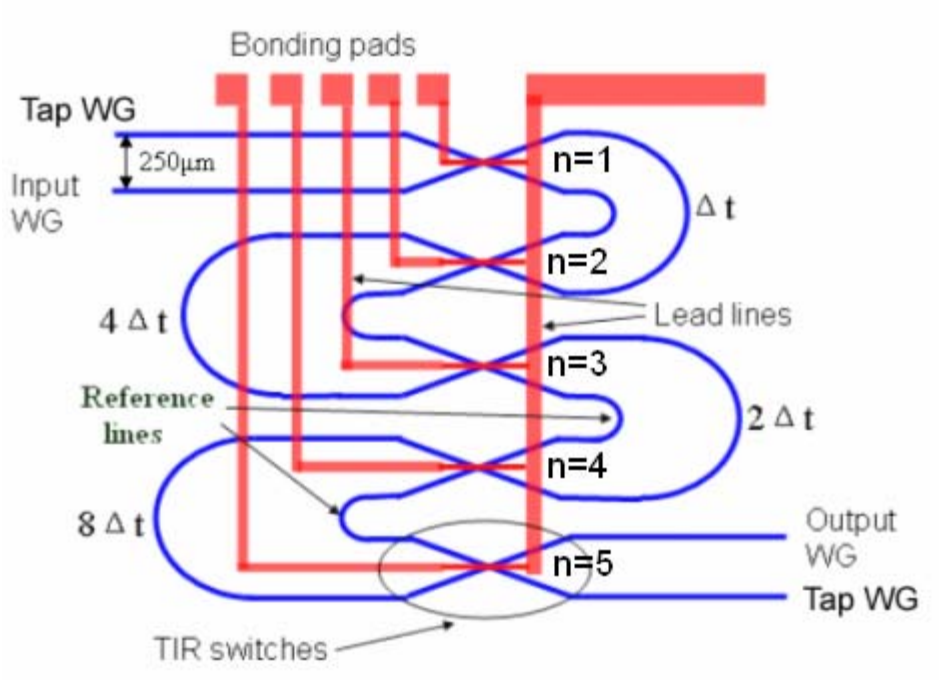

Fig 3.1 (a)

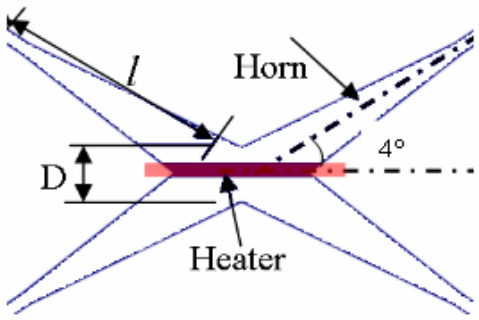

Fig 3.1 (b)

Fig 3.1 (a) Schematic of the 4-bit TTD device using TIR optical switches (b) Schematic of the TIR optical switches

3.2 Process Integration of the 4-bit TTD Device

UV curable fluorinated acrylates, ZPU12-460 and ZPU12-450 from ChemOptics, are used as the core and cladding materials. To integrate the optical switches and waveguide delay lines on a single chip, the process integrations were investigated, as depicted in the following steps, and illustrated in Fig 3.2 (a)-(d).

(1) The bottom cladding material ZPU12-450 and core material ZPU12-460 is spin coated and UV cured separately. Then a layer of SiO2 serving as the hard mask is deposited in 200ºC. The patterns of the optical switches and delay lines on the first mask are defined by contacting photolithography, and transferred to the SiO2 layer by reactive ion etching (RIE). The patterned SiO2 hard mask can protect the polymer material underneath with a very high selecting ratio and produce high quality waveguide in the followed RIE process. Fig 3.2(a) shows the formation of the waveguide structure by the aforementioned steps.

(2) After forming the core layer, the top cladding polymer, ZPU12-450 is spin coated again and UV cured. Another SiO2 layer is grown by low temperature PECVD, which will function as an isolation layer to protect the polymer in the next lift-off process. The negative pattern of the optical switch electrodes, lead lines and bonding pads from the second mask are formed by the image reversal photolithography technique. Then 5nm chromine/200nm gold layer are deposited and followed by the

lift-off process, which will ensure the uniformity of all the electrode heaters. The device status after the lift-off process is shown in Fig 3.2(b).

(3) The third mask contains the pattern of the lead lines, bonding pads and trenches for the curving waveguides, which is necessary to reduce the bending loss. The pattern is transferred to the spin coated photoresist, which is post baked to obtain better stability. The samples are electroplated to increase the lead line and bonding pad thickness to 2μm. Since the electrode heater is protected by the photoresist, its thickness will remain 205nm and maintain a much higher resistance than the lead lines and bonding pads. The electroplating process is also indispensable to the wire bonding step. Fig 3.2 (c) shows the device status.

(4) An RIE process is adopted to open the SiO2 window for the air trenches, and to etch the polymer air trench in the followed step. The final device is illustrated in Fig 3.2(d). After that, the sample is diced with a diamond saw for the back-end process.

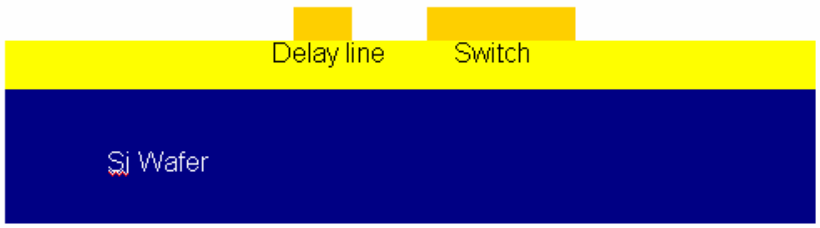

Fig 3.2(a)

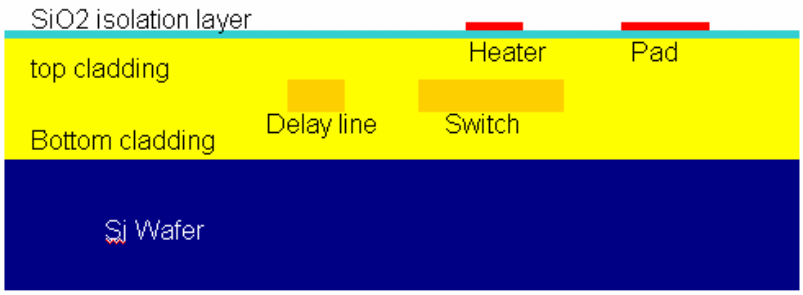

Fig 3.2(b)

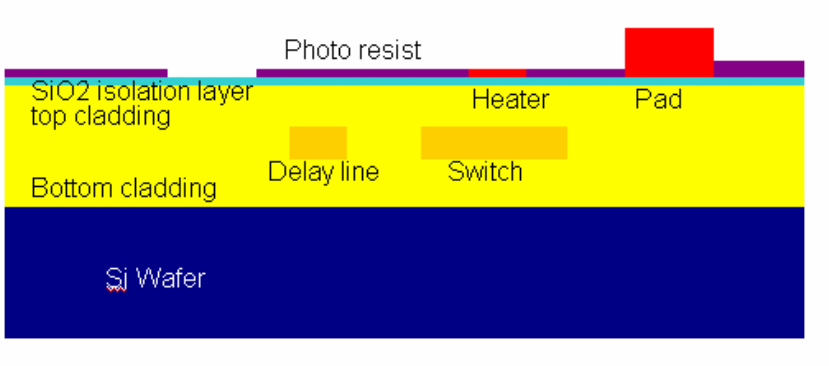

Fig 3.2 (c)

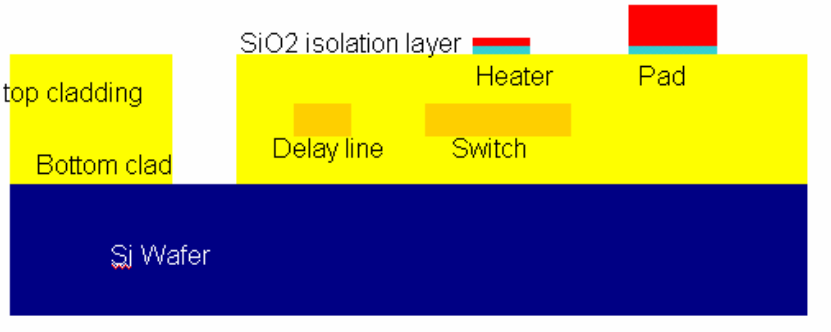

Fig 3.2 (d)

Fig 4.2 Process Integration of the 4-bit TTD module

Fig 3.3 shows the fabricated 4-bit TTD device with an enlarged view of the TIR thermo-optic switch. The chip die dimension is 21.7mm×13.7mm.

3.3 Experimental Characterization of the 4-bit TTD Module

To route the optical signal to a single output waveguide, 0, 2 or 4 switches are required to be activated. The working states of the five switches, as well as the total power consumption, in the 16 delay configurations are shown Table 3.1. The maximum power consumption is 143mW when four switches are fully activated. The average operating power of a single TIR switch is only 1/10 of that required for a digital optical switch. The switching speed of the TIR switches is measured by applying a 50Hz square wave signal with a 50% duty cycle. Both the on and off state switching time are measured to be less than 3ms, as shown in Fig.3.4.

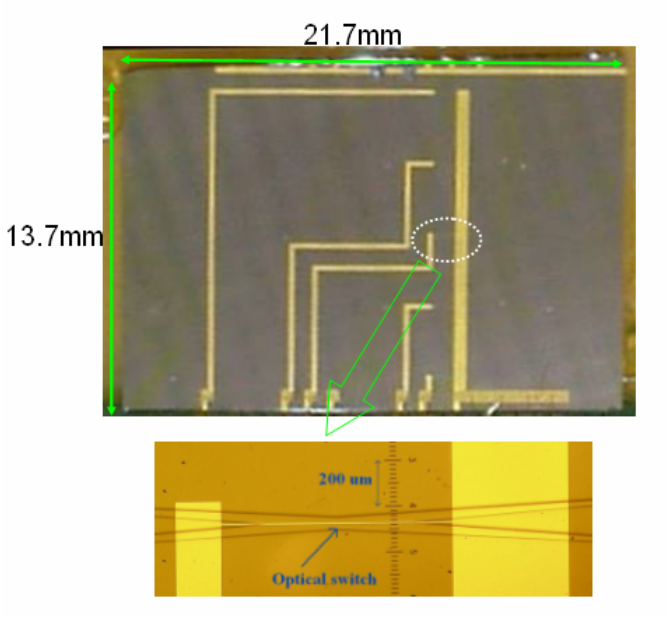

Fig 3.3 Chip die of the 4-bit TTD device with an enlarged view of the optical switch

Table 3.1 Delay configuration, power consumption and RF performance

Time Delay (Δt)	Switches Activated	Driving Power (mW)	Calculated phase error@10.5GHz (°)	Measured phase standard deviation(°)	Delay error (ps)
0	1,5	67	**-0.04**	0.94	-0.022
1	2,5	66	**-0.14**	0.39	0.221
2	1,3,4,5	137	**0.08**	0.43	0.504
3	2,3,4,5	137	**0.12**	0.35	0.236
4	1,2,3,5	141	**0.02**	0.67	0.227
5	3,5	66	**0.14**	0.61	0.086
6	1,2,4,5	141	**0.08**	0.75	-0.745
7	4,5	65	**0.08**	0.76	-0.383
8	1,4	68	**-0.04**	0.57	0.379
9	2,4	67	**-0.14**	0.64	-0.351
10	1,3	68	**-0.15**	0.68	-0.197
11	2,3	68	**-0.08**	0.57	-0.415
12	1,2,3,4	143	**-0.02**	0.48	-0.418
13	3,4	67	**0.14**	0.55	0.175
14	1,2	70	**0.16**	1.14	-0.446
15	none	0	**0.19**	1.08	-0.008

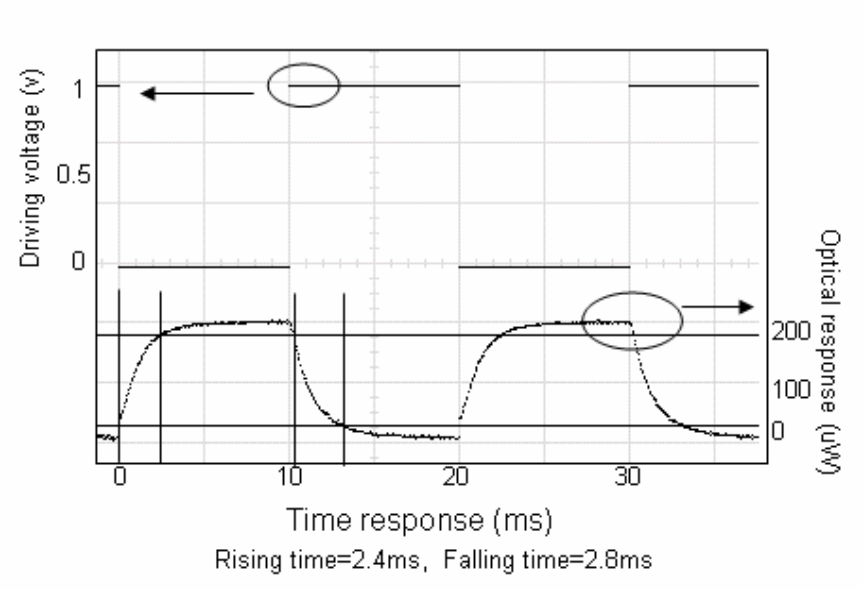

Fig 3.4 Switching speed measurement of the 4-bit TTD device

The wavelength response of the 4-bit TTD device is shown in Fig 3.5. The output power maintains at a stable level from 1500 to 1600nm wavelength range.

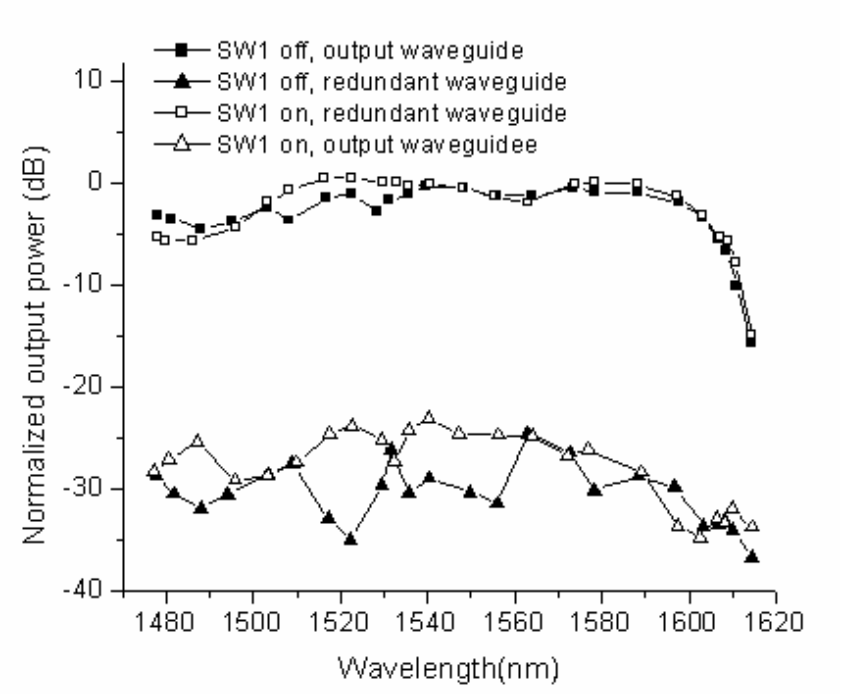

Fig 3.5 Wavelength response of the 4-bit TTD device

The insertion loss at different delay status of the 4-bit TTD device is measured and shown in Fig 3.6. It clearly shows that the insertion loss will increase as the waveguide delay path length increase. The length dependent loss is 0.18dB/Δt, in another word, 0.73dB/cm. It is higher than the measured 0.38dB/cm waveguide propagation loss, possibly due to the waveguide bending loss and process induced waveguide loss. For example, the second PECVD process under 200ºC can cause some material degradation. It is also interesting to point out that the switch dependent loss is also remarkable. The optical switch has 0.58dB lower insertion loss when activated, according to Fig 3.6.

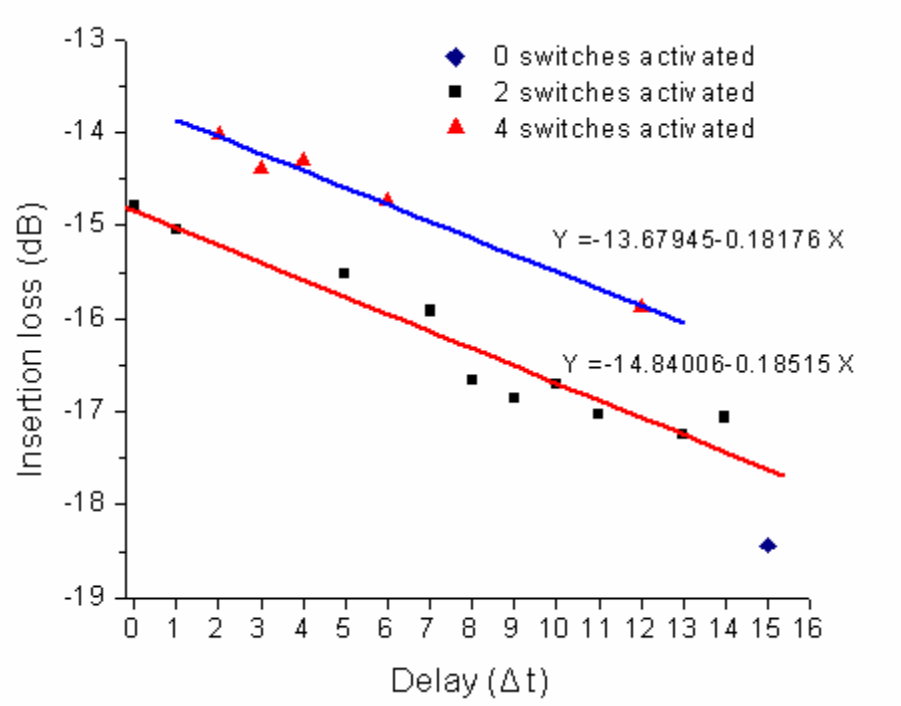

Fig 3.6 Measured insertion loss of the 4-bit TTD device under the 16 different statuses

The time delay can be measured by pulse laser combined with a high speed photodetector, and a digital oscilloscope. The time delay of the optical pulse can be directly read from the oscilloscope. Fig 3.7 shows the 16 measured pulse delay, ranging from 0 to 177ps. However, the accuracy is often limited by the response time of the photodetector. The pulse broaden width is usually comparable with the time delay.

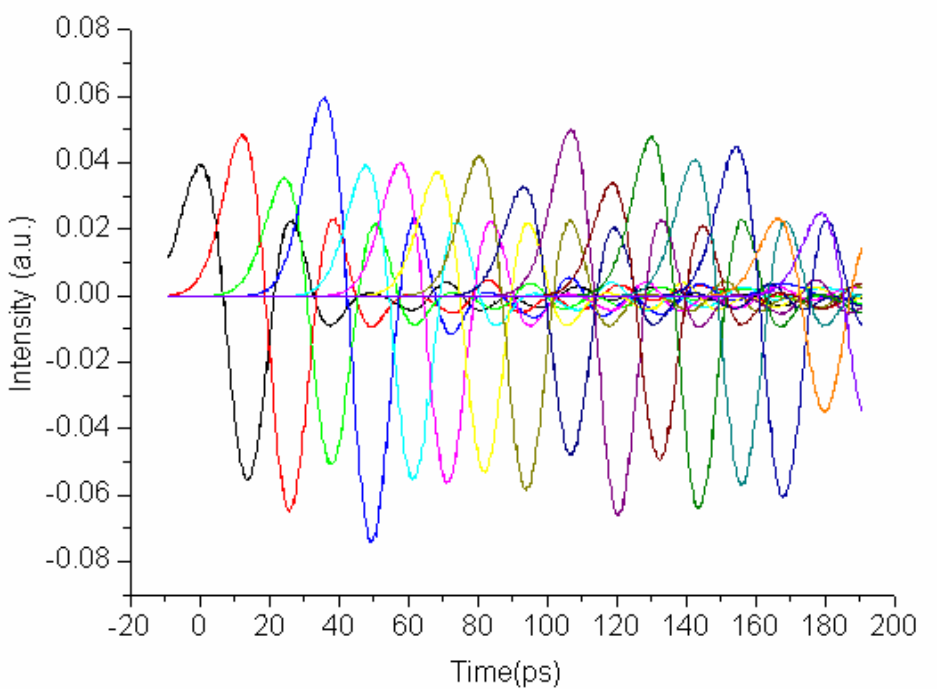

Fig 3.7 Optical pulse delay in the 16 configurations

Another widely used measurement method is described here. A HP8510C network analyzer, which provided a continuously scanning microwave from 6 to 12GHz, drove a 40GHz $LiNbO_3$ modulator to transfer the RF signal into the photonic carrier wave from a constant laser diode. The light was coupled into and out of the 4-bit TTD device through single mode fibers, and finally fed into a high speed detector. The RF signal from the photo detector was amplified and fed into the network analyzer. With the RF frequency scanning, the relative phase would change at a fixed rate, which was determined by the time delay of the device. Fig 3.8 shows the measured RF signal phase change with the scanning frequency, giving the true time delay range from 0 to 177.8ps.

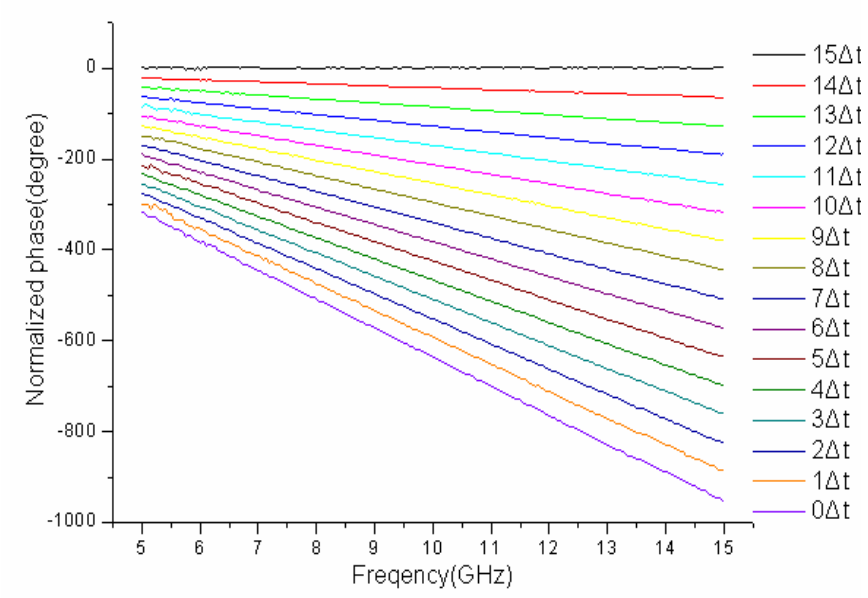

Fig 3.8 True time delay measurement with the frequency scanning of the RF signal

3.4 RF Phase Error with Optical Switch Cross Talk

The RF performance, namely, the RF phase error caused by the optical switch cross talk, is analyzed in this part. Two typical structures are presented to be compared with each other. Fig 3.9 (a) uses a 2×1 combiner as the output waveguide, which is described in ref.[7-8]; while Fig 3.9(b) uses a 2×2 switch, corresponding to the structure in this paper. The analysis procedure, from Eqn.(3.1) to Eqn.(3.6), follows the work done in ref.[7].

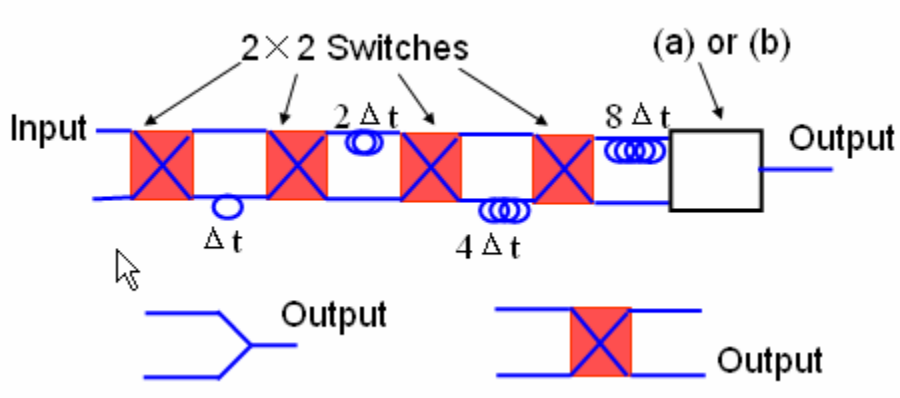

(a) (b)

Fig 3.9 4-bit TTD device, the last stage using (a) 2×1 combiner (b)2×2 optical switch

We assume the cross talk values as CT for all the five switches both in the cross and bar states, and neglect the propagation loss of delay lines for simplicity. For each switch, the splitting ratio of the optical E-field is

$$a:b=\sqrt{10^{-\frac{CT}{10}}}:1 \tag{3.1}$$

The minor signals from each switch will travel through undesired paths. Some of these signals will be transferred to the redundant waveguide, which is not harmful to the output signal quality. However, some of these signals will be routed to the output waveguide, which will cause an RF signal phase error. For analysis, we assume all the 16 possible delays will be routed to the output waveguide, so the optical E-field at the detector is

$$E=E_0e^{j\omega t}(C_1e^{j\phi_1}+C_2e^{j\phi_2}+...+C_{16}e^{j\phi_{16}}) \tag{3.2}$$

E0 is the normalized field amplitude, ω is the optical angular velocity, Ci is the coefficient of the i-th delay, and Φi is the RF phase delay. Neglecting the optical angular frequency, which is much higher than the RF signals, the intensity of the optical signal that will be detected is

$$I=E_0(C_1e^{j\phi_1}+C_2e^{j\phi_2}+...+C_{16}e^{j\phi_{16}})E_0(C_1e^{j\phi_1}+C_2e^{j\phi_2}+...+C_{16}e^{j\phi_{16}})^* \tag{3.3}$$

By expanding Eqn.(3) into the sum of polynomials, each i-th detected RF envelope signal has the coefficient of

$$X_i=\sum_{j=1}^{16}C_iC_j\cos(\phi_i-\phi_j) \tag{3.4}$$

For example, X1 is the desired signal, while the undesired signals, X2, X3, ⋯,X16 will function as noise. Combining all the RF signals as Fig 3.10 shows, the measured RF signal X1′ has a phase error with respect to X1

$$\phi_{error,i} = \tan^{-1} \frac{\sum_{j=1, j\neq i}^{16} X_j \sin(\phi_j - \phi_i)}{X_i + \sum_{j=1, j\neq i}^{16} X_j \cos(\phi_j - \phi_i)} \tag{3.5}$$

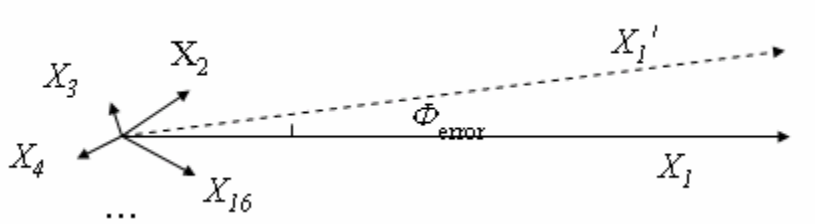

Fig 3.10 Illustration of RF signal phase error in the 4-bit TTD device

In Fig 3.9(a), the first order minor signals(E-field splitting ratios are a:b), which go through one switch's undesired port, will leak through the redundant output waveguide. Only second order minor signals (E-field splitting ratios are a2:b2), which go through two switches' undesired ports, have the opportunity to be detected, and totally there are $C_5^2 = 10$ possible signals. Based on Eqn.(3.1) which provides the E-field splitting ratios between the major and minor ports, the phase error caused by the second order minor signals is

$$\phi_{error,i} = \tan^{-1} \frac{b^2 \sum_{j=1}^{10} \sin(\phi_j - \phi_i)}{a^2 + b^2 \sum_{j=1}^{10} X_j \cos(\phi_j - \phi_i)}, \tag{6}$$

In the 2×1 combiner structure shown is Fig 3.9(b), all first order minor signals, which are the main noise contributors, plus higher order minor signals, will be captured. The phase error can vary with different delay configurations, depending on the working states of the optical switches. Fig 3.11 shows the simulated results of the RF phase error due to the cross talk for the delay value of 15Δt when the RF is 10.5GHz. The 2×2 switch TTD device structure has a smaller phase error than that of the 2×1 combiner one. But even with the 2×2 switch structure, -20dB cross talk still causes 2° phase error. In order

to overcome the volume relaxation induced cross talk aggravation of polymer TIR switches, a large half branch angle of 4° is chosen since it can offer a dynamic cross talk below -30dB [9]. All possible RF phase error due to the cross talk is simulated and shown in Table3.1.

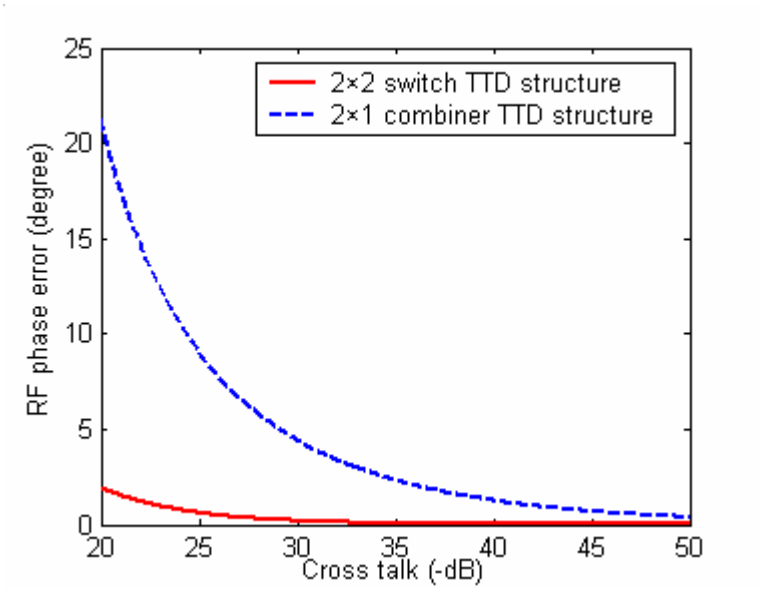

Fig 3.11 Simulated RF phase error caused by the optical switch cross talk

To experimentally evaluate the impact of the optical switch cross talk upon the RF signal phase error, we measured the phase error from 6~12GHz when the delay is 15Δt shown in Fig 3.12. As we can see from Fig 3.8, each scanning line was not a perfect straight line, with some deviation caused by environmental noise or system cross talk. If we subtract the linear fitted base line value from each measured phase change, phase error can be obtained, which represents the RF signal quality. The measured data values oscillate rapidly within 4° due to environmental noise. The linear fitted curve has a standard deviation (SD) of 1.08° and a slope of 0.00285°/GHz, corresponding to -7.9fs measurement error. Simulated phase error curves with different cross talk values, however, show gradual baseline variation, which is different from the measured result. The SD of the measured phase and delay error in all the 16 working states are also

presented in Table.1. A conclusion can be drawn that the RF phase error caused by optical switch cross talk is negligible for the device, compared with environmental noises.

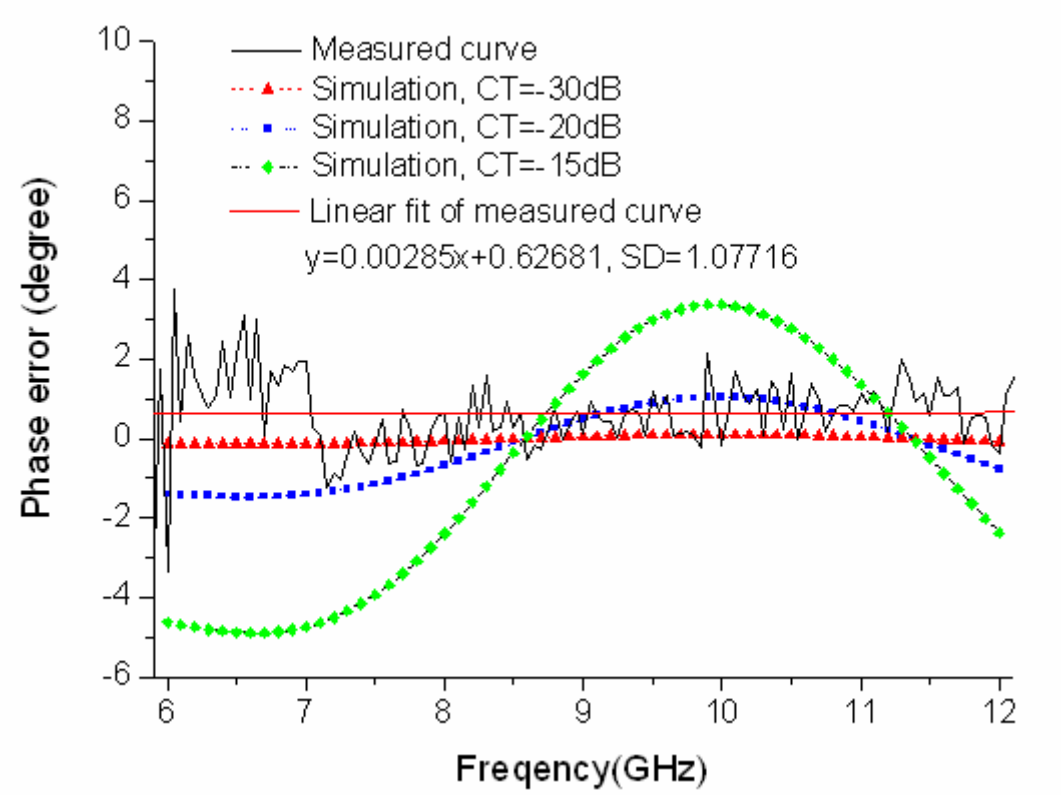

Fig 3.12 Simulation and experimental results of RF phase error

3.5 Summary

The fabricated 4-bit polymer TTD device using fully integrated TIR switches exhibits accurate delays, low power consumption, small chip size and low fabrication costs. The switching time of the TIR switches is below 3ms. Simulations predict that the cross talk induced RF signal phase error is negligible. This result is confirmed by the experimental data.

3.6 References

[1] W.Ng, A.Walston, L. Tangonan, J. J. Lee, I. Newberg, and N. Bernstein, “The first demonstration of an optically steered microwave phased array antenna using true-time-delay,” *J. Lightwave. Technol.*, vol. 9, no. 9, pp.1124–1131, Sep. 1991

[2] Z. Shi, Y. Jiang, B. Howley, Y.Chen, F. Zhao, and R.T. Chen, “Continuously Delay-Time Tunable-Waveguide Hologram Module for X-Band Phased-Array Antenna”, IEEE Photon. Technol. Lett., vol.15, pp.972-974, July, 2003

[3] K.Horikawa, I.Ogawa, H.Ogawa, and T.Kitoh, “Photonic switched true time delay beam forming network integrated on silica waveguide circuits,,” in IEEE MTT-S Int., vol. 1, May 16–20, 1995, pp. 65–68.

[4] J.D.Shin, B.S.Lee, and B.G.Kim, “Optical true time-delay feeder for X-band phased array antennas composed of 2×2 optical MEMS switches and fiber delay lines”, IEEE Photon. Technol. Lett., vol.16, pp.1364-1365, May, 2004

[5] B.Howley, Y.Chen, X.Wang, and Ray T.Chen, “2-bit Reconfigurable true time delay lines using 2×2 polymer waveguide switches,” IEEE Photon. Technol. Lett., vol.17, pp.1944-1946, Sep. 2005

[6] Y.O. Noh, J.M. Kim, M.S. Yang, H.J. Choi, H.J. Lee, Y.H. Won, S.G. Han, “Thermo-optic 2 × 2 asymmetric digital optical switches with zero-voltage operation state,” IEEE Photon. Technol. Lett., vol.16, pp.446-448, Feb. 2004

[7] X.Wang, B.Howley, M.Y.Chen and R.T. Chen, “Polarization-independent All-wave Polymer Based TIR Thermo-optic Switch”, IEEE J. of Lightwave Technol.,vol.24, pp.1558-1565, Mar.2006

[8] A.A. Szep, “Polymer-based integrated optical waveguide true time delay for wide-band phased array antennas,” Ph.D. dissertation, pp.17, pp.22-36, Univ. of Southern California, 2002.

[9] G.L Tan, R. E. Mihailovich, J. B. Hacker, J. F. DeNatale, and G.M. Rebeiz, “Low-Loss 2- and 4-bit TTD MEMS Phase Shifters Based on SP4T Switches”, IEEE Trans. on Microwave Theory and Techniques, vol.51, pp.297-304, Jan. 2003

[10] X.Wang, B.Howley, M.Y.Chen and R.T.Chen, “Crosstalk minimized polymeric 2 ×2 optical switch”, IEEE Photon. Technol. Lett., vol.11, pp.16-18, Jan., 2006

Chap 4 Hard-molding Fabrication of Large Cross Section Multimode Waveguide Array

The research of optical interconnects can be traced back to 1984, when Joseph W. Goodman first proposed the concept of "optical interconnections for VLSI systems". Many works have been done to demonstrate the feasibility and advantage of optical interconnects over the electrical copper lines. However, it is still far from commercialization to deploy optical interconnects inside computer boards, mainly due to two concerns, the reliable and low cost optical components, and the burden of electrical-to-optical and optical-to-electrical conversion. The second issue will be addressed in the next chapter. The active optical components, VCSELs and PIN photodiodes can be mass produced at a very low cost. Large cross section waveguide array remains to be the major cost of the optical components.

4.1 Overview of Large Cross Section Waveguide Fabrication Techniques

Various techniques have been employed to produce the large cross section waveguide for board level optical interconnects. We will give a brief summary.

Yoshimura presented a RIE fabrication method [1] for the multimode waveguide array with 42μmX42μm cross section. The polymer is etched with oxygen.

The main drawback of the RIE method is the long etching time required to form the deep waveguide. More attractive approaches using photo-image polymers can cross link the liquid polymer and form the desired large cross section waveguide. Borreman [2] successfully demonstrated the feasibility of this photo bleaching process on a negative photoresist, Su-8, and achieved a smooth side wall and low scattering loss.

Another approach to forming optical polymer waveguides is based on laser writing. This technique [3] has the advantage of allowing rapid prototyping, as opposed to mask-based approaches in which case a mask must be designed and produced before waveguides can be fabricated. Laser writing also affords considerable latitude in power level, focusing, and writing speed, permitting the creation of novel structures that are virtually impossible to make by mask-based lithography.

A distinct advantage of polymers in a manufacturing environment is their unique ability to be processed by fast turnaround techniques that are not available for more conventional photonic materials such as glass and semiconductors. These techniques include casting, molding, hot embossing, and soft embossing [4]–[7]. Among the four, casting and soft embossing are the processes of choice for photochemically reactive materials, and both have been demonstrated with the acrylate materials described above. In both cases, either a UV-transparent substrate or a UV-transparent tool is required for processing. The tool comprises an inverted replica of the structure to be created (e.g., a channel on the tool will become a rib on the substrate, and vice versa). In the case of soft embossing, the tool in the form of either a roll or a platen is impressed into the liquid monomer, the monomer is cured with UV light, and the tool is removed. Waveguides are formed by subsequently either filling channels or over cladding ribs formed in the embossing process.

4.2 51cm Long Waveguide Array Fabricated by Hot Embossing

In this subchapter, hard molding method based on hot embossing is employed to form a long waveguide. Our group previously demonstrated a soft-molded waveguide layer with 45º coupling mirrors that is suitable for the embedded structure [8]. Yoon et.al.[9] and Mizuno et.al.[10] also fabricated straight waveguide array by hot embossing with low propagation loss. However, the length of these reported waveguides is less than 6cm, which cannot show obvious advantage over copper

tracks. To stay competitive and deliver the products favorable requires tens of centimeters waveguide length. Over 1-meter-long waveguide based on photo-bleaching polymer has been demonstrated [11], but not by molding or embossing, which can afford a lower cost. Molding a long waveguide needs to overcome the technical issues such as uniformity, defects and handling.

Silicon mold is chosen in our experiment because: first, silicon can be etched by RIE at a relative low cost; second, surface roughness of silicon side wall can be reduced to sub-nanometer level; third, silicon has a very low thermal expansion coefficient, offering a precise transferred size. The disadvantage of silicon is its fragility, which will make the hard mold easily broken. Thus, the pressure and temperature of the molding process has to be controlled.

The waveguide pattern is composed of twelve 50μm-wide parallel waveguides with 250μm pitch. With the contacting photolithography, the pattern is transferred to a 1mm thick silicon wafer with 0.5μm top SiO2 layer. It is then etched down by reactive ion etching (RIE) to the silicon layer, leaving the protected SiO2 has a hard mask. To produce the desired 50μm depth pattern, Deep RIE (DRIE) is employed to etch the silicon with acceptable processing time. Due to the relative high etch rate and alternating etching-passivation step, the resulted silicon side wall is pretty rough. Fig.4.1 shows the SEM image of the silicon surface by DRIE.

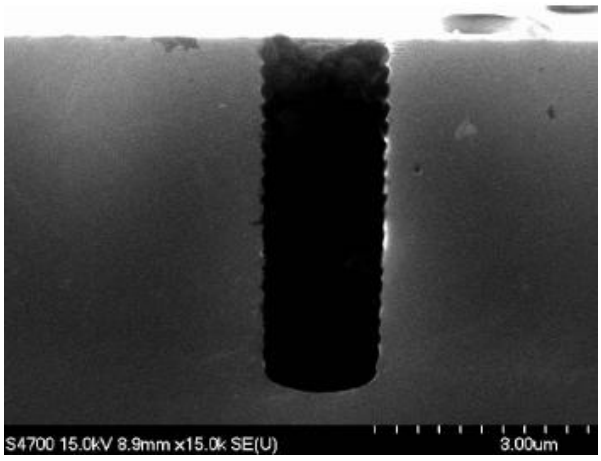

Fig.4.1 SEM of the silicon surface etched by DRIE

We successfully demonstrated a 51cm-long waveguide array by silicon hard-molding method. Compared with the flexible molds---usually made of elastomeric polydimethylsiloxane (PDMS) for pattern transfer, silicon hard molds stand out in durability and size precision.

The 51cm-long waveguide array curves inside a 4" mask. The pattern is composed of an array of twelve 50μm-wide parallel waveguides with 250μm pitch. With the contact photolithography, the pattern is transferred to a 1mm thick silicon wafer with a 0.5μm top SiO2 layer. It is then etched down by reactive ion etching (RIE) to the silicon layer to obtain the protected SiO2 has a hard mask. Due to the relatively high etch rate and the alternating etching-passivation step, the resulted silicon side wall is pretty rough. The roughness will be transferred to the polymethylmethacrylate (PMMA, Cyro Company) substrate, causing a significant scattering loss. To smooth the surface, the silicon wafer is wet-oxidated at 1050ºC for 4 hours and then etched by buffered oxidation etchant (BOE) to strip away the SiO2 [12]. With this approach, the surface root mean square (RMS) is reduced from 6.9nm to 1.2nm. Fig 4.2 (a) and (b) show the atomic force microscopy (AFM) images of the side wall profile after DRIE and oxidation-smoothing process.

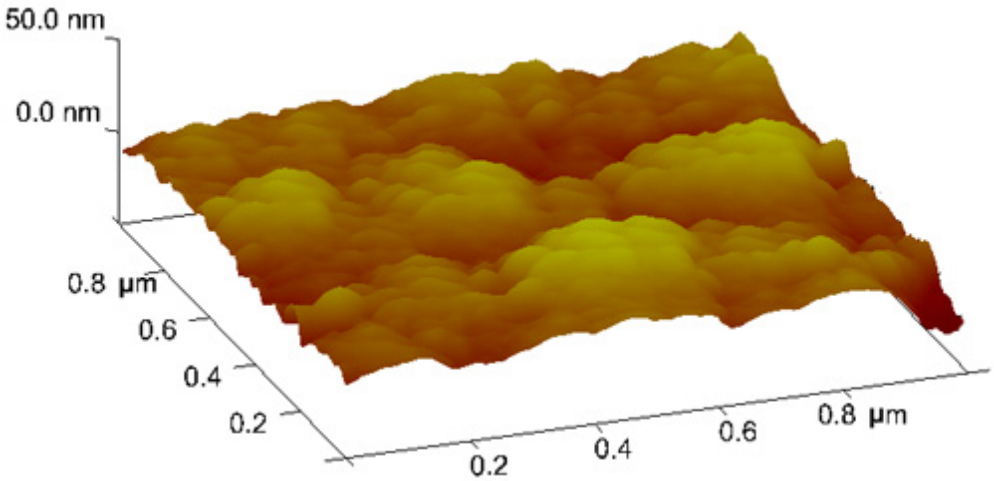

Fig 4.2 (a) The AFM images of the silicon side wall after DRIE

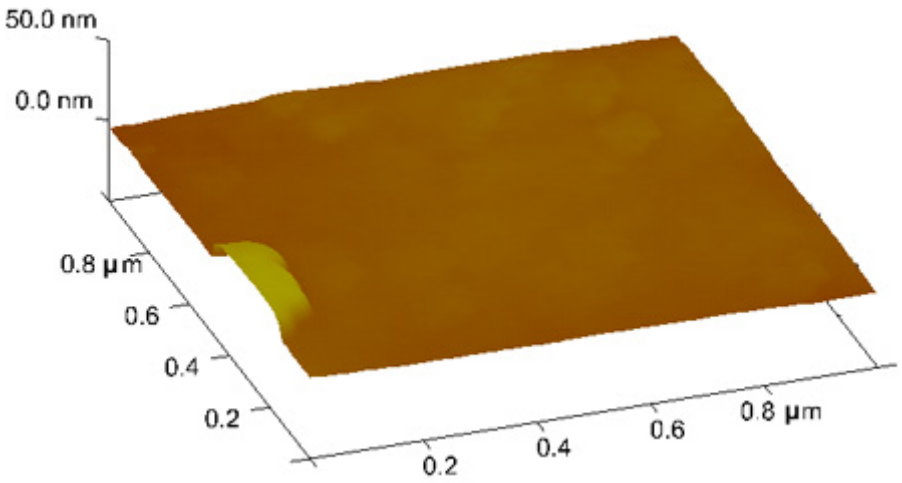

Fig 4.2(b)

Fig 4.2 (b) The AFM images of the silicon side wall after the oxidation-smoothing process

The 200µm thick PMMA film was used as the waveguide substrate, with a refractive index of 1.489 at 850nm. The hot embossing process was carried out on a specially designed molding machine with controllable pressure and temperature. This machine is capable of handling sample size as large as 36cmX24cm. Limited by the silicon mold size, we can only work on 4" wafers at this moment. The PMMA film was heated to 150ºC, 40ºC above the glass transition temperature. A pressure of 0.5MPa was applied to the silicon master mold and PMMA film with a holding time of 3min. To deliver the pressure homogeneously across the sample, a PDMS buffer layer was inserted between the PMMA film and the embossing template. By the water cooling system, the template temperature ramped down at a rate of 10ºC/min to room temperature, and then de-embossed the PMMA film with the master mold. This process would release the internal stress and ensure the pitch distance exactly at 250µm. After preparing the multimode waveguide patterns on a PMMA sheet by hot embossing, they were filled with a UV curable fluorinated polymer (WIR30-500 from ChemOptics, with a refractive index of 1.50 at 850nm) as the core material. The excess material was scraped off. After UV curing in the nitrogen atmosphere, the PMMA sheet was coated with another layer of top cladding material, WIR30-470

with a refractive index of 1.47 at 850nm. The sample was UV cured and finally cleaved and polished for testing. Fig 4.3 shows the 51cm-long waveguide array on the PMMA sheet, with the microscopy image of the cross section.

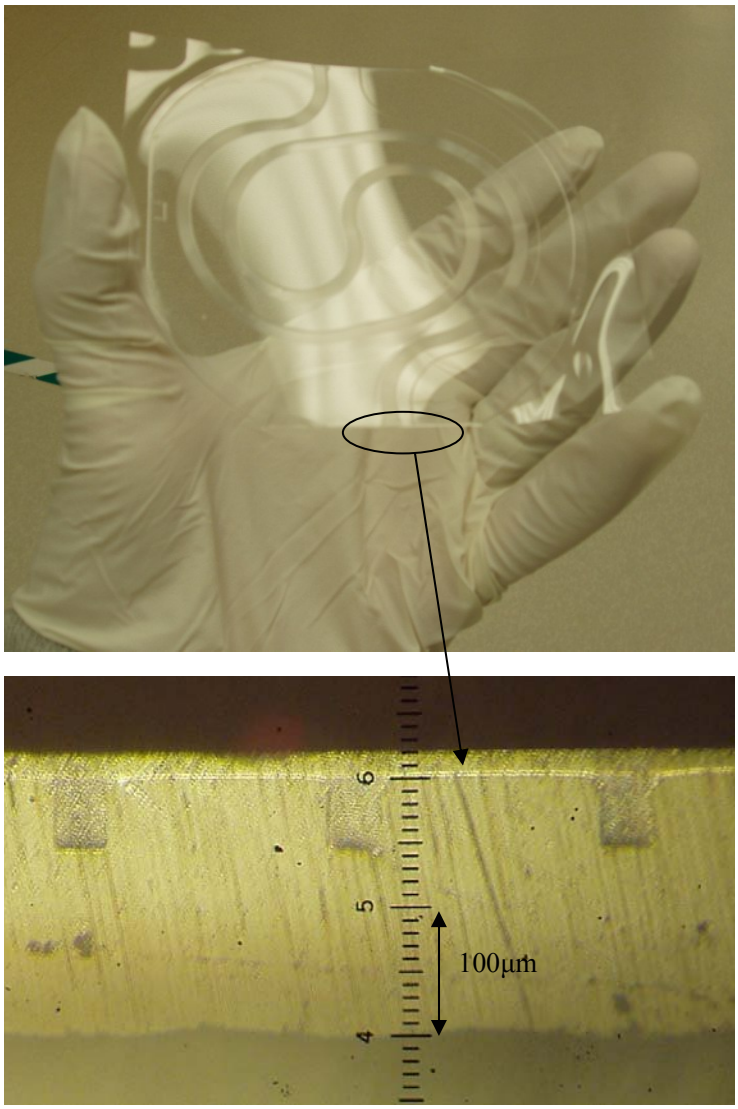

Fig 4.3 51cm-long waveguide array on PMMA sheet with microscopy image of the cross section

To measure the light transmission over the waveguide, a 9μm single mode fiber coupled with a VCSEL diode was aligned with the input surface. The near field pattern at the output surface was observed through a CCD camera. The profile shown in Fig 4.4 corresponds completely to the 50μmX50μm cross section, confirming the confinement and propagation of the light. To measure the propagation loss of the

molded waveguide, a cut back method was used to extrapolate the value. A multimode fiber with 62.5μm core diameter was used to capture the output light. As Fig 4.4 shows, the propagation loss is estimated to be 0.26dB/cm. This value is higher than the 0.16dB/cm result in [8], attributed to the waveguide curvature in the current structure and the residue sidewall roughness. The 0.72dB intersection with vertical axis corresponds to the coupling loss caused by reflection and scattering. The total insertion loss of the 51cm long waveguide, fiber-in-fiber-out, is -15.1dB, with adjacent channel cross talk lower than -31dB.

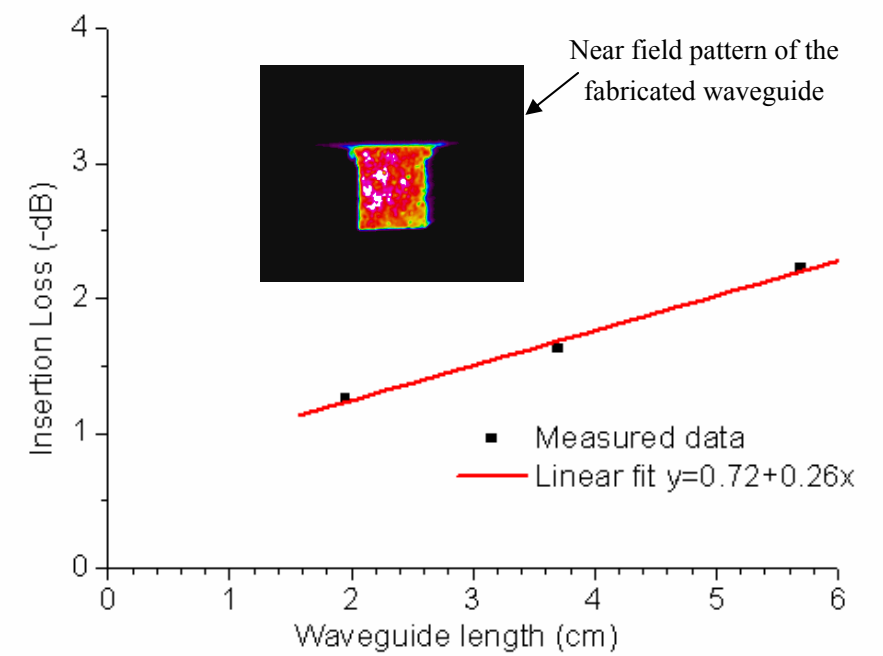

Fig 4.4 The insertion loss as a function of waveguide

The bandwidth-limiting factors of optical waveguides are either the optical loss or the optical dispersion. With the improved quality of the polymer materials, the large modal dispersion of the multimode waveguide could become the dominant bottleneck that prevents higher speed signal, compared with the optical loss. A widely used measuring method will compare a 10Gbps or a pulse signal before and after propagating through the waveguide, usually in terms of jitter variation [11] and pulse width [13]. However, the measurement precision is directly limited by the

responsivity of the photodetector and the oscilloscope. Optical autocorrelation can provide a much better measurement accuracy up to femto-second level [14]. In our measurement, an optical pulse generated from a femto-second laser is launched to the 51cm long waveguide through a 9μm core single mode fiber. The output power is connected by a 62.5μm core multimode fiber, and finally fed into an FR-103MN autocorrelator from Femtochrome Research Inc. The optical pulses in time domain with and without the waveguide were recoded in Fig 4.5. The input pulse has double peaks and a half width of 2.2ps, which is much longer than the pulse directly from the laser source, indicating the significant dispersion from the 62.5μm core multimode fiber. The output pulse after inserting the waveguide is broadened in the time domain with the separation of the second peak.

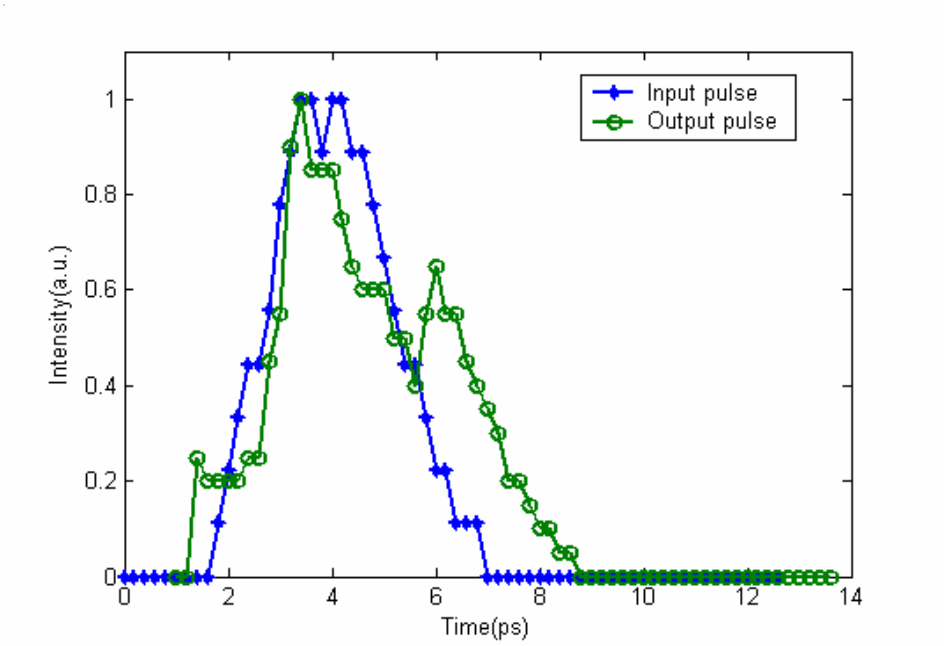

Fig 4.5 Optical pulses in the time domain

The frequency domain responsivity of the two pulses are shown in Fig 4.6. The 3-dB bandwidth of the 51cm long waveguide is found to be 150GHz. Compared with multimode fibers, a similar cross section multimode waveguide has a much larger modal dispersion, which is a reasonable result of the high order modes existence shown in Fig 4.4. However, a single waveguide channel can still provide at

least 100Gbps signal transmission, leaving a sufficient overhead bandwidth for board level optical interconnects.

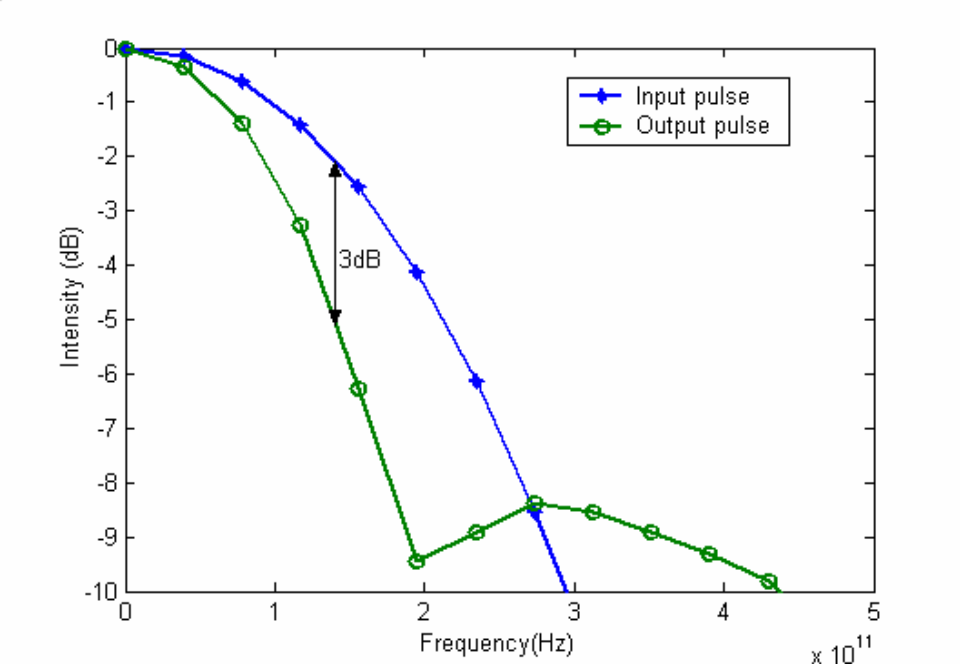

Fig 4.6 Optical pulses in the frequency domain

In conclusion, we have fabricated a 51cm-long waveguide array on a PMMA sheet by the silicon hard-molding method. With the oxidation-smoothing process, the silicon surface roughness is significantly reduced. Very precise replication from the original silicon master mold to the PMMA sheet was achieved across the entire 4" wafer through hot embossing. The hard-molded waveguides demonstrated a propagation loss of 0.26dB/cm at 850nm. To the best of our knowledge, this is the longest successfully molded waveguide that has ever been reported. The 150GHz optical bandwidth of the waveguide will provide a sufficient overhead for high speed signal transmission. Plus the low fabrication cost and mass producibility, the waveguide array shows great potential for board level optical interconnects.

4.3 UV Embossed Waveguide Array

Compared with hot embossing method mentioned above, the proposed UV embossing in this sub-chapter requires room temperature and zero pressure during the

molding process. Additionally, we will also demonstrate a much more efficient surface treating method to reduce the surface roughness of the silicon master mold.

The surface roughness of the silicon master mold directly influences the quality of the molded thin film waveguide.The high etching rate (>1μm/min) and the alternating etching-passivation step in the DRIE process leave sidewalls with a coarse and corrugated surface. The roughness will be transferred to the polymer substrate and causing a significant amount of scattering. Several attempts including chemical wet etching [15], oxidation-and-smoothing [12], have produced obvious improvement over the raw surface. In this subchapter, we present a much easier spin-coated method that has never been reported before. The silicon surface coated with a thin layer of photoresist outperforms the surfaces treated by any other method in terms of roughness. Atomic force microscopy (AFM) images are taken, and post measurement analysis with fast Fourier transform (FFT) is executed to quantitatively characterize the surface. Fig.2 (a) and (b) are the AFM images of the silicon side wall after DRIE and the one spin coated with a 0.9μm thick AZ5209 photoresist. The root mean square (rms) is decreased from 6.9nm to 0.44nm.

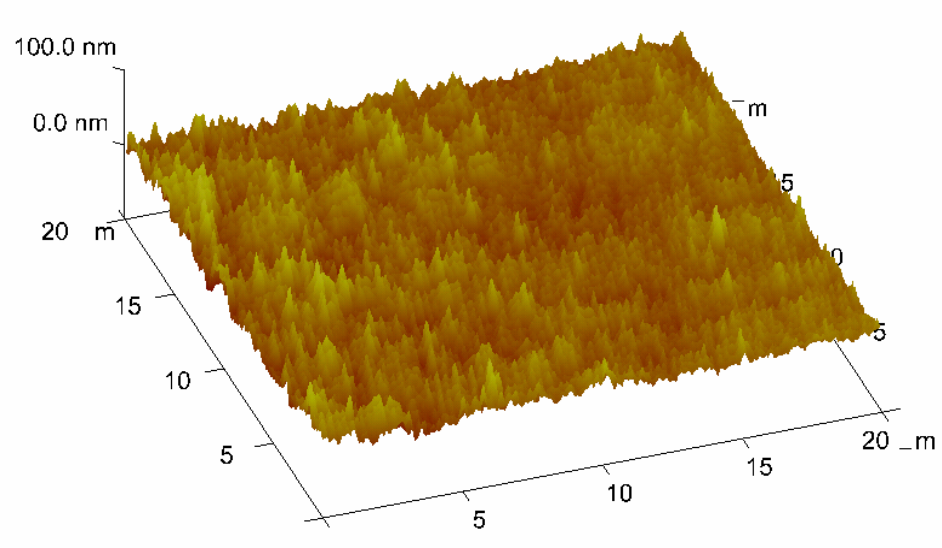

Fig 4.7 (a) AFM images of silicon surfaces after DRIE

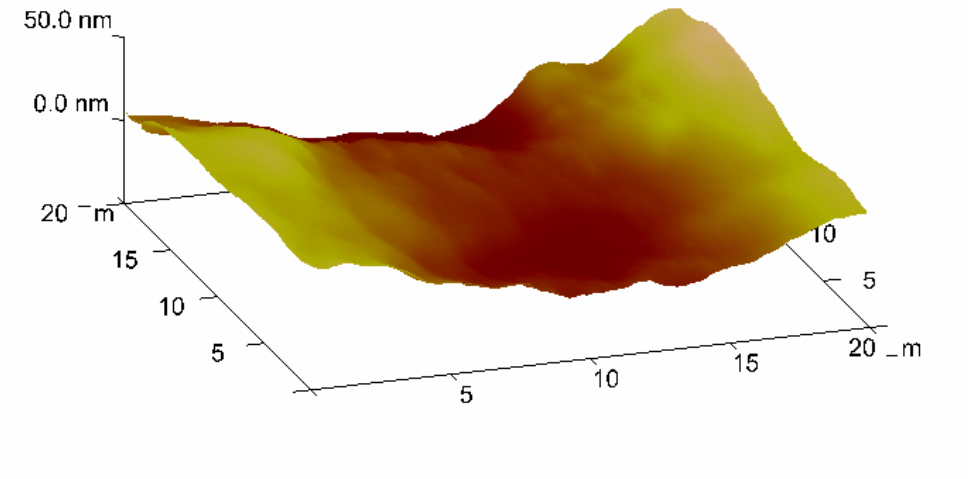

(b)

Fig 4.7 (b) AFM images of silicon surfaces after spin coated with AZ5209

The 2-dimentional spatial power spectrum density (PSD), obtained by the FFT to the measured AFM data, clearly compared the effect of different surface treatments in Fig 4.8 The other two samples are wet etched by 7M KOH solution in 75ºC for 30sec, and 1050ºC wet oxidated for 4 hours plus a 10min buffered oxide etchant (BOE) stripping. It is interesting to point out that in the low spatial frequency range (<0.1/μm), the PSDs are approximately the same for all of the surfaces, which means the long range fluctuation is not affected by the aforementioned surface treating methods. Scattering loss is primarily determined by high spatial frequency PSD, which is comparable or shorter than the propagated wavelength. In this range, the PSD of the spin coated surface is at least one order lower than the oxidation-smoothing method, two orders lower than the wet etched or raw surfaces.

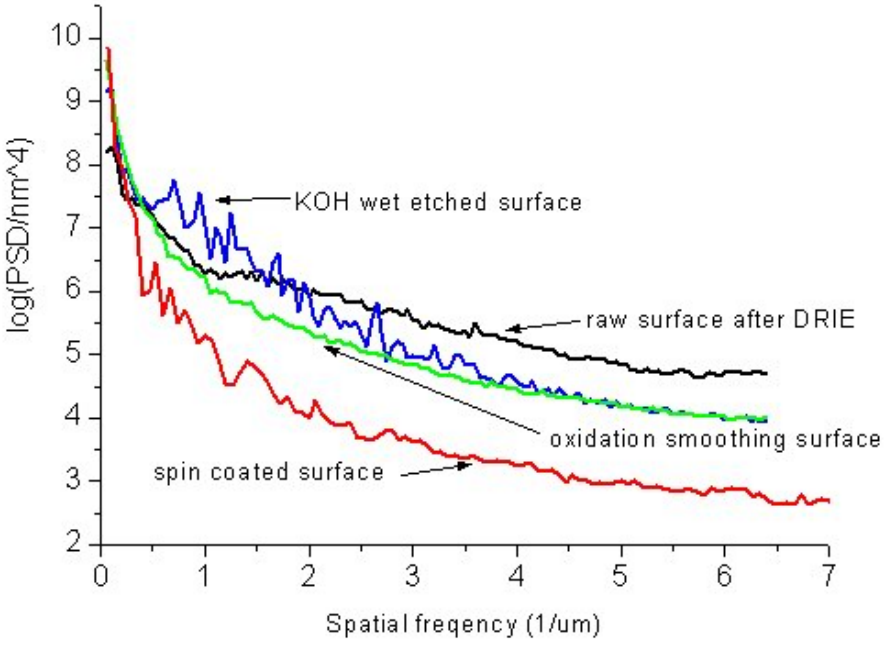

Fig 4.8 PSD of silicon surfaces after different treatment

After the master mold is successfully prepared, which is composed of twelve parallel straight waveguides with 250μm pitch and 50μmX50μm cross section, a hard molding process using UV embossing method is conducted on a 100μm thick topas film. The topas film is chosen because of its transparency and high glass transition temperature (Tg>160ºC). The main procedure is divided as the following steps shown in Fig 4.9:

(a) First, a layer of UV curable bottom cladding material, WIR30-450 (from ChemOptics, with a refractive index of 1.45 at 850nm wavelength) is spin coated on the topas film substrate.

(b) In the second step, the master mold is brought in contact with the spin-coated substrate and UV cured for 8 minutes inside a nitrogen atmosphere.

(c) To separate the polymer substrate with the silicon master mold, the sample is merged into acetone to quickly dissolve the photoresist layer on top of the silicon pattern. The intact polymer substrate will detach the master mold within 1 minute. After forming the desired trenches, a core material WIR30-470 with a higher

refractive index (1.47 at 850nm) is used to fill them up. The excess polymer is scraped off, and the same amount of UV dose is applied to cure the core layer.

(d) In the last step, the sample is spin coated with another layer of WIR30-450, which functions as the top cladding, and followed by a UV curing process.

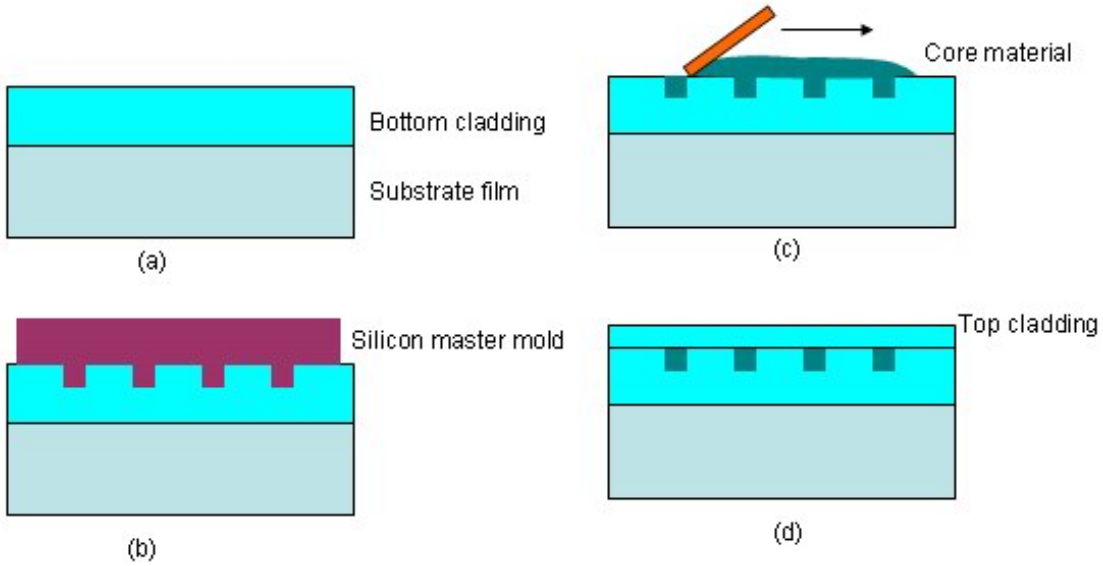

Fig 4.9 UV embossed molding process of the polymer waveguide array

Unlike any published molding process, for instance, hot embossing [9] or PDMS soft-molding [8], there are no fabrication steps associated with pressure or heating. This ensures the replicated waveguide array exactly the same size as the silicon master mold. The fabrication cost and energy consumption is lowered as well. The propagation loss of the waveguide is measured by the cutback method. An 850 nm VCSEL light was coupled into the waveguides by a 50/125μm graded index multimode fiber and the output light was then coupled into a photodetector by a 62.5/125μm graded index multimode fiber. The measured propagation loss was 0.09dB/cm at 850 nm. This data is close to the planar waveguide loss of 0.05dB/cm provided by the material vendor. We also investigated the waveguide loss fabricated by other techniques, as listed in Table 4.1. It clearly shows that the spin coated surface treating method, plus the room temperature, zero pressure UV embossing process significantly reduced the waveguide loss.

Table 4.1 Waveguide propagation loss of different fabrication techniques

Mold	Fabrication	Surface treating method	Waveguide(bottom cladding/core/top cladding)	Propagation loss (dB/cm)
Silicon	UV embossing	Spin-coated	WIR-450/WIR-470/WIR-450	0.09
Silicon	Hot embossing	Oxidation-smoothing	PMMA/WIR500/WIR470	0.26
Silicon	Hot embossing	Wet etched	PMMA/WIR500/WIR470	0.47
PDMS	Soft molding	N/A	WIR-450/WIR-470/WIR-450	0.16

As a summary for this subchapter, a novel spin-coated surface treating method is used to smooth the silicon master mold, and obtained a waveguide propagation loss as low as 0.09dB/cm with a UV embossing molding process.

4.4 References

[1] R. Yoshimura, M. Hikita, S. Tomaru, and S. Imamura, “Low-loss Polymeric Optical Waveguides with 45° mirrors”, Jpn. J. Appl. Phys., Vol. 37, pp. 3657-3661, 1998

[2] A. Borreman, S. Musa, A.A.M. Kok, M. B. J. Diemeer and A. Driessen, “Fabrication of Polymeric Multimode Waveguides and Devices in SU-8 Photoresist Using Selective Polymerization” Proceedings Symposium IEEE/LEOS Benelux Chapter, 2002, Amsterdam

[3] L. Eldada, C. Xu, K. Stengel, L. Shacklette, and J. T. Yardley, “Laserfabricated low-loss single-mode raised-rib waveguiding devices in polymers,”J. Lightwave Technol., vol. 14, pp. 1704–1713, 1996.

[4] A. Neyer, T. Knoche, L. Moller, and R. Klein, “Low-loss passive polymer waveguides at 1300 and 1550 nm,” in Proc. Polymer Optical Fibers Conf., 1994, pp. 169–171.

[5] H. Kragl, R. Hohmann, C. Marheine, W. Pott, and G. Pompe, “Low cost monomode, integrated optics polymeric components with passive fiber-chip coupling,” Electron. Lett., vol. 33, pp. 2036–2037, 1997.

[6] G. Pompe, M. Jolinck, S. Kalveram, S. Lehmacher, S. Rudolph, and A. Neyer, “Technology of hot embossed thermo-optic switches in plastics with passive fiber coupling,” in Proc. Plastics in Telecommunications Conf., vol. 8, 1998, pp. 28–29.

[7] A. Brauer and P. Darmberg, “Polymers for passive and switching waveguide components for optical communications,” in Proc. SPIE, vol. CR63, 1997, pp. 334–349.

[8] L.Wang, X.Wang, W.Jiang, J.Choi, H.Bi, and R.T.Chen, “45º polymer-based total internal reflection coupling mirrors for fully embedded intraboard guided wave optical interconnects”, Applied Physics Letters, 87, 141110, 2005

[9] K.B.Yoon, C.G.Choi, S.P.Han, “Fabrication of multimode polymeric waveguides by hot embossing lithography,” Jap.J.of Applied Physics, 43, pp.3450-3451, 2004

[10] H.Mizuno, O.Sugihara, T.Kaino, M.Hosino, “Low-loss polymeric optical waveguides with large cores fabricated by hot embossing”, Optics Letters, 28, pp.2378-2380, 2003

[11] L. Dellmann, R. Dangel, R. Beyeler, C. Berger, F. Horst, B.J. Offrein, and G.-L. Bona, “Polymer waveguides for highspeed optical interconnects,” in EOS

Topical Meeting Optics in Computing (European Optical Society, 2004), pp.131–132.

[12] K.K.Lee, D.R.Lim, and L.C.Kimerling, “Fabrication of ultrlow-loss Si/SiO2 waveguides by roughness reduction,” Optics Letters, 26, pp.1888-1890, 2001

[13] F. E. Doany, P. K. Pepeljugoski, A. C. Lehman, J. A. Kash, and R. Dangel, “Measurement of Optical Dispersion in Multimode Polymer Waveguides,” Proceedings of the IEEE–LEOS Summer Topical Meetings, 2004, pp. 31–32.

[14] Z.A.Yasa and N.M.Amer, Optics Commun., “A rapid-scanning autocorrelation scheme for continuous monitoring of picosecond laser pulses”, Vol.36, 406 (1981)

[15] D.Nilsson, S.Jensen and A.Menon, “Fabrication of silicon molds for polymer optics,” J.of Micromechanics and Microengineering, 13, pp.S57-S61, 2003

Chapter 5 System Integration for Board Level Optical Interconnects

This chapter will describe the coupling efficiency between the optical waveguide and the micro-mirror, and the optical layer integration with the VCSELs and p-i-n photodiodes.

5.1 Analysis of 45º Micro-Mirror

Waveguide couplers play a key role for the realization of three-dimensional fully embedded board-level optical interconnection owing to their surface-normal coupling of optical signals into and out of in-plane waveguides. A waveguide grating [1] as well as a 45º waveguide mirror based coupler [2] can serve as a surface normal coupler. However, the grating based approach requires precise control of grating parameters for efficient coupling and usually has low tolerance to wavelength variations. Therefore, we employed 45° total internal reflection (TIR) coupling mirrors at both ends of waveguides because they are easy to fabricate, reproducible, and relatively insensitive to wavelength variations, and can provide a high coupling efficiency.

The coupling efficiency from the VCSEL to the waveguide can be simulated either by Gaussian beam method [3] or ray tracing method [4]. Ray tracing method assumes the beam from VCSEL will travel in a straight line with 8º-12º divergent angle (4º-6º half-width divergent angle), which is only true for far field radiation. The distance from VCSEL to waveguide coupler is usually 50~500μm. At this range, ray tracing method will possibly underrate the coupling efficiency. Gaussian beam optics can simulate the near field behavior for which ray tracing method cannot. Let's take a review of Gaussian beam optics and compare its result to real VCSEL devices.

Figure 5.1(a) illustrates waveguide with 45° mirror coupler and transparent substrate. The VCSEL is bonded to the substrate; hence, laser light travels through the substrate and bends at right angle at the mirror facet. The transparent substrate is

optically isotropic. Figure 5.1(b) illustrates Gaussian beam propagation in homogeneous medium.

Propagation angle at mirror surface θ(r,z) can be calculated from the radius of curvature of wavefront R(z) and distance from center *r* [5].

$$\theta(r,z) = \tan^{-1}\left(\frac{R(z)}{r}\right) \tag{5.1}$$

The radius of curvature R at any z of the wave-front is given by equation

$$R(z) = z\left(1 + \frac{\pi\omega_0{}^2 n}{\lambda z}\right), \quad z_0 = \frac{\pi\omega^2{}_0 n}{\lambda}, \quad \omega(z) = \omega_0\sqrt{1+\left(z/z_0\right)^2} \tag{5.2}$$

where, λ is wavelength, ω_0 is the beam waist at VCSEL surface and ω(z) is the beam width at z. The half-width divergent angle [5] is given by

$$\theta_0 = \frac{\lambda}{n\pi\omega_0} \tag{5.3}$$

The electric field distribution E(r,z) of Gaussian beam in homogeneous medium is given by

$$E(\mathrm{r},\mathrm{z}) = E_0\frac{\omega_0}{\omega(z)}e^{\left\{-i[kz-\delta(z)]-(r^2)[\frac{1}{\omega^2(z)}-\frac{ik}{2R(z)}]\right\}} \tag{5.4}$$

and the intensity distribution of the Gaussian beam is

$$I(r,z) = |E(r,z)|^2 = E_0\left\{\frac{\omega_0}{\omega(z)}\right\}^2 e^{\left(-2(r^2)\frac{1}{\omega^2(z)}\right)} \tag{5.5}$$

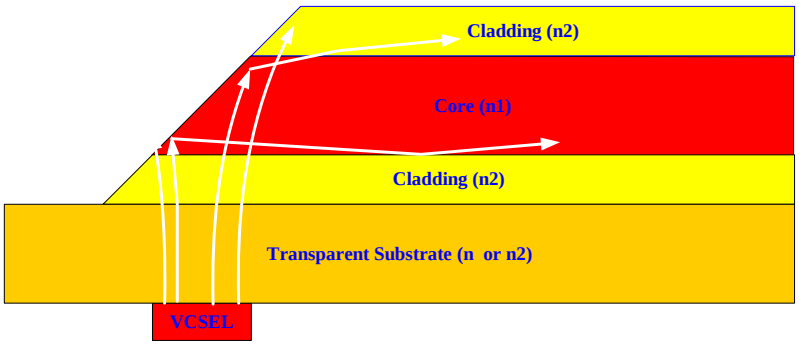

(a)

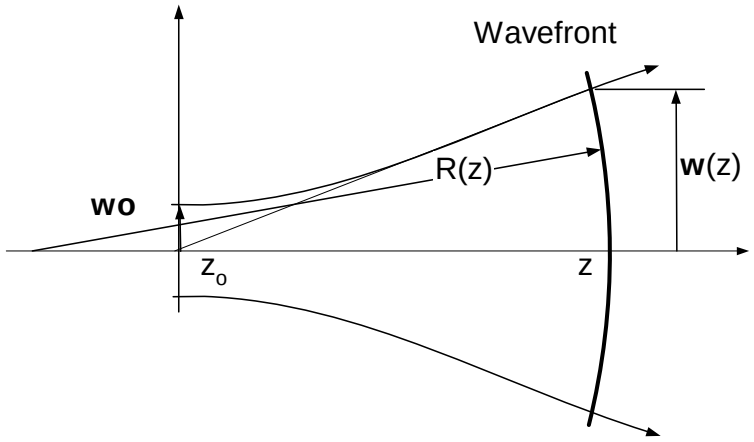

(b)

Figure 5.1 Coupling Mechanism (a) Diagram of the coupling mechanism (b) Gaussian beam propagation in a homogeneous medium.

Therefore, the coupling efficiency, η can be calculated by

$$\eta = \frac{\int_{-r_c}^{r_c} |E(r,z)|^2 \, dr}{\int_0^{\infty} |E(r,0)|^2 \, dr} = \left(\frac{\omega_0}{\omega(z)} \right)^2 \int_{-r_c}^{r_c} |E(r,z)|^2 \, dr \tag{5.6}$$

where, r_c is the maximum radius at the mirror facet which correspond to the acceptance angle of the waveguide. The coupling efficiencies between VCSEL and square (50μmX50μm) waveguide with Δn=0.01(refractive index difference between core and cladding) is almost 100% with the substrate thickness of 127μm and the VCSEL aperture of 12μm. However, the half-width divergent angle calculated by Eqn (5.3) is only 1.7º, compared with reported real VCSEL devices of 5~6º [6], which is 3~4 times larger than the ideal Gaussian beams.

A more accurate simulation method herein adopted is called M2 factor revised Gaussian beam [7], which semi-empirically introduces a M2 factor to define the beam quality. The M2 factor defines the Gaussian beam to have the highest quality with M2=1, and multimode beams will have a rating of M2>1. M is defined as

$$M = \left(\frac{w_{0M}}{w_0} \right) \tag{5.7}$$

where w_{0M} is the VCSEL aperture, and w_0 stands for the equivalent Gaussian beam waist. The modified beam intensity $I(r,z)$ can be expressed as

$$I(r,z) = \frac{2}{\pi w_{0M}^2(z)} \exp\left(\frac{-2r^2}{w_{0M}^2(z)}\right) \tag{5.8}$$

where

$$w_{0M}(z) = w_{0M}\left[1 + \left(\frac{M^2 z\lambda}{\pi w_{0M}^{\ 2}}\right)^2\right]^{1/2} \tag{5.9}$$

This definition implies that a VCSEL beam will be larger than the corresponding single mode beam, and diverge more rapidly. The VCSEL diode in our simulation has an optical aperture of 12μm and a real half beam divergent angle of 12º. Accordingly, the M factor calculated from Eqn(5.7) is 2.6. The distance from the VCSEL to the center of the 45° waveguide coupler is 50μm (with 25μm top cladding). With an index contrast of 0.02 between the core and cladding, the waveguide has an acceptance angle of 9.46°. Any incident light from the waveguide coupler has a larger incident angle than 9.46° will eventually radiated from the waveguide. In the aforementioned model, the metal coated mirror is assumed to have 100% reflectivity. Fig 5.2 shows the coupling efficiency from the 12μm aperture VCSEL to the 50μmX50μm waveguide through the micro-mirror as a function of the misalignment. The maximum coupling efficiency is 90.5%. There is a pretty flat plateau with ±25μm toleration to achieve over 80% coupling efficiency. But this is obviously lower than 100% coupling efficiency. Fig 5.3 shows the coupling efficiency from the VCSEL to the waveguide as a function of the micro-mirror deviation angle from 45º. Unlike the simulation result from [3], the coupling efficiency is very sensitive to the angular deviation when Δn equals 0.01 and 0.02. This indicates the divergent angle of the VCSEL diode is close to waveguide acceptance angle. Note that if the micro-mirror has a Δθ deviation angle, the reflected beam will shift 2Δθ. This could exacerbate the case. However, for strong index contrast waveguide (Δn=0.05), which has

a larger acceptance angle, the angular deviation tolerance can be as large as ±4º for 70% coupling efficiency.

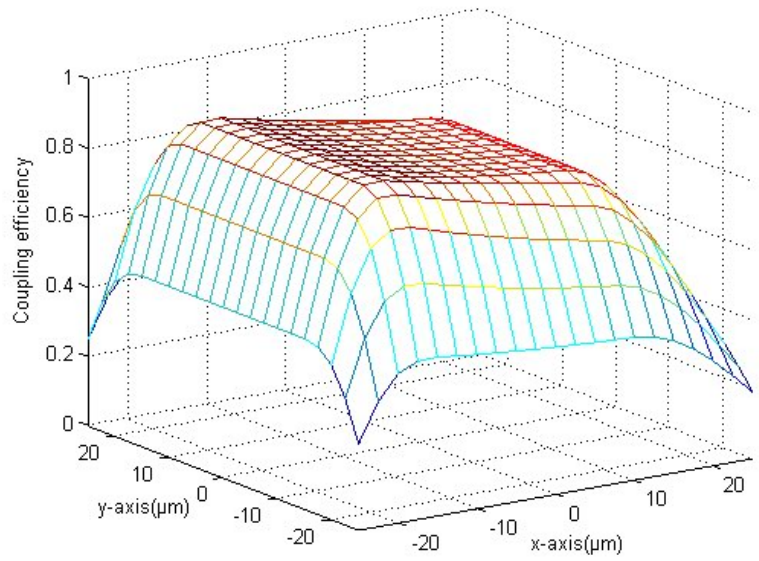

Fig 5.2 Simulated coupling efficiency of the 45º micro-mirror as a function of the misalignment of the two axes

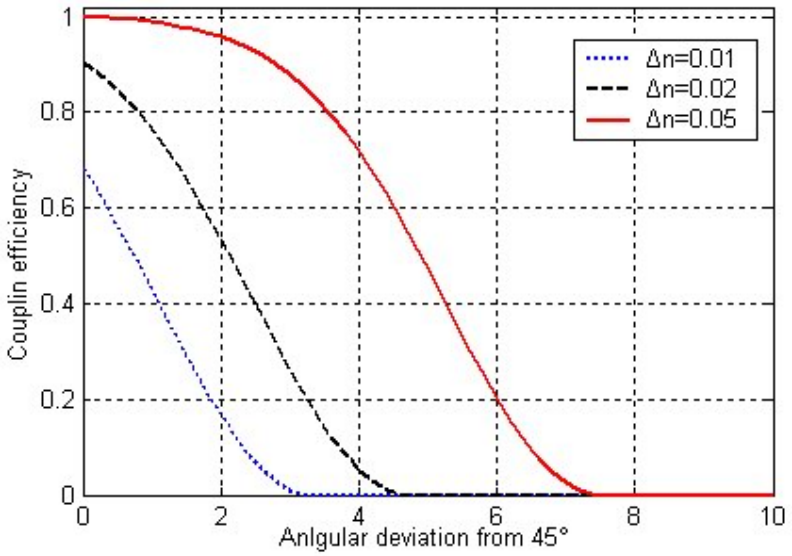

Fig 5.3 Simulated coupling efficiency of the 45º micro-mirror as a function of the angular deviation

Another interesting approach to achieve a higher coupling efficiency with the multimode waveguide may employ a sphere mirror instead of a flat 45º mirror, as shown in Fig 5.4, because the concave mirror can focus the divergent beam from the VCSEL and make it more parallel. The radius of the sphere mirror R can vary from 50μm to infinity, in another word, flat mirror.

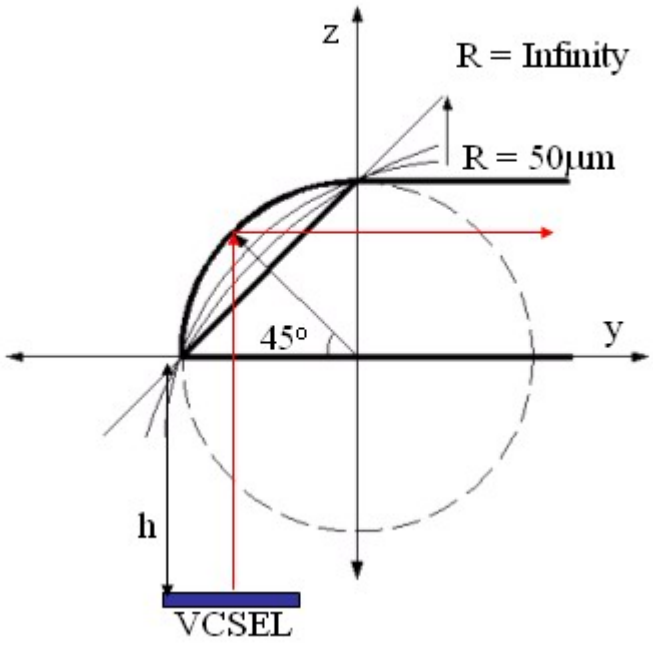

Fig 5.4 Schematic of the sphere mirror

Fig 5.5 shows the coupling efficiency from as a function of the radius. When R is very small, the sphere mirror can over focus the incident beam, and a significant fraction of the light has a larger incident angle than the waveguide acceptance angle. The optical coupling efficiency increases as the radius increase, and reaches a peak value as R stays around 400μm. If R increases further, the sphere mirror becomes more and more flat, losing the focusing function. The coupling efficiency will decrease gradually to that of the 45º micro-mirror mentioned above. Fig 5.5 also shows the coupling efficiency for different substrate thickness. The thicker the substrate is, the larger the beam width will become and the larger the divergent angle will be, resulting in a decreased coupling efficiency.

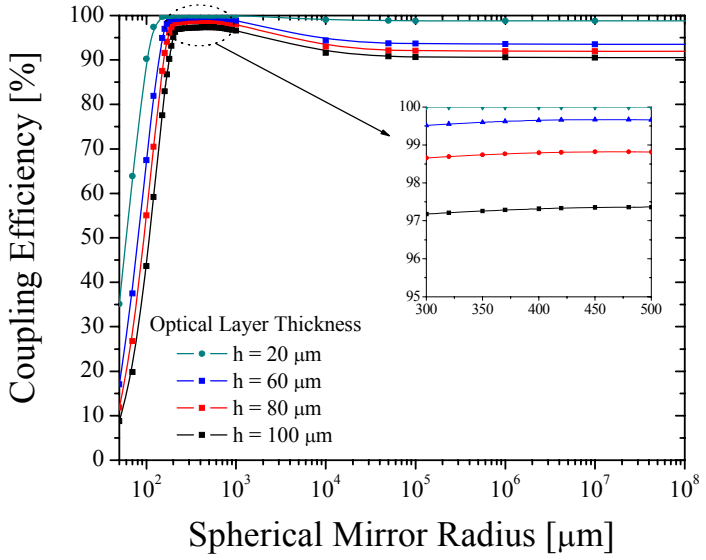

Fig 5.5 Coupling efficiency as a function of the sphere mirror radius for difference substrate thickness waveguide

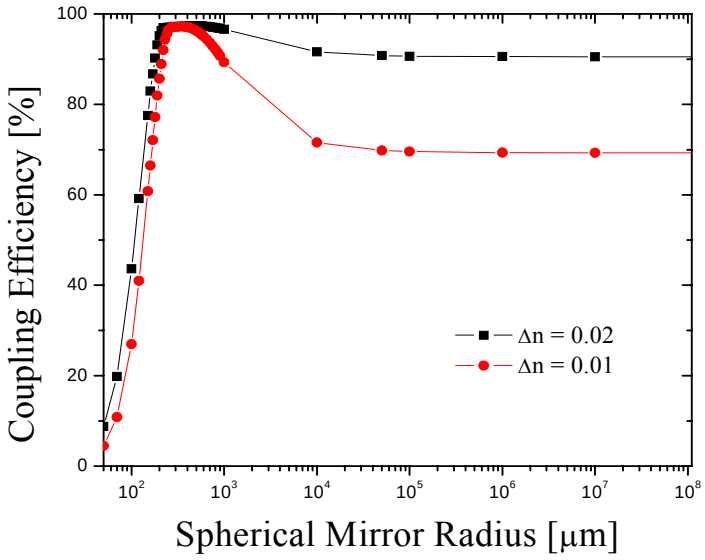

Fig 5.6 Coupling efficiency as a function of the sphere mirror radius for difference index contrast waveguide

Fig 5.6 shows the coupling efficiency for the waveguide with core-cladding index contrast of 0.01 and 0.02. As we can see, the sphere mirror will work much better for low index contrast waveguide, because the low index contrast waveguide is more sensitive to the incident beam angle.

5.2 45º Micro-mirror Fabrication and Testing Results

The waveguide micro-mirror can be fabricated by the one-step pattern transfer method described in [2]. After the DRIE process, the silicon master mold is mechanically polished on both ends using a specially designed 45º stage. The polishing process started from 30μm grits lapping pad to 1μm grits. Finer polishing is not necessary since the following spin-coated surface treating process will smear the remained roughness. The 45º titled end surfaces will transfer to the UV cross linked polymer substrate that is in direct contact with the master mold, as Fig 5.7 (a) shows. The waveguide array pattern, together with the desired micro-mirror coupler, is replicated in a negative shape from the master structure simultaneously. To further reduce the fabrication effort described in [2] using standard photolithography and followed lift-off process, the sample is covered by a polymer thin-film mask with opened mirror windows. This reusable thin film mask will shield the deposition of metal layer on the polymer substrate except in the open windows, as Fig 5.7(b) indicates. An electron beam evaporated 200nm thick gold layer is deposited to form the high reflective mirror. After removing the thin film mask, the UV embossed trenches in Chap 4.3 with metal mirrors on both ends shown in Fig 5.7(c), can be filled with the core material in the further procedure.

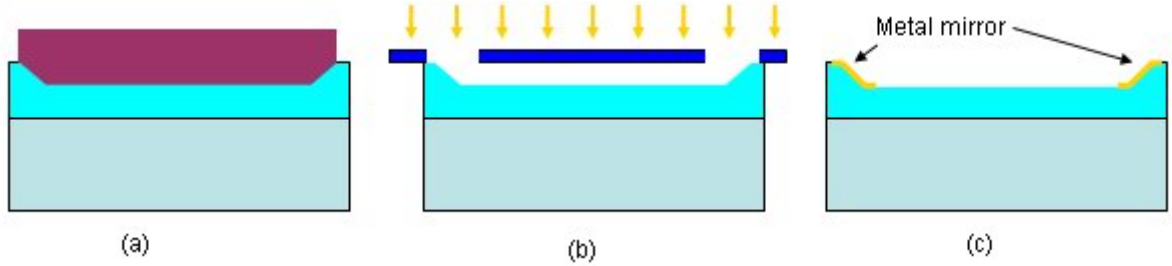

Fig 5.7 Fabrication of 45º waveguide micro-mirror (a)replicate the master mold with 45º titled facets (b) covered by thin film mask with opening windows (c) Deposited metal mirrors

To observe the light transmission over the UV embossed waveguide array with the embedded 45º micro-mirrors, the sample is fixed on an evacuated holder. A 9μm core diameter fiber coupled with a 633nm He-Ne laser vertically launched the input light into the waveguide mirror, as Fig 5.8 (a) shows. To co-illuminated the twelve mirror array, the input fiber is purposely pulled 5mm above the mirror surface. At the back end, the output field patterns are projected onto an image scope, which can be viewed through a monitor. The output pattern of the twelve reflecting mirrors is shown in Fig 5.8 (b). We measured the total insertion loss at 850nm of the twelve channels. By comparing the results with the values for the straight waveguides of the same length and dimension, we extracted the total coupling loss of the front and back mirror. If the two mirrors have the same coupling efficiency, which is approximately correct, the obtained coupling loss is 0.7~1.5dB for each mirror in Fig 5.8 (c). In another word, the highest coupling efficiency we can get is 85%.

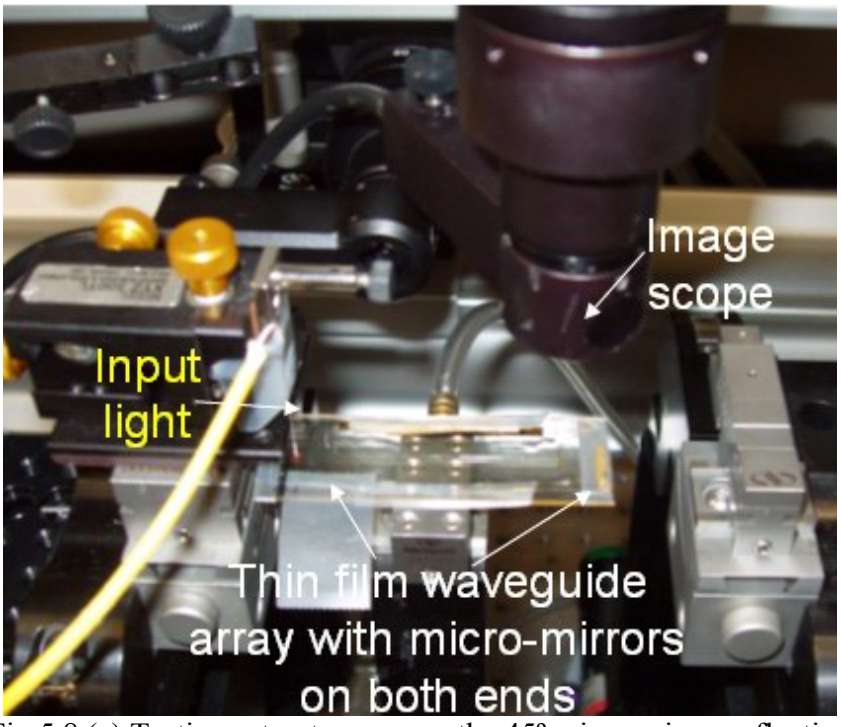

Fig 5.8 (a) Testing setup to measure the 45º micro-mirror reflection

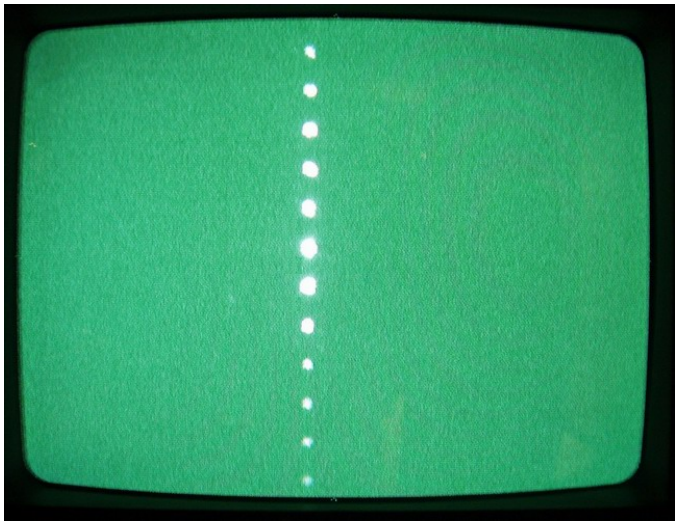

Fig 5.8 (b) Output pattern of the 1X12 micro-mirror array

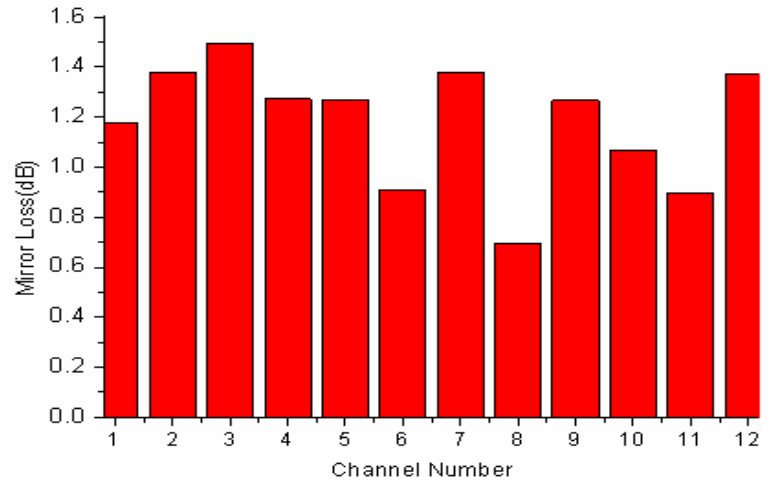

Fig 5.8 (c) Measured coupling loss of the 1X12 micro-mirror array

5.3 Experimental Characterization of the 4-bit TTD Module

The integration of optoelectronic devices with the flexible waveguide film is the most important process among the whole integration steps, including the final laminating process with the PCB. The proposed integration method through vias involves the following processes [3]: copper foil laminating, pattern alignment from back side, laser drilling through the topas film substrate, device bonding and copper electroplating.

Although we had successfully bonded VCSELs and photodiode array with the thin film waveguide, there are still difficulties to implement the thorough process due to its complexity. As a simpler alternative scheme, a via-free process is proposed as Fig 5.9:

(a) Thin film waveguide array with embedded metal mirrors on both ends

(b) The polymer film is polished on both sides and stops 20μm before the mirror position. This process can be precisely controlled by polishing time and rate. And then, the VCSELs and photodiode array are bonded to the thin film waveguide with a photoaligner. The alignment error can be controlled within ±5μm in both lateral and longitudinal direction.

(c) Flip-chip bonding balls are deposited on the bonding pads of the VCSELs and photodiode arrays. The total height of the optical layer is within 170μm, which will fit the flip-chip requirement.

(d) In the last step, the optical layer is laminated inside PCB layers with an easy alignment.

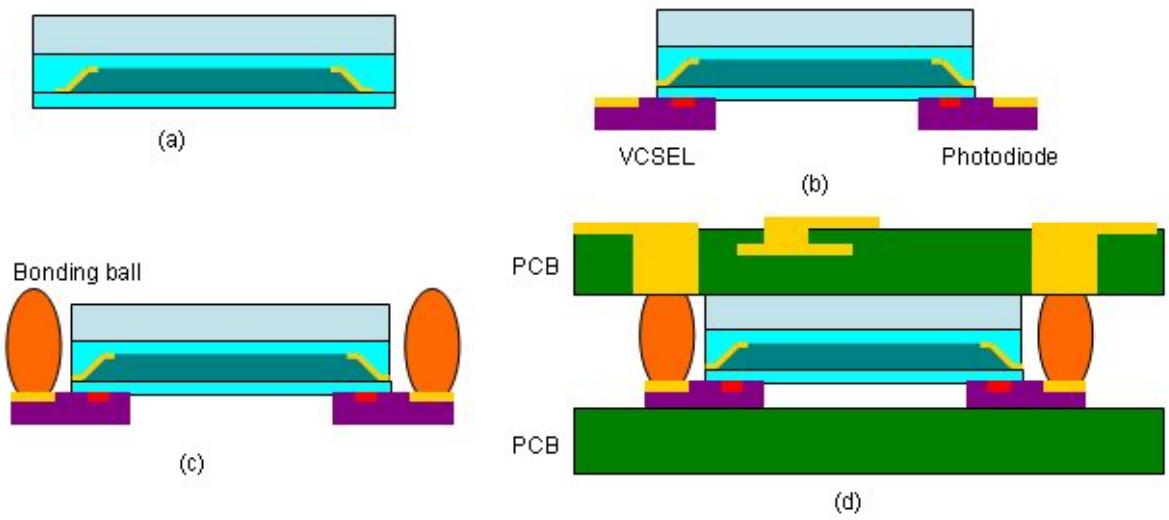

Fig 5.9 Simplified Integration procedure of fully embedded board level optical interconnects

For the evaluation of the optical system performance, only step (a) and (b) is carried out. No signal transmissions have ever been demonstrated in our previous papers

on the fully embedded structure because the active optical devices, VCSELs and p-i-n photodiodes, are blocked from any electrical pads by the polymer film substrate. With the polishing of the substrate, the active optical devices can be accessed by microwave probes. Fig 5.10 shows the measurement setup for the optical transmission.

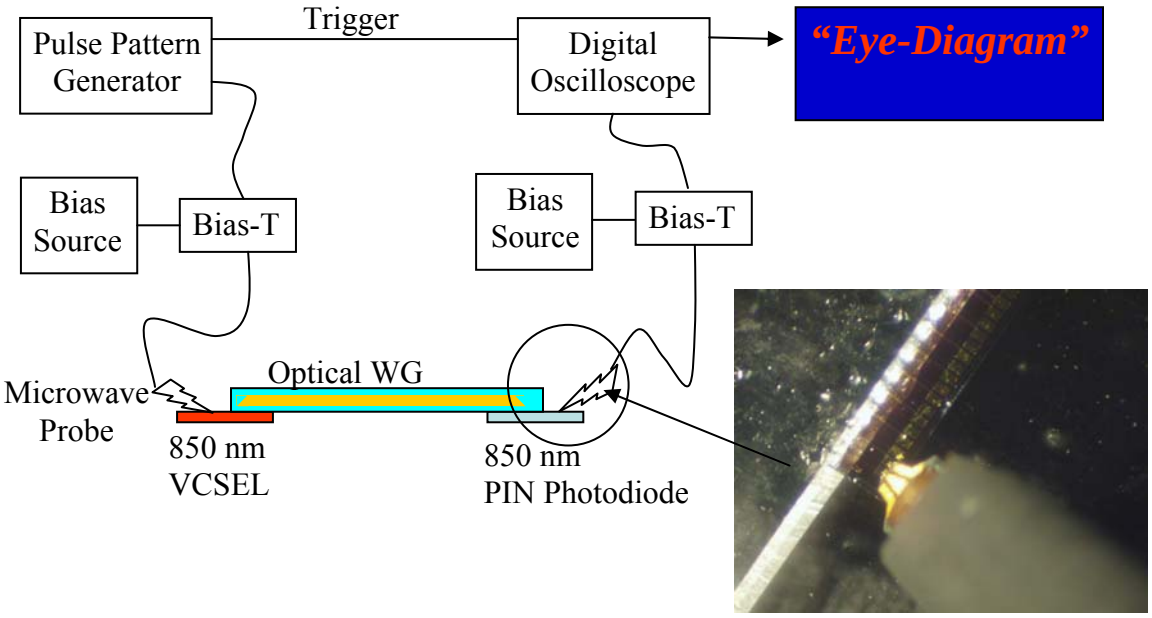

Fig 5.10 Schematic diagram of the measurement setup for the assembled optical system

We biased the VCSEL with a lasing current, and measured the photo current from the p-i-n diode, the response curve is shown in Fig 5.11. The maximum response from the photodiode is 300μA.

The VCSEL was then biased at 5mA and modulated by ±0.3V 2.5Gbps pseudo random signal. The response from the photodiode is directly input into a digital oscilloscope without any pre-amplification. The measured signal eyediagram is shown in Fig 5.12 with a Q-factor of 7.41.

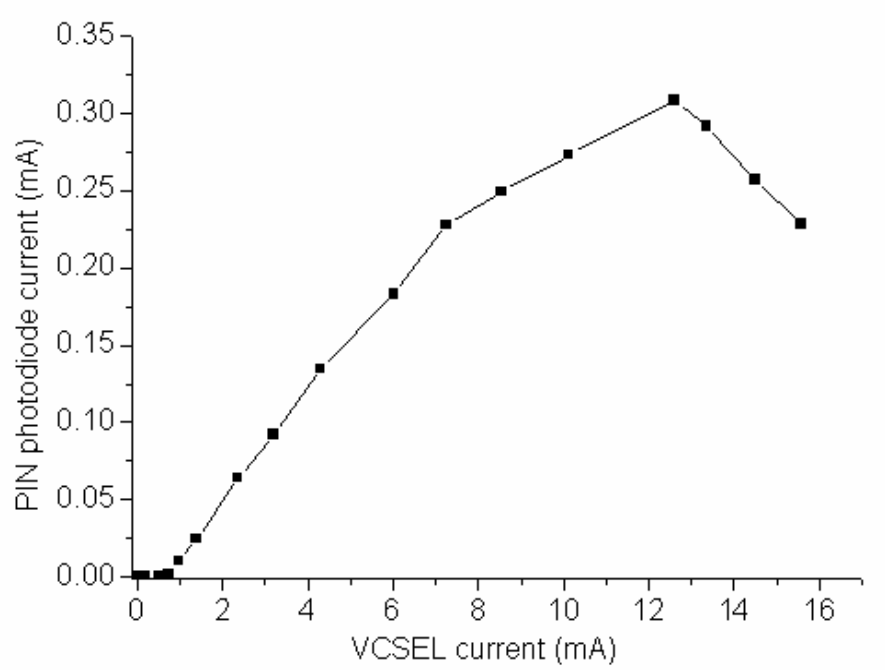

Fig 5.11 photo current as a function of the VCSEL current

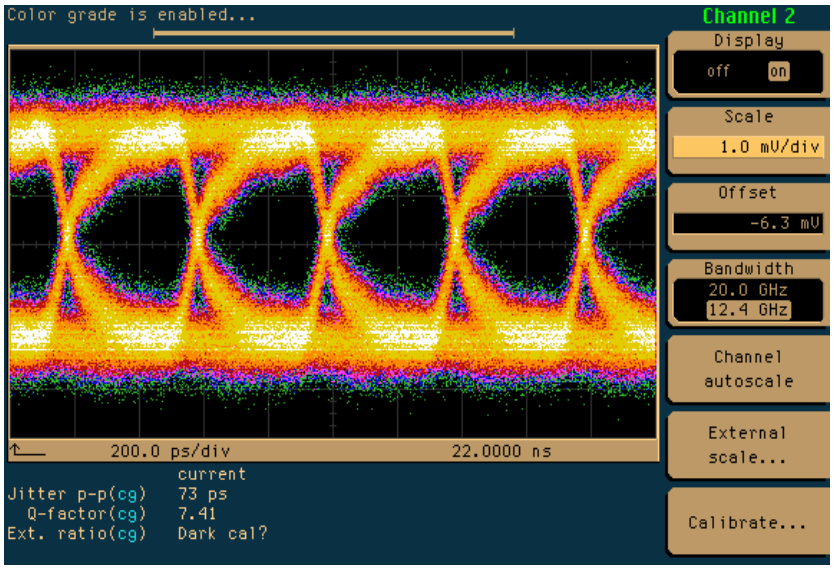

Fig 5.11 2.5Gbps eyediagram measured from the photodiode

5.4 Summary

In this chapter, the coupling efficiency of the 45º micro-mirror is simulated by M^2 factor revised Gaussian beam method. The 45º micro-mirror is formed by a one-step pattern transfer from the master mold, and got metal coated with a photolithography-free process. The highest coupling efficiency of the micro-mirror is 85%. The system integration is simplified by a polish-bonding scheme, which will require less fabrication effort and reduce the cost. For the first time, we implemented the light transmission over the optical fully embedded architecture with 2.5Gbps digital signal. The maximum photocurrent is 300μA.

5.6 References

[1] R.T.Chen, L.Lin, C.Choi, Y.Liu, B.Bihari, L.Wu, S.Tang, R.Wickman, B.Picor, M.K.Hibbs-brenner, J.Bristow, and Y.S.Liu, "Fully Embedded Board-Level Guided Wave Optoelectronic Interconnects", Proc. Of the IEEE, 88,6, pp.780-794, 2000

[2] L.Wang, X.Wang, W.Jiang, J.Choi, H.Bi, and R.T.Chen, "45º polymer-based total internal reflection coupling mirrors for fully embedded intraboard guided wave optical interconnects", Applied Physics Letters, 87, 141110, 2005

[3] Choi, C.; Lin, L.; Yujie Liu; Jinho Choi; Li Wang; Haas, D.; Magera, J.; Chen, R.T., "Flexible optical waveguide film fabrications and optoelectronic devices integration for fully embedded board-level optical interconnects ," IEEE J. of Lightwave Technology, 22, pp.2168 – 2176, 2004

[4] J.H. Wu, J. Wu, J. Bao, and X. Wu, "Soft-lithography-based optical interconnection with high misalignment tolerance," Optics Express, Vol.13, No.6, pp.6259-6267, 2005

[5] B. E. A. Saleh, and M. C. Teich, "Fundamentals of photonics," in Chap. 3, John Wiley & Sons (New York), (1991).

[6] C.Debaes, M.Vervaeke, V.Baukens, H.Ottevaere, P. Vynck, P. Tuteleers, B. Volckaerts, W. Meeus, M. Brunfaut, J. Van Campenhout, A. Hermanne, H. Thienpont, "Low-cost microoptical modules for MCM level optical

interconnections", IEEE Journal of Selected Topics in Quantum Electronics", Vol.9, no.2, pp.518-530, 2003

[7] A.E.Siegman, S.W.Townsend, "Output beam propagation and beam quality from a multimode stable-cavity laser," IEEE J.of Quantum Electronics, Vol.29, No.4, pp.1212-1217, 1993

Chapter 6 Summary

Benefited from its tremendous gain in bandwidth, optics is taking the leader role instead of electronics in many communication systems for the past three decades, and is expected to continue this trend irresistibly in the predictable future. From the architecture point of view, most optical communication systems provide only the point-to-point topology. The interconnection among the distributed nodes still has to rely on the electronic exchanger, which is becoming an imminent bottleneck throttling the overall system bandwidth. In contrast, all optical exchange networks employing optical switches will skip the heavy-loaded data conversion and achieve a prominent bandwidth enhancement and cost reduction. In the first part of this dissertation, a planar lightwave circuit (PLC) based polymer optical switch utilizing total internal reflection (TIR) effect is proposed and fabricated. The design and fabrication of 2X2 polymer thermo-optic switches based on TIR effect is optimized in the aspect of thermal management and optical transmission. The measured results are comparable to the performance to commercialized polymer optical switches in terms of insertion loss, cross talk and polarization dependent loss, but outperform in device length, power consumption, and switching speed. The wavelength coverage from 630nm to 1600nm, as we called “all-wave coverage”, is the most unique feature of the optical switch. The design and fabrication of a 4X4 optical switch matrix based on the cross-bar structure is also demonstrated, and obtained an ultra compact size, compared with other structures.

The application of the TIR optical switch is extended to provide true time delays (TTD) for phased array antennas (PAA). A fully integrated 4-bit TTD device composed of TIR switches and waveguide delay lines successfully delivered the 16 delay values required by a PAA system. The process integrations are investigated, followed by the testing results of the device. The RF phase noise induced by the optical switch cross talk is theoretically studied, and confirmed by experimental results to be negligible.

As we move from long-distance network to short distance reach, optics encounters increasing difficulties in terms of packaging, reliability and system cost. However, with the rapid increasing speed and complexity of VLSI technology, electrical interconnects

will fail to provide sufficient bandwidth beyond 10GHz after 2012. There does exist an opportunity for the continuing exploration of optics to complement or even replace the conventional board level electrical interconnects. An innovative approach with a fully embedded structure is anticipated to overcome the technical and cost barriers that prohibit the realization of optical interconnects in board levels. In the second half of this dissertation, technology efforts projected to relieve the concerns of low cost, high performance optical layers, as well as the system integration issues are carried out. The fabrication process for large cross section multimode waveguide arrays by silicon hard molding process was investigated. A 51-cm long waveguide array by hot embossing method was successfully demonstrated with -15.1dB insertion, which is the longest molding waveguide that has ever been reported. The 150GHz optical bandwidth measured by a pulse laser will provide sufficient bandwidth overhead for board level optical interconnects application. The coupling efficiency of the 45º micro-mirror was theoretically studied using M^2 factor revised Gaussian beam method. The mirror was also experimentally achieved through a one-step pattern transfer molding process, and obtained a coupling efficiency as high as 85%. The integration of the optoelectronics device with the optical waveguide array is explored. With a simplified integration scheme, the VCSELs and photodiode array are integrated with the thin film waveguide, and successfully demonstrated 12X2.5Gbps signal transmission.

Appendix

Publications of Xiaolong Wang

Journal Publications

[1] **Xiaolong Wang**, Li Wang, Wei Jiang, and R. T. Chen, "51cm-long Hard-molded Waveguide Array with 150 GHz Bandwidth for Board Level Optical Interconnects", *Optics Letters*, accepted

[2] **Xiaolong Wang,** Ray T. Chen, "Image Enhanced Multi-mode Interference Coupler Using Deeply Etched Air Trenches covering C- and L-Bands," *Applied Physics Letters*, submitted

[3] **Xiaolong Wang**, Brie Howely, Maggie Chen, Ray T.Chen, "Phase Error Corrected 4-Bit True Time Delay Module Using Cascaded 2x2 Polymer Waveguide Switch Array," *Applied Optics*, accepted

[4] **Xiaolong Wang**, Brie Howely, Maggie Chen, Ray T.Chen, "4x4 Non-blocking Polymeric Thermo-optic Switch Matrix using the Total Internal Reflection Effect," *IEEE Journal of Selected Topics in Quantum Electronics*, Vol.12, pp.997-1000, Sep/Oct (2006)

[5] **Xiaolong Wang**, Brie Howley, Maggie Chen and Ray Chen, "Polarization-independent All-wave Polymer Based TIR Thermo-optic Switch ," *IEEE Journal of Lightwave Technol.*, Vol.24, pp.1558-1565 (2006)

[6] **Xiaolong Wang**, Brie Howley, Maggie Y. Chen, and Ray T. Chen, "Crosstalk-Minimized Polymeric 2X2 Thermo-optic Switch," *IEEE Photonics Technology Letters*, Vol.18, pp.16-18, (2006)

[7] **Xiaolong Wang**, Qingfeng Yan, Jingwei Liu, Shaowu Chen and Jinzhong Yu, "SOI Waveguides Fabricated by Wet-etching Method," *Jounral of Chinese Semiconductors*, Vol.24, No.10, pp.1025-1029 (2003)

[8] **Xiaolong Wang**, Jingwei Liu, Qingfeng Yan and Jinzhong Yu, "SOI Thermo-optic Modulator and Switch with Fast Response," *Chinese Optics Letters*,Vol.1, No.9, pp.527-528 (2003)

[9] **Xiaolong Wang**, Yu Jinzhong, "The Latest Progress of Optical Waveguide Switches," *China Physics*, Vol.32, No.3, pp.165-170 (2003)

[10] **Xiaolong Wang**, Jinzhong Yu, "Multimode Interference Couplers with different background refractive index," *Acta Photonica Sinica*, Vol.32, No.9, pp.1045-1048 (2002)

[11] **Xiaolong Wang**, Jinzhong Yu, and Shaowu Chen, "Mode Analysis of SOI Waveguide with Trapezoidal Cross Section," *Chinese Optoelectronics/Laser*, Vol.13, No.11, pp.1120-1123 (2002)

[12] Brie Howley, **Xiaolong Wang**, and Ray T. Chen, Yihong Chen, "Experimental evaluation of curved polymer waveguides with air trenches and offsets," *Journal of Applied Physics*, Vol.100, 023114 (2006)

[13] Li Wang, **Xiaolong Wang**, Wei Jiang, Jinho Choi, Hai Bi, and Ray Chen, "45º polymer-based total internal reflection coupling mirrors for fully embedded intraboard guided wave optical interconnects," *Applied Physics Letters*, Vol.87, 141110, (2005)

[14] Brie Howely, Yihong Chen, **Xiaolong Wang**, Qingjun Zhou, Zhong Shi, Yongqiang Jiang, and Ray T. Chen, "2-bit Reconfigurable True Time Delay Lines Using 2X2 Polymer Waveguide Switches," *IEEE Photonics Technology Letters*, Vol.17, No.9, pp.1944-1946 (2005)

[15] Jingwei Liu, **Xiaolong Wang**, Shaowu Chen, and Jinzhong Yu, "Analyses of Relations between Modulating Area Structure and Switch Speed and Power Consumption of SOI Thermo-Optic Switch Based on Finite Element Method," Chinese Journal of Semiconductors, Vol.25 No.10, pp.1324-1330 (2004)

[16] Jinzhong Yu, Qingfeng Yang, Jinsong Xia, **Xiaolong Wang**, **"**SOI (Silicon on Insulator) based integrated optoelectronics," *Journal of Functional Materials and Devices*, Vol.9 No.1, pp.1-7 (2003)

Conference Publications

[17] **Xiaolong Wang**, Brie Howley, Maggie Y.Chen, Panoutsopoulos Basile and Ray T.Chen, "Fully-integrated 4-bit True Time Delay Module using Polymer Optical Switches and Waveguide Delay Lines," *Integrated Photonics Research and Applications (IPRA) Topical Meeting/ Nanophotonics (NANO) Topical Meeting*, Uncasville, CT, April 26-28, 2006

[18] **Xiaolong Wang**, Brie Howley, Maggie Y. Chen, Qingjun Zhou, Ray T.Chen and Panoutsopoulos Basile, "Polymer Based Thermo-optic Switch for Optical True Time Delay," Proceedings of SPIE, Vol.5728, pp.60-67 (2005)

[19] Maggie Yihong Chen, Brie Howley, **Xiaolong Wang**, Panoutsopoulos Basile, and Ray T. Chen, "2-D Scalable Optical Controlled Phased-Array Antenna System," *Nanophotonic Packaging, Proceedings of SPIE*, Vol. 6126, 61260I, (2006)

[20] Brie Howley, **Xiaolong Wang**, Yihong Chen, and Ray T. Chen, "Integrated Polymer Optoelectronic Time Delay Device for an X-band Phased Array Antenna System," *Optoelectronic Integrated Circuits VIII*, *Proc. of SPIE*, Vol. 6124, 61240Z, (2006)

[21] Brie Howley, **Xiaolong Wang**, Qingjun Zhou, Yihong Chen, Ray T. Chen, "Polymer Waveguides and Thermo-Optic Switches for an Optical True Time Delay Phased Array Antenna ," Proceedings of SPIE ,Vol.5731,pp.12-19 (2005)

[22] Li Wang, **Xiaolong Wang**, Jinho Choi, David Hass, Jerry Magera, and Ray T. Chen, " Low-loss, thermally stable waveguide with 45º micromirrors fabricated by soft molding for fully embedded board-level optical interconnects," Proceedings SPIE Vol.5731, pp.87-93 (2005)

[23] Chen, R.T.; Li Wang; Jinho Choi; **Xiaolong Wang**; "Packaging efforts for inter- and intra-board level optical interconnects," *Lasers and Electro-Optics Society*, 2004. LEOS 2004. The 17th Annual Meeting of the IEEE ,Volume: 1 , Nov. 8-9, 2004 Pages:441 – 442

[24] Li Wang, Jinho Choi, **Xiaolong Wang**, Ray T. Chen, David Hass, and Jerry Magera , “Thin film optical waveguide and optoelectronic device integration for fully embedded board level optical interconnects,” *Proc. SPIE Int. Soc. Opt. Eng*. 5556, 1 (2004)

Bibliography

Chapter 1

[1] http://www.labs.nec.co.jp/Eng/Topics/data/r010322/

[2] M. Okuno, "Highly integrated PLC-type optical switches for OADM and OXC systems," in Proc. Optical Fiber Communications Conf., Atlanta, GA, Mar. 2003, vol. 1, pp. 169–170.

[3] Giles, C.R. Aksyuk, V. Barber, B. Ruel, R. Stulz, L. Bishop, D. "A silicon MEMS optical switch attenuator and its use in lightwavesubsystems," IEEE Journal of Selected Topics in Quantum Electronics, Vol.5, No.1, pp.18-25, 1999.

[4] Hattori, K. Fukui, M. Jinno, M. Oguma, M. Oguchi, K. "PLC-based optical add/drop switch with automatic level control," IEEE Journal of Lightwave Technology, Vol.17, No.12, pp.2563-2571, 1999

[5] http://physics.pdx.edu/~larosaa/Agilent_All_Optical_Network.htm

[6] Q. Lai, W. Hunziker, and H. Melchior, "Low-power compact 2 × 2 thermooptic silica-on-silicon waveguide switch with fast response," IEEE Photon. Technol. Lett., vol. 10, no. 5, pp. 681–683, May 1998.

[7] R.V.Schmidt, R.C.Alferness, "Directional Coupler Switches, Modulators and Filters using Alternating ΔβTechniques", IEEE Transactions on Circuit and Systems, Vol.26, No.12, 1979: pp.1099-1108

[8] Y.Silberberg, P.Perimutter and J.E.Baran, "Digital Optical Switch", Applied Physics Letters, Vol.51, No.16, 1987: pp1230-1232

[9] W.K.Burns, and A.F.Milton, "An Analytic Solution for Mode Coupling in Optical Waveguide Branches", IEEE Journal of Quantum Electronics, Vol.16, No.4, 1980: pp446-454

[10] Li, Bing; Tang, Suning; Taboada, John M.; An, Dechang; Shi, Zan; Li, Bulang; Chen, Ray T.,"
Proc. SPIE Vol. 4225, p. 0-9, Optical Interconnects for Telecommunication and Data Communications

[11] A.Yeniay, R.Gao, K.Takayama, and A.F.Garito, IEEE J.Lightwave Technol., Vol.22, No.1, pp.154-158, 2004

[12] Y. Hida, H.Onose, S.Imamura, IEEE Photonics Technology Letters, Vol.5, No.7, pp.782-784, 1993

[13] C.A. Balanis, *Antenna theory: Analysis and design*, 3rd Edition, John Wiley & Sons, 2005

[14] R. C. Hansen, *Phased array antennas*, Wiley-Interscience, 1998

[15] W.Ng, A.Walston, L. Tangonan, J. J. Lee, I. Newberg, and N. Bernstein, "The first demonstration of an optically steered microwave phased array antenna using true-time-delay," *J. Lightwave. Technol.*, vol. 9, no. 9, pp.1124–1131, Sep. 1991.

[16] Z. Shi, Y. Jiang, B. Howley, Y.Chen, F. Zhao, and R.T. Chen, "Continuously Delay-Time Tunable-Waveguide Hologram Module for X-Band Phased-Array Antenna", *IEEE Photon. Technol. Lett.*, vol.15, pp.972-974, July, 2003

[17] K.Horikawa, I.Ogawa, H.Ogawa, and T.Kitoh, "Photonic switched true time delay beam forming network integrated on silica waveguide circuits,," in *IEEE MTT-S Int.*, vol. 1, May 16–20, 1995, pp. 65–68.

[18] J.D.Shin, B.S.Lee, and B.G.Kim, "Optical true time-delay feeder for X-band phased array antennas composed of 2×2 optical MEMS switches and fiber delay lines", *IEEE Photon. Technol. Lett.*, vol.16, pp.1364-1365, May, 2004

[19] B.Howley, Y.Chen, X.Wang, and Ray T.Chen, "2-bit Reconfigurable true time delay lines using 2×2 polymer waveguide switches," *IEEE Photon. Technol. Lett.*, vol.17, pp.1944-1946, Sep. 2005

[20] International SEMATECH, "The National Technology Roadmap for Semiconductors (ITRS)—Technology Needs," Semiconductor Industry Association, 2005.

[21] S. Berry, "Advanced Bus and Interface Market and Trends," *Electronic Trend Publication Inc.*, September 2003.

[22] http://www.intel.com/technology/itj/2004/volume08issue02/art04_interconnect/p02_intro.htm

[23] D. Huang, T. Sze, A. Landin, R. Lytel, and H.L. Davidson, "Optical interconnects: Out of the box forever?" *IEEE J. Sel. Top. Quan. Elec*., vol. 9, no. 2, pp. 614-623, 2003.

[24] R. Mooney. Intel internal document on equalization.

[25] J.W.Goodman, F.I.Leonberger, S.Y.Kung, and R.A.Athale, "Optical Interconnections for VLSI Systems," *Proc. IEEE*, vol. 72, no. 7, pp. 850-866, July 1984

[26] M. Gruber, S. Sinzinger, and J. Jahns, "Optoelectronic multichip module based on planar-integrated free-space optics," Proc. SPIE, Optics in Computing2000, **4089**, (2000)

[27] Mu Hee Cho, Sung Hwan Hwang, Han Seo Cho, and Hyo-Hoon Park, "High-Coupling-Efficiency Optical Interconnection Using a 90 -Bent Fiber Array Connector in Optical Printed Circuit Boards," IEEE Photonics Technology Letters, Vol.17, No.3, pp.690-692, 2005

[28] I.K.Cho, K.B.Yoon, S.H.Ahn, and H.K.Sung, "Experimental demonstration of 10Gbit/s transmission with an optical backplane system using optical slots", Optics Letters, 30,pp.1635-1637, 2005

[29] Elmar Griese, "A High-Performance Hybrid Electrical–Optical Interconnection Technology for High-Speed Electronic Systems," IEEE TRANSACTIONS ON ADVANCED PACKAGING, VOL. 24, NO. 3, pp. 375-383, 2001

[30] Takashi Sakamoto, Hiroyuki Tsuda, Member, Makoto Hikita, Member, Toshiaki Kagawa, Kouta Tateno, and Chikara Amano, "Optical Interconnection Using VCSELs and Polymeric Waveguide Circuits," JOURNAL OF LIGHTWAVE TECHNOLOGY, VOL. 18, NO. 11, pp.1487-1492, 2000

[31] Yuzo Ishii, Shinji Koike, Yoshimitsu aria, and Yasuhiro Ando, "SMT-Compatible Optical I/O Chip Packaging for Chip-Level Optical Interconnects," Elec. Components and Technology Conf. 2001

[32] Eva M. Strzelecka, Duane A. Louderback, Brian J. Thibeault, Geoff B. Thompson, Kent Bertilsson, and Larry A. Coldren, "Parallel free-space optical interconnect based on arrays of vertical-cavity lasers and detectors with monolithic microlenses", Applied Optics, 37, pp.2811-2821, 1998

[33] Choi, C.; Lin, L.; Yujie Liu; Jinho Choi; Li Wang; Haas, D.; Magera, J.; Chen, R.T., "Flexible optical waveguide film fabrications and optoelectronic devices integration for fully embedded board-level optical interconnects," Lightwave Technology, Journal of ,Volume: 22 , Issue: 9 , pp.2168 - 2176, 2004

[34] Choi C, Lin L, Liu YJ, Chen RT, "Performance analysis of 10-mu m-thick VCSEL array in fully embedded board level guided-wave optoelectronic interconnects," ,J LIGHTWAVE TECHNOL 21 (6): pp.1531-1535, 2003

[35] R.T.Chen, L.Lin, C.Choi, Y.Liu, B.Bihari, L.Wu, S.Tang, R.Wickman, B.Picor, M.K.Hibbs-brenner, J.Bristow, and Y.S.Liu, "Fully Embedded Board-Level Guided Wave Optoelectronic Interconnects", Proc. Of the IEEE, 88,6, pp.780-794, 2000

Chapter 2

[1] L.Eldada, "The promise of polymers", SPIE's OEmagazine, pp.26-29, May 2002

[2] C.S Tsai, B.Kim and F.R. Akkari, "Optical channel waveguide switch and coupler using total internal reflection", IEEE Journal of Quantum Electronics, Vol.14, pp. 513-517, 1978

[3] J.Yang, Q.Zhou and R.T.Chen, "Polyimide -waveguide-based optical switch using total-internal –reflection effect", Applied Physics Letters, Vol.81, pp. 2947-2949, 2002

[4] X Wang, B. Howley, M. Chen, et al, "Polymer Based Thermo-optic Switch for Optical True Time Delay", SPIE Photonics West 2005 San Jose

[5] Y.Silberberg, P.Perimutter and J.E.Baran, "Digital Optical Switch", Applied Physics Letters, Vol.51, pp.1230-1232, 1987

[6] Q. Lai, , W. Hunziker, H. Melchior, “Low-power compact 2×2 thermooptic silica-on-silicon waveguide switch with fast response”, IEEE Photonics Technology Letters, Vol.10, pp.681 – 683 ,1998

[7] H.Kogelnik and R.V.Schmidt, “Switched directional couplers with alternating Δβ”, IEEE J. Quantum Electronics, Vol.12, pp.396-401, 1976

[8] P.C Lee, E.Voges, “Three-dimensional semi-vectorial wide-angle beam propagation method”, Journal of Lightwave Technology, Vol.12, pp.215-225, 1994

[9] C. Lee, M. Wu, L. Sheu, P. Fan, J. Hsu, “Design and analysis of completely adiabatic tapered waveguides by conformal mapping”, Journal of Lightwave Technology, Vol.15, pp. 403 – 410, 1997

[10] A.S.Harry, “Thermal Analysis of electro- migration test structures”, IEEE Transactions on Electron Devices, Vol.34, pp.664-672, 1987

[11] I. Cayrefourcq, M. Schaller, C. Fourdin, et al, “Optical switch design for true time delay array antenna”, IEE Proceedings Optoelectronics, , Vol. 145 , pp.77 – 82, 1998

[12] C.C. Constantinou and R.C.Jones, “Path integral analysis of the linearly tapered graded-index waveguide”, J.Phy.D: Appl.Phys., Vol.24, pp.839-848, 1991

[13] S.Matsuoka, Relaxation Phenomena in Polymers. Hanser Gardner, NY: New York, 1992

[14] C.Robertson and G.Wilkes, “Refractive index: a probe for monitoring volume relaxation during physical aging of glassy polymers,” Polymer, vol.39, pp.2129-2133, Nov. 1998

[15] Z.Zhang, G.Xiao and C.Grover,”Volume relaxation in polymers and its effect on waveguide application,” Appl. Opt., vol.43, pp.2325-2331, Apr. 2004

[16] X Wang, B.Howley, M.Chen, et al, “Polymer Based Thermo-optic Switch for Optical True Time Delay,” in SPIE Photon. West’05, San Jose, CA, Jan., 2005, vol. 5728, pp.60-67

[17] L.McCaughan and G.Bogert, “4×4 Ti:LiNbO3 integrated-optical crossbar switch array,” Appl. Phys. Lett., vol.47, pp.348-350, Aug 1985

[18] H.Inoue, H.Nakamura, K.Morosawa, et al, "An 8mm length nonblocking 4×4 optical switch array," IEEE J. Selected Areas in Commun., vol.6, pp.1262-1266, Aug 1988

[19] F.Rabbering, J.Numen and L.Eldada, "Polymeric 16×16 digital optical switch matrix," in Proc. European Conference on Optical Communication 2001, Post-deadline, Amsterdam, Holland, Sep-Oct, 2001

[20] G.Takashi, Y.Missuho, H.Kuninori, et al, "Low-loss and high-extinction-ratio silica-based strictly nonblocking 16×16 thermo-optic matrix switch," IEEE Photon. Technol. Lett., vol.10, pp.810-812, Jun 1998

Chapter 3

[1] W.Ng, A.Walston, L. Tangonan, J. J. Lee, I. Newberg, and N. Bernstein, "The first demonstration of an optically steered microwave phased array antenna using true-time-delay," *J. Lightwave. Technol.*, vol. 9, no. 9, pp.1124–1131, Sep. 1991

[2] Z. Shi, Y. Jiang, B. Howley, Y.Chen, F. Zhao, and R.T. Chen, "Continuously Delay-Time Tunable-Waveguide Hologram Module for X-Band Phased-Array Antenna", IEEE Photon. Technol. Lett., vol.15, pp.972-974, July, 2003

[3] K.Horikawa, I.Ogawa, H.Ogawa, and T.Kitoh, "Photonic switched true time delay beam forming network integrated on silica waveguide circuits,," in IEEE MTT-S Int., vol. 1, May 16–20, 1995, pp. 65–68.

[4] J.D.Shin, B.S.Lee, and B.G.Kim, "Optical true time-delay feeder for X-band phased array antennas composed of 2×2 optical MEMS switches and fiber delay lines", IEEE Photon. Technol. Lett., vol.16, pp.1364-1365, May, 2004

[5] B.Howley, Y.Chen, X.Wang, and Ray T.Chen, "2-bit Reconfigurable true time delay lines using 2×2 polymer waveguide switches," IEEE Photon. Technol. Lett., vol.17, pp.1944-1946, Sep. 2005

[6] Y.O. Noh, J.M. Kim, M.S. Yang, H.J. Choi, H.J. Lee, Y.H. Won, S.G. Han, "Thermo-optic 2 × 2 asymmetric digital optical switches with zero-voltage operation state," IEEE Photon. Technol. Lett., vol.16, pp.446-448, Feb. 2004

[7] X.Wang, B.Howley, M.Y.Chen and R.T. Chen, "Polarization-independent All-wave Polymer Based TIR Thermo-optic Switch", IEEE J. of Lightwave Technol.,vol.24, pp.1558-1565, Mar.2006

[8] A.A. Szep, "Polymer-based integrated optical waveguide true time delay for wide-band phased array antennas," Ph.D. dissertation, pp.17, pp.22-36, Univ. of Southern California, 2002.

[9] G.L Tan, R. E. Mihailovich, J. B. Hacker, J. F. DeNatale, and G.M. Rebeiz, "Low-Loss 2- and 4-bit TTD MEMS Phase Shifters Based on SP4T Switches", IEEE Trans. on Microwave Theory and Techniques, vol.51, pp.297-304, Jan. 2003

[10] X.Wang, B.Howley, M.Y.Chen and R.T.Chen, "Crosstalk minimized polymeric 2 ×2 optical switch", IEEE Photon. Technol. Lett., vol.11, pp.16-18, Jan., 2006

Chapter 4

[1] R. Yoshimura, M. Hikita, S. Tomaru, and S. Imamura, "Low-loss Polymeric Optical Waveguides with 45° mirrors", Jpn. J. Appl. Phys., Vol. 37, pp. 3657-3661, 1998

[2] A. Borreman, S. Musa, A.A.M. Kok, M. B. J. Diemeer and A. Driessen, "Fabrication of Polymeric Multimode Waveguides and Devices in SU-8 Photoresist Using Selective Polymerization" Proceedings Symposium IEEE/LEOS Benelux Chapter, 2002, Amsterdam

[3] L. Eldada, C. Xu, K. Stengel, L. Shacklette, and J. T. Yardley, "Laserfabricated low-loss single-mode raised-rib waveguiding devices in polymers,"J. Lightwave Technol., vol. 14, pp. 1704–1713, 1996.

[4] A. Neyer, T. Knoche, L. Moller, and R. Klein, “Low-loss passive polymer waveguides at 1300 and 1550 nm,” in Proc. Polymer Optical Fibers Conf., 1994, pp. 169–171.

[5] H. Kragl, R. Hohmann, C. Marheine, W. Pott, and G. Pompe, “Low cost monomode, integrated optics polymeric components with passive fiber-chip coupling,” Electron. Lett., vol. 33, pp. 2036–2037, 1997.

[6] G. Pompe, M. Jolinck, S. Kalveram, S. Lehmacher, S. Rudolph, and A. Neyer, “Technology of hot embossed thermo-optic switches in plastics with passive fiber coupling,” in Proc. Plastics in Telecommunications Conf., vol. 8, 1998, pp. 28–29.

[7] A. Brauer and P. Darmberg, “Polymers for passive and switching waveguide components for optical communications,” in Proc. SPIE, vol. CR63, 1997, pp. 334–349.

[8] L.Wang, X.Wang, W.Jiang, J.Choi, H.Bi, and R.T.Chen, “45º polymer-based total internal reflection coupling mirrors for fully embedded intraboard guided wave optical interconnects”, Applied Physics Letters, 87, 141110, 2005

[9] K.B.Yoon, C.G.Choi, S.P.Han, “Fabrication of multimode polymeric waveguides by hot embossing lithography,” Jap.J.of Applied Physics, 43, pp.3450-3451, 2004

[10] H.Mizuno, O.Sugihara, T.Kaino, M.Hosino, “Low-loss polymeric optical waveguides with large cores fabricated by hot embossing”, Optics Letters, 28, pp.2378-2380, 2003

[11] L. Dellmann, R. Dangel, R. Beyeler, C. Berger, F. Horst, B.J. Offrein, and G.-L. Bona, “Polymer waveguides for highspeed optical interconnects,” in EOS Topical Meeting Optics in Computing (European Optical Society, 2004), pp.131–132.

[12] K.K.Lee, D.R.Lim, and L.C.Kimerling, “Fabrication of ultrlow-loss Si/SiO2 waveguides by roughness reduction,” Optics Letters, 26, pp.1888-1890, 2001

[13] F. E. Doany, P. K. Pepeljugoski, A. C. Lehman, J. A. Kash, and R. Dangel, “Measurement of Optical Dispersion in Multimode Polymer Waveguides,” Proceedings of the IEEE–LEOS Summer Topical Meetings, 2004, pp. 31–32.

[14] Z.A.Yasa and N.M.Amer, Optics Commun., "A rapid-scanning autocorrelation scheme for continuous monitoring of picosecond laser pulses", Vol.36, 406 (1981)

[15] D.Nilsson, S.Jensen and A.Menon, "Fabrication of silicon molds for polymer optics," J.of Micromechanics and Microengineering, 13, pp.S57-S61, 2003

Chapter 5

[1] R.T.Chen, L.Lin, C.Choi, Y.Liu, B.Bihari, L.Wu, S.Tang, R.Wickman, B.Picor, M.K.Hibbs-brenner, J.Bristow, and Y.S.Liu, "Fully Embedded Board-Level Guided Wave Optoelectronic Interconnects", Proc. Of the IEEE, 88,6, pp.780-794, 2000

[2] L.Wang, X.Wang, W.Jiang, J.Choi, H.Bi, and R.T.Chen, "45º polymer-based total internal reflection coupling mirrors for fully embedded intraboard guided wave optical interconnects", Applied Physics Letters, 87, 141110, 2005

[3] Choi, C.; Lin, L.; Yujie Liu; Jinho Choi; Li Wang; Haas, D.; Magera, J.; Chen, R.T., "Flexible optical waveguide film fabrications and optoelectronic devices integration for fully embedded board-level optical interconnects ," IEEE J. of Lightwave Technology, 22, pp.2168 – 2176, 2004

[4] J.H. Wu, J. Wu, J. Bao, and X. Wu, "Soft-lithography-based optical interconnection with high misalignment tolerance," Optics Express, Vol.13, No.6, pp.6259-6267, 2005

[5] B. E. A. Saleh, and M. C. Teich, "Fundamentals of photonics," in Chap. 3, John Wiley & Sons (New York), (1991).

[6] C.Debaes, M.Vervaeke, V.Baukens, H.Ottevaere, P. Vynck, P. Tuteleers, B. Volckaerts, W. Meeus, M. Brunfaut, J. Van Campenhout, A. Hermanne, H. Thienpont, "Low-cost microoptical modules for MCM level optical interconnections", IEEE Journal of Selected Topics in Quantum Electronics", Vol.9, no.2, pp.518-530, 2003

[7] A.E.Siegman, S.W.Townsend, “Output beam propagation and beam quality from a multimode stable-cavity laser,” IEEE J.of Quantum Electronics, Vol.29, No.4, pp.1212-1217, 1993

Vita

Xiaolong Wang was born in Lu'an, Anhui, China, on May 3rd, 1977, the son of Xianwei Wang and Weiping Ding. After completing his education at the 1st Middle School in Lu'an, Anhui, China, in 1996, he entered the Department of Material Science and Engineering at Tsinghua University, Beijing, China. He received the degree of Bachelor of Science from Tsinghua University in July 2000. In September 2000, he joined the Institute of Semiconductors, Chinese Academy of Sciences, Beijing, China. He received the degree of Master of Science in Engineering from the Chinese Academy of Sciences in September 2003. He entered the Department of Electrical and Computer Engineering at The University of Texas at Austin in September 2003. His current research topics cover planar lightwave circuit based optical devices, board level optical interconnects and radio frequency photonics for phased array antennas.

Permanent Address: RM206, BLD 71, WEST LANE OF GUANZHUANG, Chaoyang District
Beijing 100024
China

This dissertation was typed by the author.